University of Cape Town

AST5001W

MSc in Astrophysics and Space Science

Detecting Surface Inhomogeneity of Asteroids

Author:
Mandla Mnisi
Project Supervisor:
Dr Nicolas Erasmus

Student Number:
MNSMAN009
UCT Supervisor
Dr Itumeleng Monageng

February 27, 2025

Contents

Abstract

This thesis investigates the detection of surface composition inhomogeneity on asteroids using time-series spectroscopy and photometry. Observations were conducted on three test cases—Pluto, asteroid 2005 EK70, and the weather satellite Meteosat-11 using the Mookodi instrument on the Lesedi telescope. For Pluto, time-resolved spectroscopy revealed methane ice absorption bands, with band depths varying between 3.33% and 4.80%, consistent with previously reported values. Photometric analysis supported these results, showing an $r - i$ colour variation linked to surface inhomogeneity. For asteroid 2005 EK70, no significant spectral variations were detected, suggesting a uniform surface composition. The asteroid's diameter was determined to be 1.25 ± 0.26 km, with a rotation period of 4.34 hours, indicating it is stable. The third test case, Meteosat-11, served as a control to verify Mookodi's ability to track stationary objects. These findings demonstrate the capability of ground-based instruments like Lesedi to detect surface composition inhomogeneity from Earth. Future work could further refine these methods and apply them to a wider range of solar system objects.

1 Introduction

Past spacecraft missions to asteroids have revealed that many asteroids possess relatively homogeneous surfaces, as illustrated in Figure 1. The images in Figure 1 are true-colour photos taken by spacecraft in the visible spectrum and demonstrate that while these objects are not all alike, individual asteroids mostly exhibit a uniform appearance, with homogeneous surface colours ranging from gray-white (similar to lunar regolith) to dark reddish brown and some coal-like black.

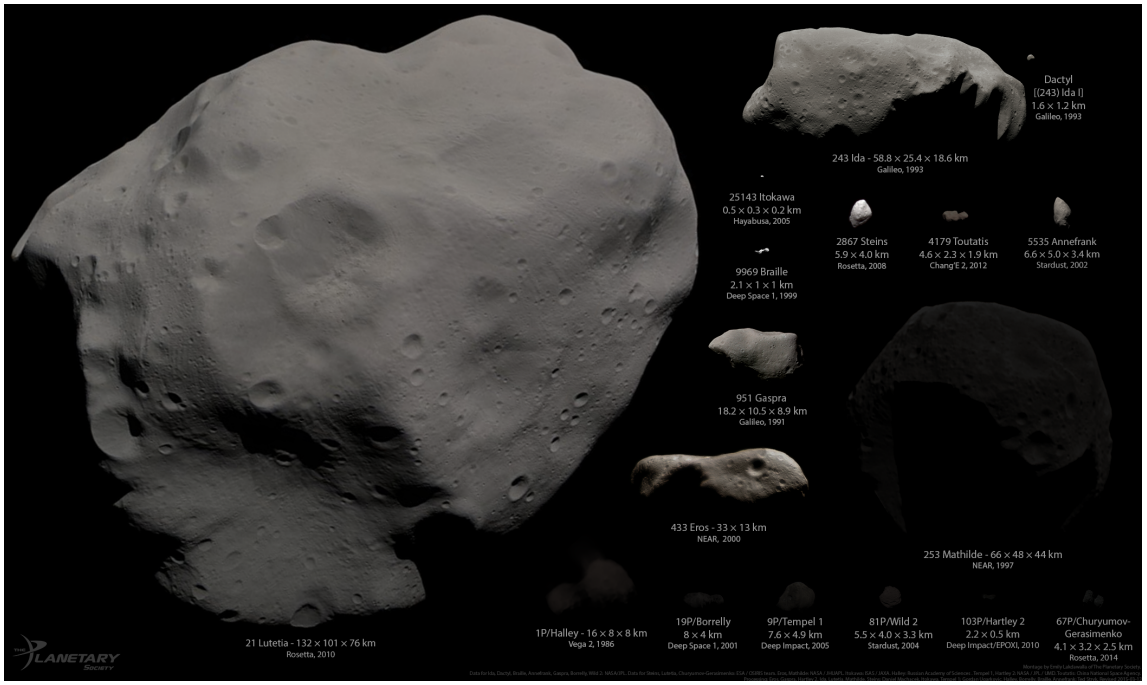

Figure 1: Asteroids that have been visited by spacecraft and the colours of the asteroids are true colours. There is a diversity in albedo levels and spectral signatures and these asteroids show no surface composition inhomogeneity. Source: Emily Lakdawalla/The Planetary Society.

However, a few notable exceptions have challenged this perception. The dwarf planet Ceres and the main-belt asteroid 16 Psyche have both demonstrated evidence of surface composition inhomogeneity. Ground-based observations of Ceres (Carry et al. [2008]), coupled with the DAWN (McCord and Zambon [2019]) spacecraft's close flyby, have uncovered distinct regions with varying albedo and colour, indicative of differing surface materials. The inhomogeneity has since been accredited to cryovolcanism on Ceres (Ruesch et al. [2016]). Similarly, studies based on ground-based infrared observations of 16 Psyche have revealed a patchwork of albedo variations across its surface while radar albedo signatures have indicated the presence of metal-rich material on the surface (Shepard et al. [2021], see Figure 2) which is rare in the asteroid population. The most likely cause of this inhomogeneity has been suggested to be ferrovolcanism (Johnson et al. [2020]). A NASA science mission, launched from Kennedy Space Center on October 13, 2023, is en route to 16 Psyche and is expected to arrive in August 2029, aiming to reveal the true nature of this intriguing asteroid.

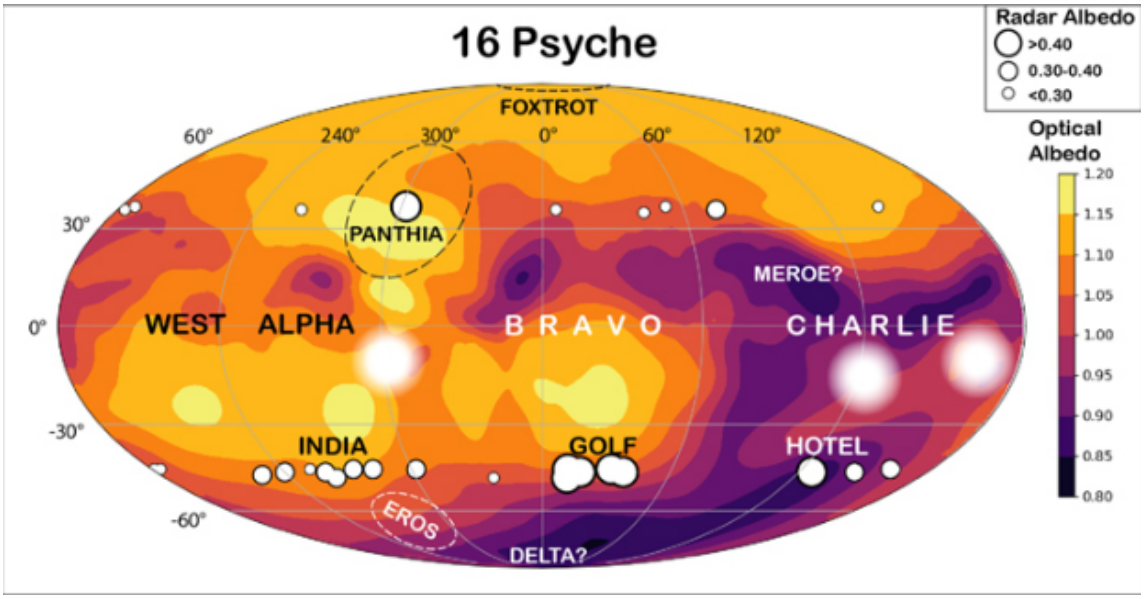

Figure 2: Figure showing the optical albedo map of 16-Psyche. The asteroid appears to be showing albedo inhomogeneity. The different colours on the map are the different levels of optical albedo. The different black circle sizes represent the different ranges in radar albedo. Source: Shepard et al. [2021].

These inhomogeneous asteroids could hold significant scientific and industrial interest. By examining the diverse and often anomalous inhomogeneous asteroids like Psyche, we may gain valuable insights into the formation processes of our Solar System and the underlying mechanisms that shaped our cosmic neighbourhood (Batygin and Brown [2010] and Griveaud et al. [2024]). Moreover, such asteroids may harbor valuable resources that could be exploited for future space mining endeavors (Hein et al. [2018] and Calla et al. [2018]).

While it is impractical to send spacecraft to every asteroid to assess its surface characteristics for inhomogeneity, ground-based telescopes offer a promising alternative. By employing techniques such as time-series spectroscopy and multi-filter photometry, astronomers can potentially identify inhomogeneous asteroids from Earth.

Previous studies, such as those conducted by Lorenzi et al. [2016] on Pluto and Sanchez et al. [2017] on 16 Psyche, have demonstrated the feasibility of using ground-based observations to detect surface composition variations in Solar System objects. These investigations have relied on analysing spectral signatures to identify changes associated with rotational phases, i.e., different locations along longitude.

This thesis aims to evaluate the capabilities of the Mookodi instrument (Erasmus et al. [2024]), a low-resolution spectrograph with multi-filter imaging capabilities, mounted on the 1-m Lesedi telescope (Worters et al. [2016]) operated by the South African Astronomical Observatory (SAAO), in achieving similar results.

To assess the Mookodi instrument's suitability for time-series spectroscopy and the detection of spectral variations related to rotational phases, three specific test observations were conducted. These tests will help determine if the instrument is a suitable candidate to contribute to the discovery and understanding of asteroids with surface inhomogeneity.

The first test involves a target with previously published results showing surface inhomogeneity. The brightness of the target should also be comparable to that of a typical main-belt asteroid, where ground-based low-resolution spectra with a 1-m telescope would result in a decent signal-to-noise ratio, i.e., within an apparent magnitude range of about 5 to 14. To make the first test easier, the target should have slow to medium on-sky motion and a rotation about its axis spanning a few hours or a few days so that multiple long-exposure spectra can be taken at a given rotation phase. Additionally, the target should be observable from the SAAO's site, where Lesedi is located. While technically not an asteroid, Pluto was chosen because it meets all these criteria and will prove that surface inhomogeneity of a Solar System object can be measured with the Mookodi instrument.

The second test involves a Near-Earth Asteroid (NEA) target. While the chances of detecting surface inhomogeneity on a randomly selected NEA are unlikely, this test will prove that time-series spectroscopy on an object with a much faster on-sky motion than Pluto can be performed. This test object should also have a known taxonomic type from literature so we can confirm that our obtained spectra agree with that. For this test, 2005 EK70 was selected because it meets all these criteria and was visible and observable with Lesedi during the time allocated to us on this telescope for this project.

The third test involves a bright asteroid-like object with a high likelihood of displaying surface inhomogeneity. For this test, the weather satellite Meteosat-11 was chosen. Ideally, a defunct tumbling satellite would have been preferred, but this was the only object available that met some of the criteria during the allocated observing run.

This thesis is organised into several sections. Chapter 2 provides an overview of the telescopes and instruments used in this study. Chapter 3 covers the data

reduction pipelines. Chapter 4 presents the first test case target, Pluto. Chapter 5 focuses on the second test case target, 2005 EK70. Chapter 6 discusses the third test case target, Meteosat-11. In the final section, a conclusion is drawn on the thesis as a whole and discussing possible future plans.

2 Telescope, instrument and data pipelines

2.1 Lesedi

The telescope used for this project is the 1-m Lesedi telescope (Worters et al. [2016]) situated at the South African Astronomical Observatory's facility near the town of Sutherland in the Northern Cape, South Africa. The altitude and azimuth (alt-az) mounted telescope features a 1-meter primary mirror with a focal ratio of $f/8$ and two Nasmyth ports, which can be individually fed by a rotatable tertiary mirror, enabling rapid switching between the two ports. Each port has a field of view diameter of 100 mm (approximately 43 arcminutes) and is equipped with a field derotator that houses an autoguider unit. The telescope has excellent pointing and tracking (including non-sidereal tracking) capabilities and is therefore well-suited for this specific project. Each port has a field of view (FoV) diameter of 100 mm.

Of the two Nasmyth ports, one accommodates the Sibonise (formerly WiNCaM) instrument (Worters et al. [2016]), a multi-filter imager (including some specialised narrowband filters) with a semi-wide field of view (about 40×40 arcminutes FoV). The other port houses Mookodi, a low-resolution spectrograph and multi-filter imager. The telescope's optics are optimised for a wavelength range of 350–900 nm.

The Lesedi telescope can be remotely operated by a physical observer but is nominally used in full robotic mode. Figure 3 shows two photographs of the Lesedi telescope: one showing both Nasmyth ports and the other focusing on a single port that houses the Mookodi instrument. The Mookodi instrument is the instrument used for this project.

(a) Front view.

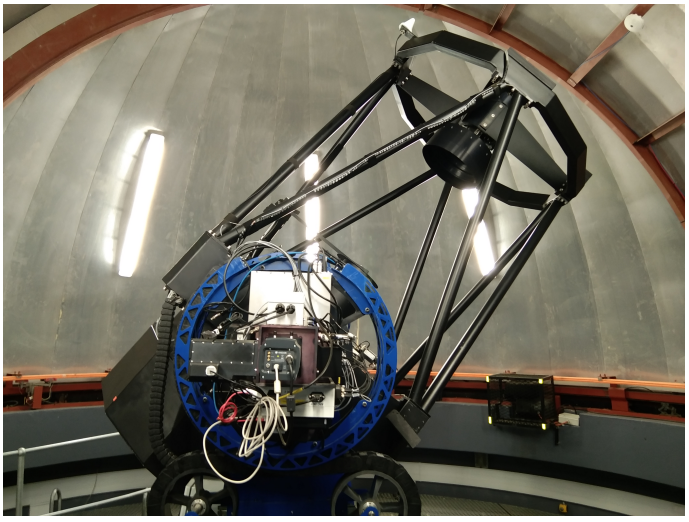

(b) Side view.

Figure 3: The 1-meter alt-az Lesedi telescope from two perspectives: a front view (top) and a side-on view (bottom). In the front view, the large black decagon-shaped structure is the mirror cell, and the circular blue units on either side are the Nasmyth ports. The right Nasmyth port in this image houses the Mookodi instrument, which is the instrument used for this project. Each port is fitted with a field derotator containing an autoguider unit.

2.2 Mookodi

Figure 4 shows a photo of the Mookodi instrument (Erasmus et al. [2024]) with important components labeled.

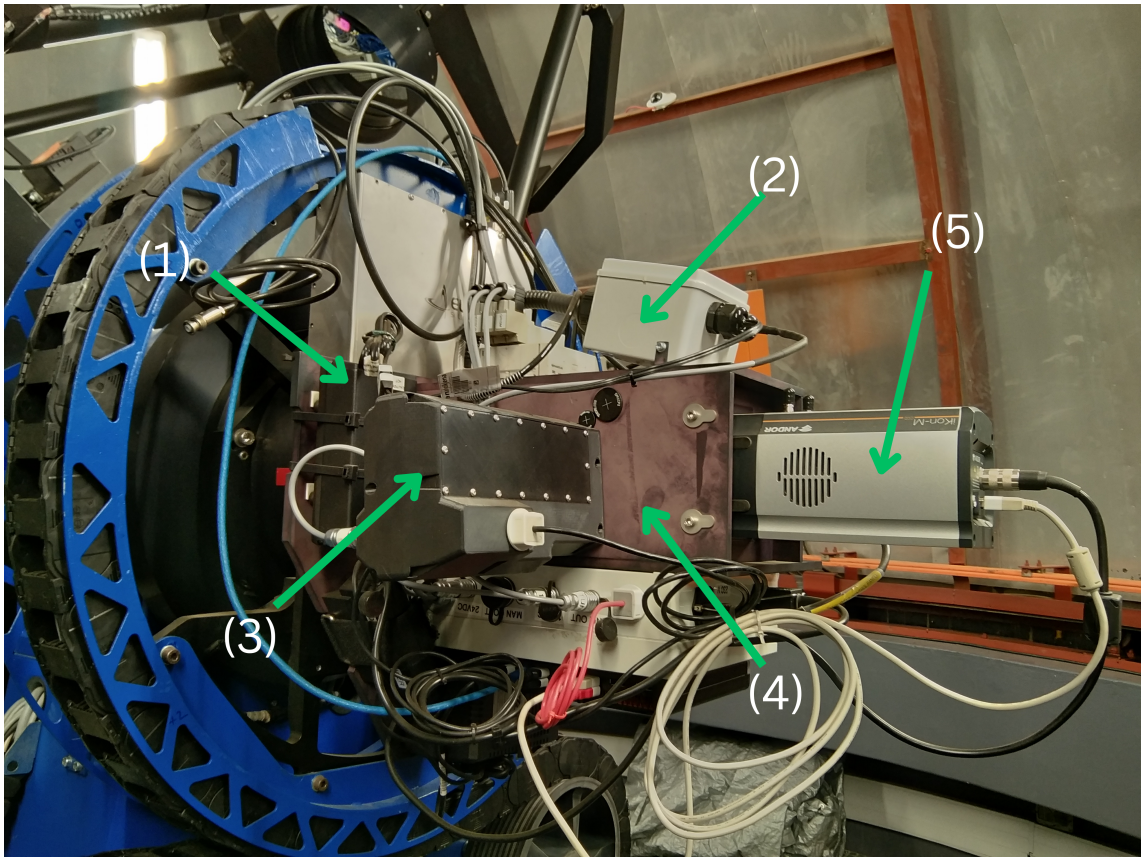

Figure 4: The photo shows the Mookodi instrument. The important components that make up the instrument are labeled with numbers. (1) is the flat/arc lamp mirror, (2) is the housing for the Xenon arc and Tungsten flat lamp, (3) is the filter slide housing, (4) is the optical housing that houses all the optics and optical mechanics of the spectrograph which consists of of the entrance slit of the spectrograph, the collimator lens assembly, the volume phase holographic (VPH) transmission grating and prism pair assembly and the re-imaging lens, and (5) is the Andor detector camera.

The instrument can do both spectroscopy and imaging. When in spectroscopy mode, the instrument utilises a high-efficiency 600 lines/mm volume phase holographic (VPH) grating which results in a wavelength resolution of approximately 350 that spans a wavelength range between 4000 to 8000 Å. The grating is positioned between

two 10-degree BK7 wedge prisms, optimising the input angle to the VPH for system performance and ensuring a straight-through optical path at the output angle, thereby making the switch between spectroscopic and imaging mode as simple as moving the slit and VPH grating out of the beam. This can be done remotely via pneumatics.

The resolution of the spectrograph is determined by the following formula:

$$R = \frac{0.12\rho W}{sD} \tag{1}$$

Here, ρ is the grating lines per mm, W is the beam width in mm, s is the sky projected slit width in arcseconds, and D is the telescope diameter in metres.

The Mookodi detector is a Andor iKon-M 934 (BEX2-DD) features a resolution of 1024×1024 pixels, each measuring 13 microns. The overall size of the detector is 13.3×13.3 mm.

Figure 5 illustrates the optical layout of the Mookodi instrument, incorporating components such as telescope field-corrector lenses, a 50-mm Nikon camera lens, the slit, the focus, the grating, and the collimator.

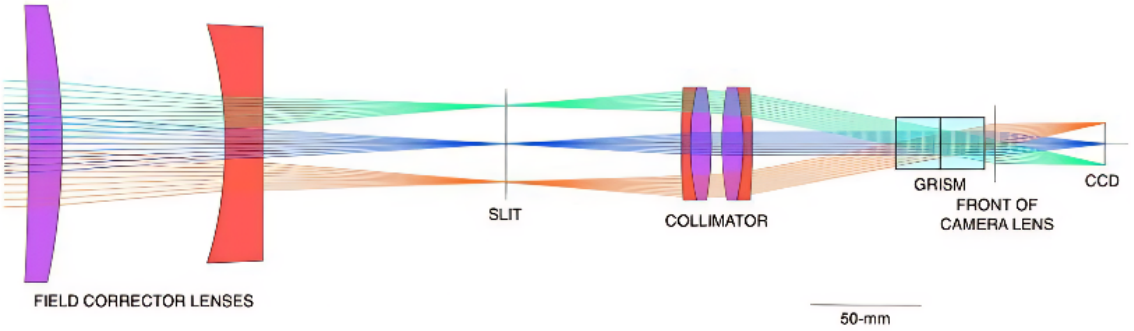

Figure 5: The presentation of the optics of Mookodi. The first two optical components are the telescope field-corrector lenses. The paraxial lens(vertical line) in front of the detector represents the 50-mm Nikon camera lens. The slit is located at the telescope focus and the grating is at the system pupil between the collimator (the achromatic doublet lens pair) and Nikon camera lens. Source: Erasmus et al. [2024].

The wavelength dispersion of the Mookodi detector is 3.85 Å per pixel. The instrument features a stepped-slit with narrow and wide slit region. The projected size of the narrow slit is 2 arcsec×6 arcmin, while the wide slit measures 4 arcsec×1 arcmin. The spectroscopic sensitivity of the detector ensures an $SNR > 5$ at magnitude 16

(1000 sec). The Xenon Pen-Ray (Analytik Jena) serves as the wavelength calibration arc lamp.

The detector has an imaging field-of-view of 10.06 arcmin×10.06 arcmin and an imaging plate scale of 0.59 arcsec/pixel at 1 × 1 binning. The photometric filters incorporated in the Mookodi detector include the full SDSS filters (u', g', r', i', and z'). The limiting magnitude is 20 for the r' filter and 19.5 for the g', i', and z' filters for a 60-second exposure.

3 Reduction pipelines

3.1 ASPIRED for Spectroscopy

To extract spectra from the time-series spectroscopic data taken with Mookodi, a software package called Automated SpectroPhotometric REDuction pipeline (ASPIRED) was used and was developed by Lam et al. [2023]. ASPIRED is a Python-based software package designed to transform 2D-spectral image data into 1D-spectral data, and is capable of handling data from long-slit, low-resolution spectrographs like Mookodi.

The ASPIRED program encompasses two primary routines: image reduction and spectral reduction. The raw FITS spectroscopic data contains both data and metadata that ASPIRED can extract and access. The initial step in the ASPIRED reduction tool involves image reduction—applying correction routines to the science images using bias-, dark-, and flat-frames. Upon completion of image reduction, the subsequent step is the spectral reduction process.

Spectral reduction is a multi-step process. The initial step involves identifying and tracing the spectrum (or spectra [1]) on the reduced spectroscopic image, where the objective is to locate the center of the spectral trace throughout the entire 2D spectrum dispersion. This process is illustrated in Figure 6. The second phase addressed image correction for any deformation present, particularly when the spatial direction of the image is not orthogonal to the dispersion direction. To rectify this, both pixel directions are independently corrected: the spatial direction is aligned using the spectral trace, and the dispersion direction is aligned using sky emission lines.

[1] ASPIRED has the capability of extracting multiple traces from a single 2D image, i.e., multiple sources along a slit

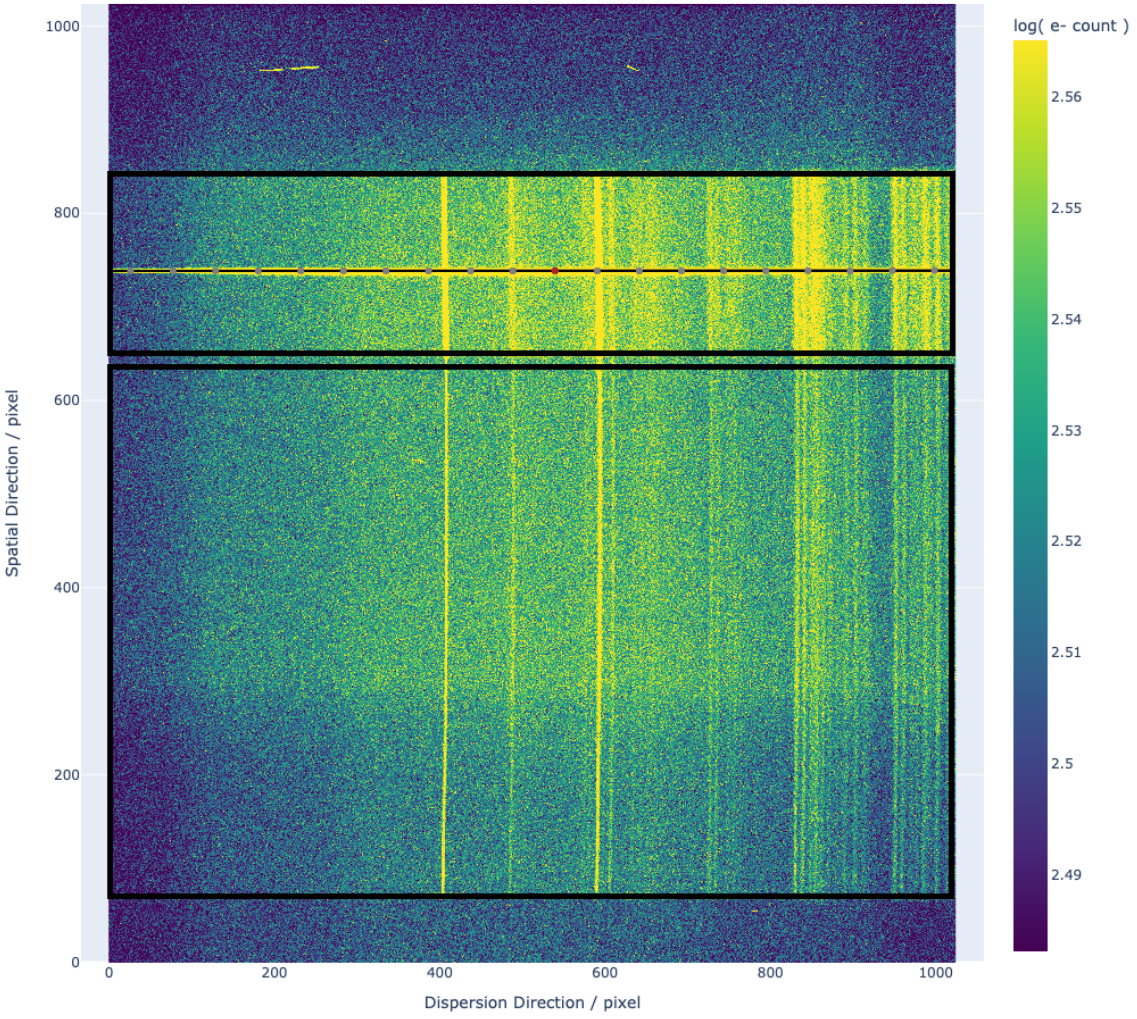

Figure 6: This figure demonstrates ASPIRED's capability to locate the trace spectrum. Two slit areas are visible in this figure: the wide slit and narrow slit area indicated with the two black squares. Skylines shown from the wide slit appear brighter and wider compared to those from the narrow slit, which are dimmer and narrower. The trace of this target is centrally located within the wide slit area. The auto detected trace is indicated with circles where the location of the trace is tracked along the dispersion direction. Additionally, ASPIRED has the capability to remove cosmic rays from the 2D spectral data if they happen to be present on the trace spectrum; however, at this stage, they have not yet been removed.

The third phase revolves around extracting the spectra from the image. The primary goal of spectral extraction is to aggregate electron counts over a defined aperture. Depending on the chosen spectral extraction method, the extraction could be either

robust or optimal in maximising the signal-to-noise ratio (S/N). This optimisation is achieved by applying weights to the spectral profile outskirts, ensuring a lower proportion of photons originating from the sky background rather than the source. Trace spectra counts were measured by summing electron counts over each spectral interval and subtracting background counts, resulting in counts specific to the target. Figure 7 illustrates how counts are extracted from the 2D spectral data.

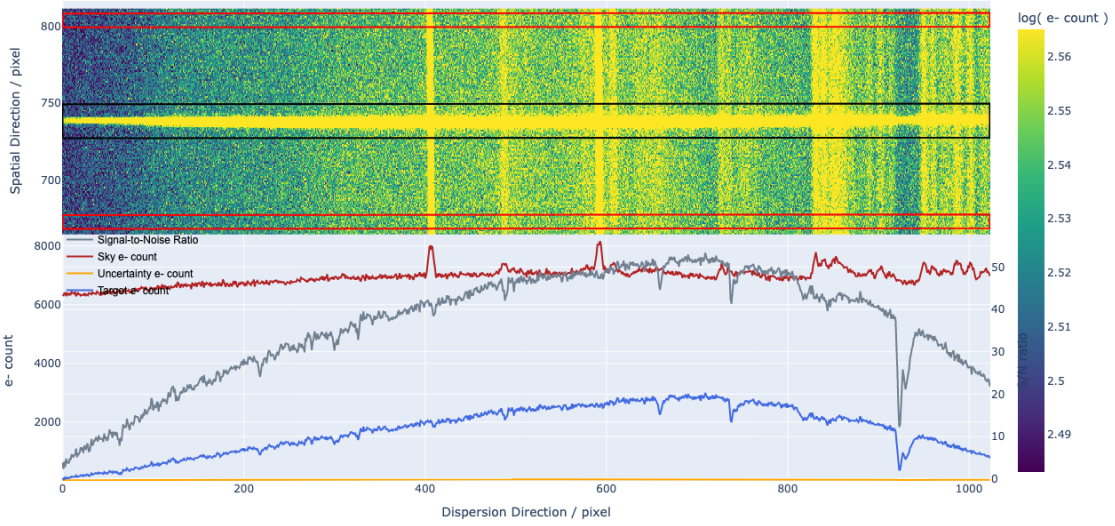

Figure 7: The figure showing how the counts are measured from the 2D spectral trace. The black rectangle covers the counts of the target. The red rectangles cover the background counts. If the widths of the red rectangles are added this gives the total width of the black rectangle. The black rectangle also indicates that the trace is fitted with a first-degree polynomial because the trace spectrum is fairly flat.

A source trace aperture (area encapsulated by black rectangular trace in Figure 7) is used to sum counts along the y-xis within the aperture. A similar method is applied for extracting background counts by considering two background trace apertures (areas encapsulated by the two red rectangular traces in Figure 7) While the traces appear "flat" they are strictly speaking following a fitted first degree polynomial to account for any curvature in the spectra (which is almost negligible in the case of Mookodi).

The fourth phase of spectral reduction involves wavelength calibration for both the science and standard star spectra. This process employs the Hough transform

to establish the pixel-wavelength relation, commonly referred to as Hough pairs. A polynomial function is then derived from the Hough pairs to obtain the most probable wavelength assignments. The key plots used in this calibration step (see Figure 8) includes the arc lamp spectrum, a residual plot (showing differences between fitted peaks and true wavelengths), and a pixel-wavelength plot (overlaying the pixel wavelength function on peak values from the arc spectrum).

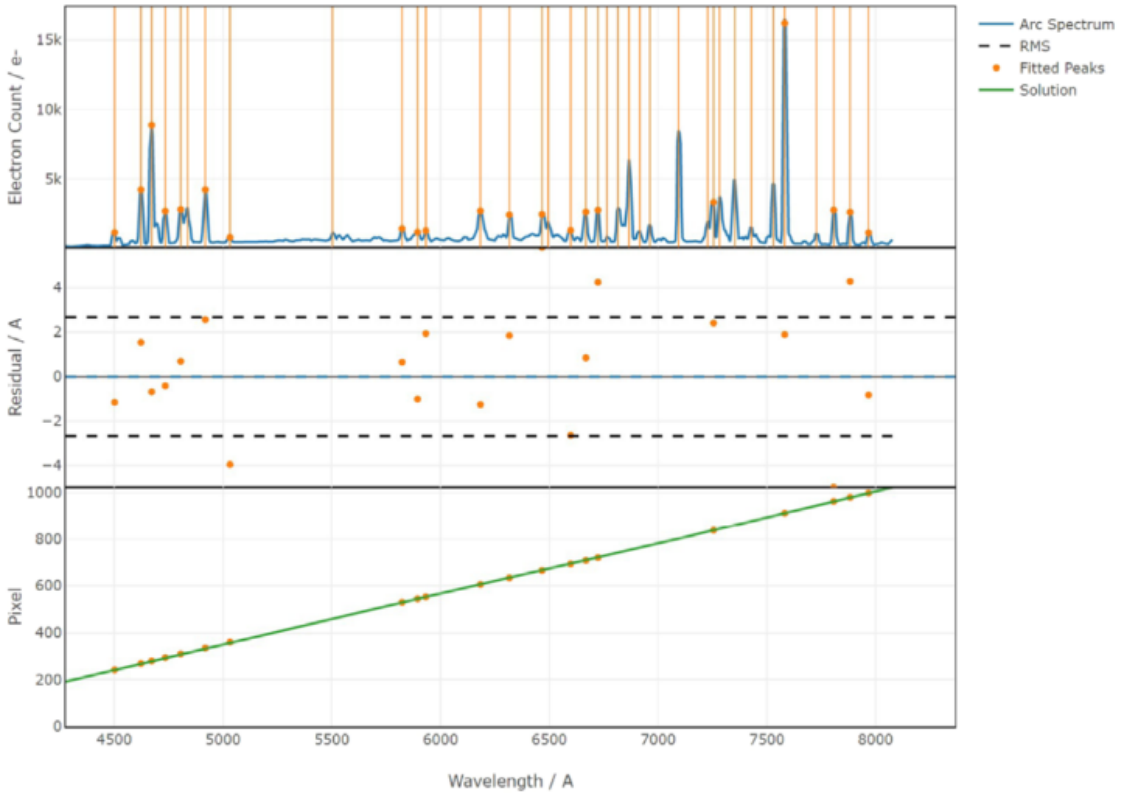

Figure 8: Example figure showing the dignostic wavelength calibration plots of the arc lamp spectrum, a residual plot and a pixel-wavelength plot. Source: Lam et al. [2023].

The fifth step in spectral reduction is flux calibration. In our study, raw counts were utilised instead of calibrated flux, as the target spectra would be normalised using the counts of G-type (i.e. Sun-like) stars since the spectra obtained for this project is sunlight reflected off of the target and not light emitted by the target. The absolute flux is also not essential for the analysis and therefore the flux-calibration step offered by ASPIRED was omitted for this project.

ASPIRED offers an automated and efficient solution for long-slit spectroscopic data

reduction, whereas PypeIt[2] (Prochaska et al. [2020a] and Prochaska et al. [2020b]) provides a more modular and customizable workflow. While both software packages are designed for spectral extraction, they differ in their degree of automation and user control. A key distinction lies in trace detection and spectral extraction: ASPIRED employs polynomial fitting to automatically detect and trace spectra, making it particularly effective for standard long-slit spectroscopy. In contrast, PypeIt allows for greater manual intervention, which can be advantageous when working with complex datasets that require fine-tuned adjustments.

The primary reason for choosing ASPIRED for this project is its out-of-the-box support for Mookodi data. However, future Mookodi users may also want to consider PypeIt, a similar Python-based spectrographic data reduction package. Like ASPIRED, PypeIt is open-source, modular, and written in Python, making it adaptable for various spectroscopic datasets.

Simillar to ASPIRED, PypeIt has been designed for semi-automated reduction of astronomical spectroscopic data and supports a wide range of spectrographs from major observatories, including JWST, Keck, Gemini, VLT, Magellan, and LBT, among others. Its modular approach allows users to configure reduction procedures for different instrument setups, including long-slit, multi-slit, and cross-dispersed echelle spectroscopy. It incorporates trusted algorithms developed by the astronomy community over decades for bias subtraction, flat-fielding, wavelength calibration, sky subtraction, and optimal spectral extraction.

3.2 PHOTOMETRYPIPELINE for Photometry

To complement the time-series spectroscopy data for this thesis work (and since Mookodi can seamlessly, with almost no overhead time, switch to a multi-filter imaging mode) additional images in $g'r'i'z'$ were also collected for TEST CASE 1. The pipeline used for extracting the calibrated photometry from those images was PHOTOMETRYPIPELINE (PP) developed by Mommert [2017]. The pipeline is a Python-based, automated pipeline that can extract automated and calibrated point-source photometry from multi filter imaging data. PP is designed to work with imaging data that comes from small to medium-sized telescopes and is specifically optimised to perform photometry on moving targets (e.g. asteroids), but can also be used for extracting photometry of fixed sources like stars. PP requires images that have already been reduced as a pre-step. Raw images are first reduced by subtracting bias frames and then dividing by a master flat field frame.

[2] `https://pypeit.readthedocs.io/en/stable/`

The PP software consists of five stages in its work flow which are: 1) Image Preparation, 2) Source Extraction and Image Registration, 3) Photometry, 4) Photometric Calibration, and 4) Target Identification and Target Photometry Extraction. Each of these tasks is run with a corresponding stand-alone Python script. Figure 9 shows the work flow diagram of PP.

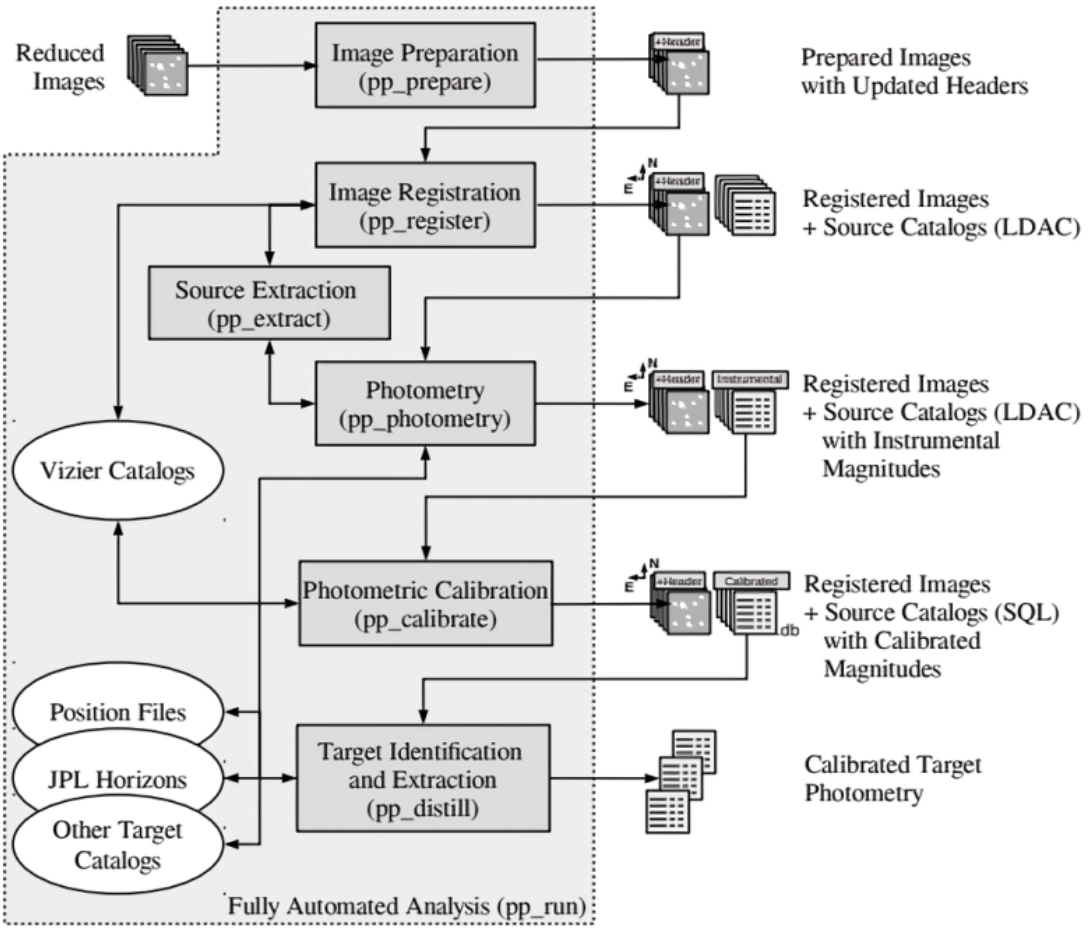

Figure 9: The work flow diagram of the PHOTOMETRYPIPELINE (PP) starting with "Image Preparation" and ending with "Target Identification and Target Photometry Extraction". "Image Preparation" produces the prepared images with slightly modified headers. "Image registration" invokes source identification and extraction routines and produces astrometrically registered images and source catalogs of each source. After that the aperture photometry is performed which produces instrumental magnitudes. "Photometric Calibration" produces the registered images and a SQL source catalogs with calibrated magnitudes. Finally, the "Target Identification" and Extraction produces the calibrated photometry of the target of interest. Each step, as described, can be executed sequentially in a manual way or the entire work flow can be fully automated by using a fully automated script (invoked with the command `"pp_run all"`). Flow diagram source: Mommert [2017]

Telescope and instrument combinations around the world store information in image

files in a unique manner. Therefore, before data analysis can commence, special instructions must be set up in PP's configuration files for each combination. These instructions include files that guide the pipeline in locating and processing critical details within the images. It is essential to ensure that each image header contains vital information, such as the observation date, location, the telescope used, and the object in the observed image. This information is crucial for PP to understand and process the images.

The first task within the PHOTOMETRYPIPELINE, referred to as Image Preparation ("pp_prepare"), examines the information within the image headers and adjusts it to ensure that subsequent tasks in the PP system can interpret the data correctly (e.g format the date). Additionally, it establishes basic instructions for correctly aligning the images, e.g., north up or down.

Each image is analysed using a tool called Source Extractor (Bertin and Arnouts [1996]) [3]. This tool identifies and extracts point sources (such as asteroids, stars etc.) in the image based on their signal-to-noise ratio and other criteria. Source Extractor generates a catalog for each input image, listing all the detected sources.

The second task in the PP is Image Registration ("pp register"), which reads the catalogs generated by Source Extractor. Image Registration utilises a tool called SCAMP (Bertin [2006])[4] to match the detected sources in the input images with known sources in reference catalogs, which are obtained from the VizieR (Ochsenbein et al. [2000]) [5] service. SCAMP calculates an astrometric solution for each image, determining the precise coordinates of the sources. This solution is then imprinted onto the image header, ensuring accurate positional representation. SCAMP may attempt to match the input catalogs with various reference catalogs (e.g. GAIA, Pan-STARRS and LSST) until a suitable match is found. Typically, catalogs such as GAIA, URAT-1, 2MASS, or USNO-B1 are attempted in a specific sequence until successful alignment is achieved. The registration process also assesses the quality of the alignment. Additionally, SCAMP corrects for any distortions in the images. Upon successful registration, the results are provided, including information about each input image indicating the match based on the utilised catalog.

The next task within the PP is Photometry ("pp_photometry"). The Photometry task analyses each source in the images using various aperture sizes to measure the flux and its uncertainty. This analysis is conducted using 20 different aperture radii derived and a curve-of-growth analysis is produced to determine the optimal aperture size.

[3]Source Extractor. Link: `http://www.astromatic.net/software/sextractor`
[4]SCAMP. Link: `http://www.astromatic.net/software/scamp`
[5]VizieR. Link: `https://vizier.cds.unistra.fr/viz-bin/VizieR`

The next task within the PP is Photometric Calibration ("pp calibrate"), which compares the instrument magnitude of background stars in the observed field with their known catalog magnitude. The PP calculates a value known as the magnitude zeropoint, representing the offset between the instrument magnitude in the image and the true magnitude from the catalog.

PP also identifies and removes any stars that may compromise the accuracy of the calibration, such as stars affected by image artifacts or blending with background objects. With the magnitude zeropoint determined, PP applies corrections to the instrument magnitudes of all objects in the image, ensuring that the photometric measurements are calibrated and consistent. The PP system supports converting brightness measurements between different photometric systems (e.g. SDSS, Bessel, etc.).

The next task within the PP is Target Identification and Target Photometry Extraction ("pp_distill"). The "pp_distill" task extracts photometry for selected targets by first extracting photometric data for chosen targets from PP generated databases. Targets are identified based on their coordinates, which can be provided either through simple text files or manually input as fixed coordinates. For moving targets, ephemerides (predicted coordinates at specific time) are obtained from the JPL (Jet Propulsion Laboratory) Horizons database using the CALLHORIZONS[6] Python module.

For each target, a photometry file is created containing information about the target's photometric data, along with diagnostic output, allowing users to assess data quality. The "pp_distill" task automatically selects a reasonably bright star as a "control star". This star is treated the same as any other target and assists in evaluating the reliability of the entire analysis process. The entire PP workflow can be executed using the fully automated analysis script ("pp_run") or each step executed manually.

[6]CALLHORIZONS. Link: `https://github.com/mommermi/callhorizons`

4 TEST CASE 1: Pluto

Pluto and Previous Reports of Surface Inhomogeneity via Earth-based Observations

Pluto serves as an example of a dwarf planet exhibiting extreme surface inhomogeneity. Observations from the New Horizons Mission revealed surfaces characterised by stark variations in albedo and colour (Olkin et al. [2017]). Figure 10 presents an enhanced global colour view of Pluto, illustrating sudden shifts in surface features. The most prominent feature is the bright, heart-shaped region known as Tombaugh Regio, distinguished by its striking white colouration and divided into two distinct lobes. The left lobe, Sputnik Planitia, exhibits high albedo, with a bright and smooth surface, primarily covered in nitrogen ice (Bertrand et al. [2020]).

Surrounding the bright Tombaugh Regio are dark regions, one of which is Cthulhu Macula, located to the left of the bright region. Cthulhu Macula exhibits low albedo and appears reddish-brown in colour. Additionally, several transitional areas display a mixture of reddish-brown and white hues, indicating gradual shifts between regions of high and low albedo.

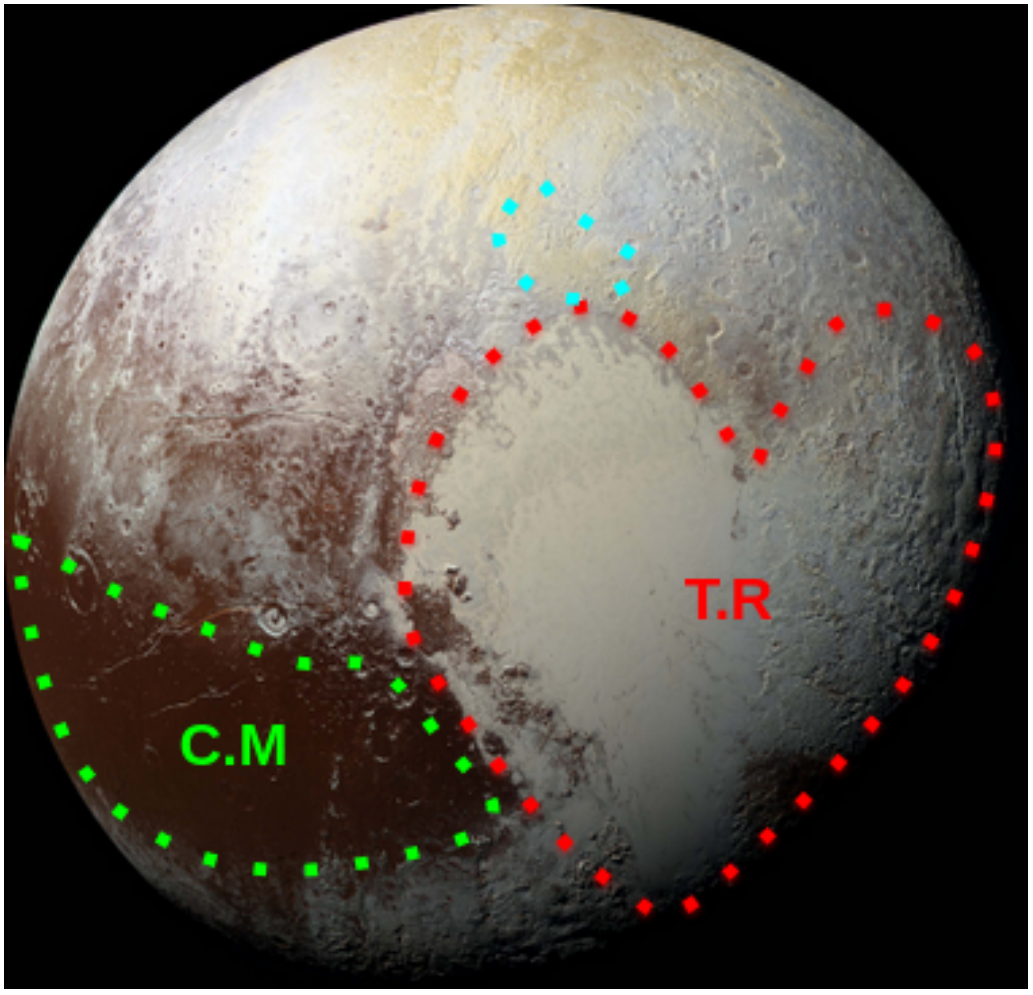

Figure 10: Figure showing an enhanced colour global view of Pluto taken by NASA's New Horizons spacecraft (Olkin et al. [2017]). Some of the marked areas are Cthulhu Macula (labelled as C.M, patch of area highlighted with a green dotted outline), Tombaugh Regio (labelled as T.R, patch of area highlighted with a red dotted outline) and a patch of area with a mix of white and reddish-brown (highlighted with a blue dotted outline) . There are significant variations in the colour and albedo. Some areas are bright white and some areas are reddish-brown. There also exists transition areas where there is a mix between reddish brown and bright white. Source: NASA/JHUAPL/SwRI

Figure 11 presents two plots, of which the upper plot illustrates the photometric light curve data of Pluto, serendipitously collected by the Asteroid Terrestrial-impact Last Alert System (ATLAS) network between 2017 and 2022 (see Tonry et al. [2018] for details on the ATLAS system). The data was retrieved using ATLAS's publically

available "Forced Photometry Service"[7] and consists of photometric data acquired in two custom broadband filters: the *c*-filter, covering 420-650 nm, and the *o*-filter, covering 560-820 nm. The lower plot shows this data phased according to Pluto's known rotational period of 6.387 days, as established by Tholen and Tedesco [1994]. The phased light curve demonstrates a clear brightness fluctuation of approximately 0.1 magnitude, correlated to the rotational phase. This brightness variation can only be due to changes in Pluto's surface albedo since Pluto is spherical in shape, in contrast to many smaller asteroids, which display brightness variations due to their irregular shapes rather than surface composition differences.

Although the phased light curves for the two filters show no significant colour variation with rotation, this is most likley due to the broad bandwidths of approximately 250 nm for each filter, which could obscure subtle spectral changes. However, time-series spectroscopy, even at low resolution, could reveal spectral variations linked to Pluto's rotation, potentially indicating surface inhomogeneity.

[7]Link to the Forced Photometry Service:`https://fallingstar-data.com/forcedphot/`

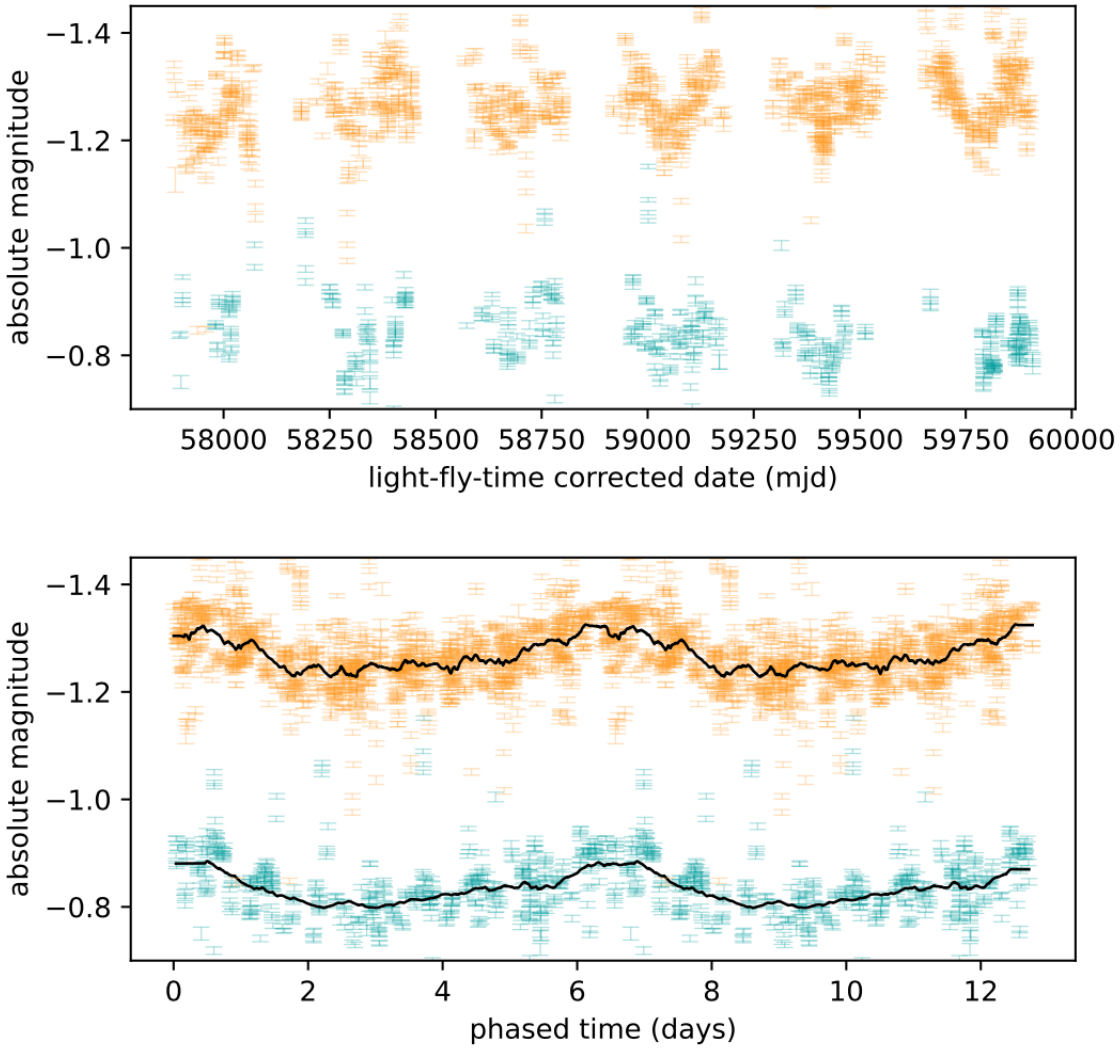

Figure 11: (Top panel): Photometric light curve data of Pluto collected by the ATLAS network between 2017 and 2022 using two custom broadband filters: *c* (420-650 nm) and *o* (560-820 nm). (Bottom panel): Shows the data folded with Pluto's rotation period of 6.387 days, revealing brightness variations of approximately 0.1 magnitude as a function of rotation period. The black lines on the plot represent the running-averages to guide the eye. The data was retrieved using ATLAS's publically available "Forced Photometry Service"(Shingles et al. [2021]). The figure is credited to N. Erasmus and reproduced with permission (private communication).

In a study by Lorenzi et al. [2016], Pluto was observed on six different nights between May 13 and July 17, 2014, utilising the low-resolution spectroscopic mode of Auxiliary-port Camera (ACAM, Benn et al. [2008]), mounted on the 4.2-metre

William Herschel Telescope(Boksenberg [1985]) at the Observatorio del Roque de los Muchachos. The observations were carried out using the V400 disperser with a 1.5 arcsecond slit, providing a spectral resolution of 300 at 0.55 micrometers, similar to that of Mookodi (See Chapter 2.2).

The reflectance spectra obtained by Lorenzi et al. [2016], as depicted in Figure 12, represent the spectra of Pluto, normalised against a solar-type star spectra to eliminate standard star colour and telluric absorption lines.

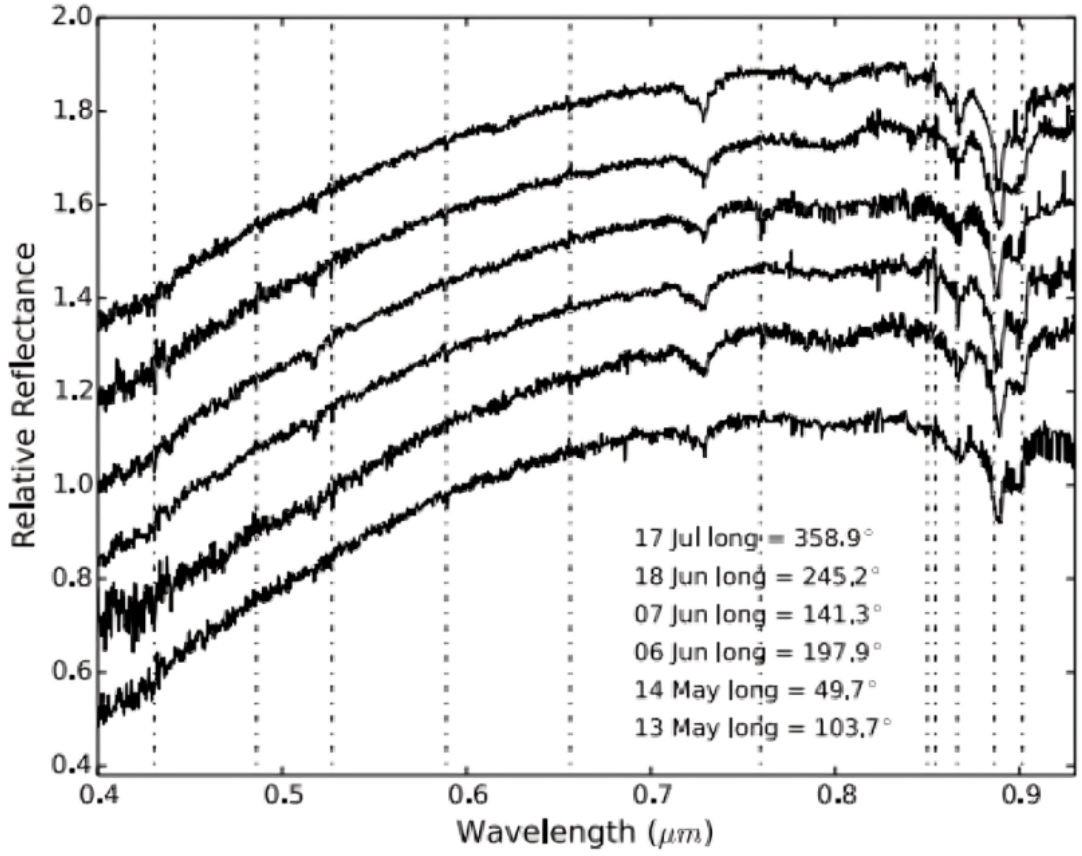

Figure 12: Figure showing six reflectance spectra observed by Lorenzi et al. [2016] at various rotation phases of Pluto. The legend shows the date and longitude of Pluto as viewed from Earth (i.e., rotation phase) of each observation in the same order as they appear in the plot; for example, the top most spectrum was taken on July 17, at a longitude of 358.9°. All reflectance spectra are normalised at 0.6 μm and shifted vertically by 0.15 relative to each other for clarity. The vertical dashed lines indicate the location of telluric absorption lines, so any residual feature located there is likely not a real signal from Pluto's surface. The reflectance spectra clearly show methane ice absorption bands at 0.73, 0.78-0.80, and 0.83-0.91 μm. The depth of these methane ice absorption band features can be seen to vary as a function of longitude (i.e., rotation phase). Source: Lorenzi et al. [2016].

The normalised spectra revealed methane ice absorption bands at 0.73, 0.78-0.80, and 0.83-0.91 μm. Lorenzi et al. [2016] calculated the isolated band depths at various wavelengths, with one-sigma errors provided for each measurement. The study further examined the variation in band depth (in %) with longitude for the five prominent

methane absorption bands, as illustrated in Figure 13 . The observed variations in methane ice absorption bands are indicative of methane concentration changes on the surface of Pluto, suggesting surface composition inhomogeneity. Specifically, the absorption bands at 0.89 μm, 0.87 μm, and 0.73 μm exhibited a band depth variability of 3 %, while the bands at 0.80 μm and 0.79 μm showed a variability of 2 %.

Lorenzi et al. [2016] compared their findings to that of an independent study of Grundy et al. [2013] (see bottom panel of Figure 13), who reported variations in band depths at different wavelengths (1.14, 1.72, and 2.32 μm). The band depth variability in these absorption bands was more, at around 10 %, but the trend matched that of the results from Lorenzi et al. [2016].

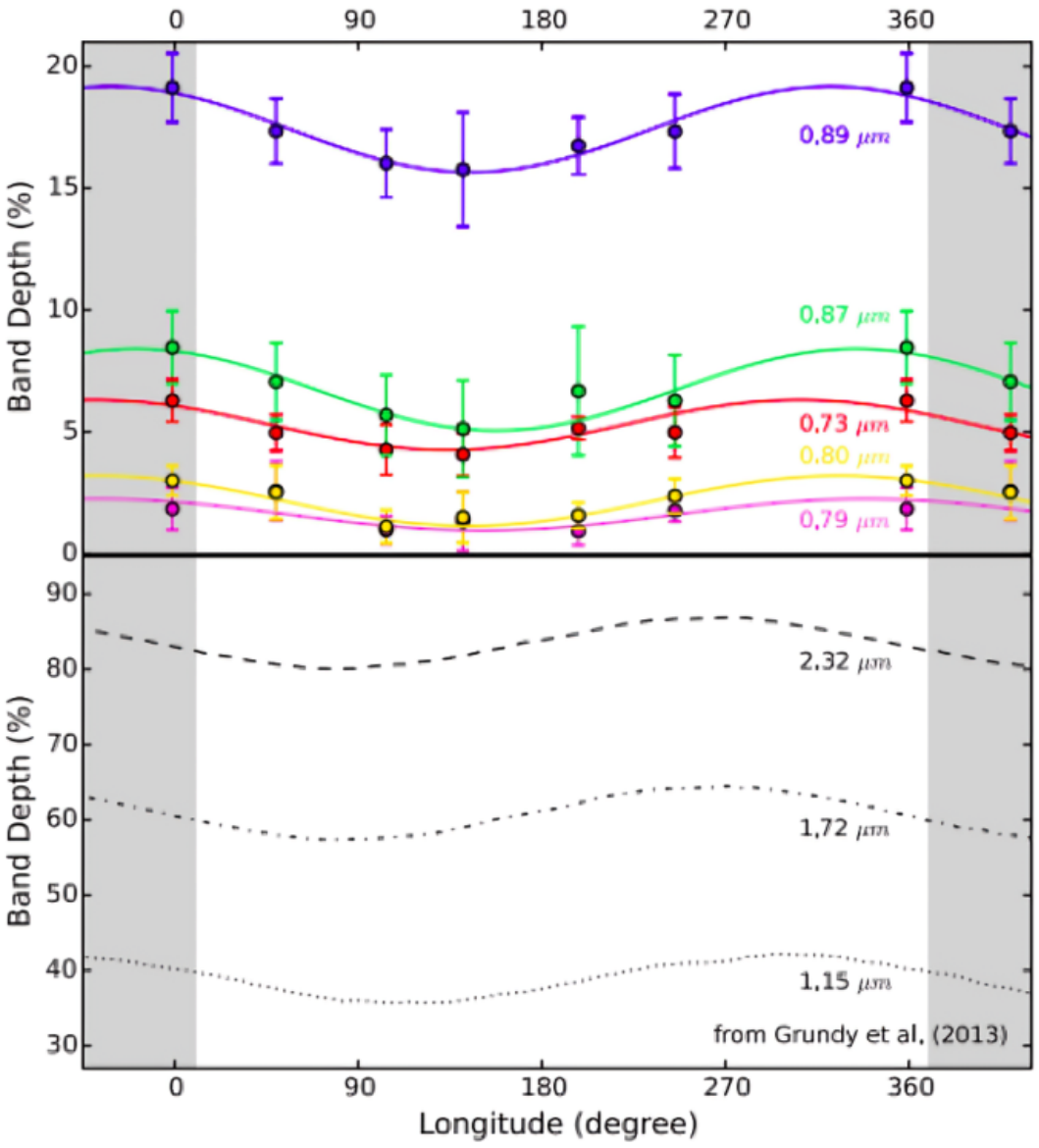

Figure 13: (Top panel): Shows the variation in band depth (in %) with longitude for the five stronger methane absorption bands. The strong methane bands identified by Lorenzi et al. [2016] are at 0.89 μm, 0.87 μm, 0.73 μm, 0.80 μm, and 0.79 μm. The band depth data points were fitted with a sinusoidal function to clarify the trend. (Bottom panel): Illustrates the variation in band depth (in %) with longitude for three strong methane bands, which are at 2.32 μm, 1.72 μm, and 1.15 μm. Source: Lorenzi et al. [2016].

4.1 Observing Pluto with Mookodi

4.1.1 Observing Strategy

The observing strategy for Pluto was primarily designed to replicate the results of Lorenzi et al. [2016], which required covering an entire rotation period (i.e., at least 6 days). Using ephemeris obtained from JPL Horizons [8], a week in early July 2024 was identified for observations. A bright standard (G-type) star named HD 190617 with coordinates similar to Pluto was also identified, and observations of this star were scheduled after each Pluto observation to ensure they were captured at roughly the same time and therefore under similar airmass conditions.

For the observations, The Lesedi telescope was used in robotic mode i.e. the observing requests for Pluto and the standard star were submitted via Lesedi's newly developed Observatory Control System (OCS) that schedules the observations. The OCS is based on the recently open-sourced software [9] developed by the Las Cumbres Observatory (Brown et al. [2013]). The observations were monitored closely, and interventions were made when necessary by resubmitting failed observations or adjusting the submission order to ensure proper data collection.

The observations were conducted in robotic mode. Unfortunately, at the time of the observations, the ability to perform non-sidereal tracking and to adjust the parallactic angle was not yet possible in robotic mode. However, Pluto could essentially be treated as a sidereal object due to its relatively slow motion. The JPL Horizon system provided precise positional data for Pluto, indicating that on 10 July 2023 at 22:00 UTC, its Right Ascension was 20 h:07 m:11.27 s and its Declination was $-22°{:}57'10.0"$. The RA and Dec rates were found to be -3.41 arcsec/hour and -1.01 arcsec/hour, respectively. Given these small motion rates, Pluto's movement across the sky was minimal during the planned observation period.

With the RA and Dec motion rates established, calculations indicated that Pluto would move a total of 3.56 arcseconds/hour. The spectrograph's slit had a width of 4 arcseconds, meaning that Pluto would take approximately 1 hour and 7 minutes to traverse the slit completely. To accommodate this, the observation strategy was designed around a 30-minute window, during which two 10-minute spectroscopic exposures were carried out. At the midpoint of this window, Pluto's RA and Dec values were used to position it centrally within the slit. Over the course of the 30-minute period, Pluto's displacement was approximately 1.78 arcseconds, ensuring that it remained within the slit throughout both exposures.

[8] Horizons system. Link: `https://ssd.jpl.nasa.gov/horizons/`

[9] `https://observatorycontrolsystem.github.io/`

Following the spectroscopic observations, photometric measurements were taken. Precise non-sidereal tracking was also not required for the photometry, as Pluto's exact position within the image was not critical, provided it remained within the instrument's field of view. The lack of non-sidereal tracking therefore did not impact the quality of the photometric and spectroscopic data. As a result, both spectroscopic and photometric data were successfully obtained, even with the constraints imposed by the robotic mode. Observations of Pluto were carried out continuously for one week from June 23rd to June 30th, 2023. A few days later, the observations resumed to fill in some of the rotational phase gaps that were missed during the early July observing run, concluding on July 24th, 2023 (see the table summary of observations in Appendix A). For all the observation dates, two Pluto spectroscopic science exposures were taken roughly every hour, each with an exposure time of 600 sec. For each spectroscopic science image collected on all observation dates, there is a corresponding arc. To calibrate the spectral data, standard star frames were collected at regular intervals during the observation. In addition, photometric science exposures were collected using the g'r'i'z' Sloan filters available with Mookodi in imaging mode. An exposure times of 60 sec was chosen to avoid saturation for the photometric exposures.

The viewing geometry of the Lorenzi et al. [2016] was compared to the viewing geometry at the time of the observations for this project. The results show that the viewing geometry has changed over time since the direction of rotation axis has evolved over time due to the shift in the Pluto-Earth-Sun orientation (see Figure 14).

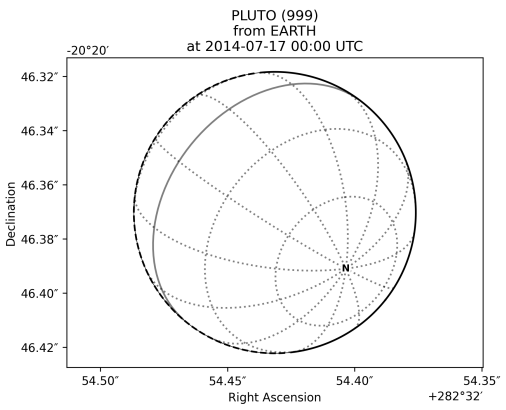

(a) Lorenzi et al. [2016] Pluto wireframe on 17 July 2014. The sub-Earth latitude for this geometry is 51° North on Pluto.

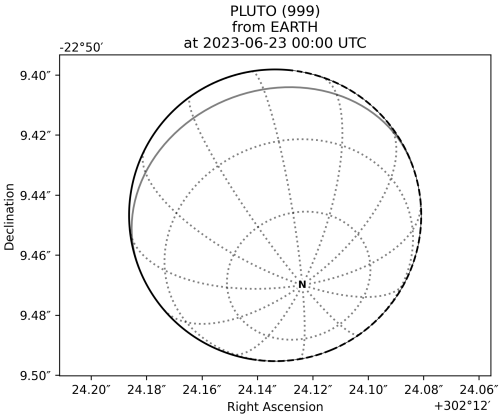

(b) 23 June 2023 Pluto wireframe. The sub-Earth latitude for this geometry is 58.86° North on Pluto.

Figure 14: Wireframe orientations for the Lorenzi et al. [2016] observations (left figure) and the 23 June 2023 observations (right Figure). The viewing geometry has changed when comparing the Lorenzi et al. [2016] observations.

4.1.2 Data Collected

Table 1 provides a summary of the spectroscopic observations of Pluto and the standard star HD 190617, conducted between June 23rd and July 24th, 2023. The table lists the number of exposures taken for both Pluto and HD 190617 on each observation night, along with the corresponding exposure times. On July 11th, the exposure time for HD 190617 was reduced from 60 seconds to 30 seconds to avoid CCD saturation.

Table 1: Summary of Pluto and HD 190617 Spectroscopic Science Exposures

Date	Number of Pluto Exposures	Exposure Time (sec)	Number of HD 190617 Exposures	Exposure Time (sec)
June 23rd	10	600	3	60
July 10th	13	600	12	60
July 11th	16	600	29	30
July 12th	16	600	36	30
July 13th	14	600	44	30
July 14th	5	600	35	30
July 16th	12	600	28	30
July 17th	14	600	22	30
July 20th	4	600	1	30
July 21st	8	600	56	30
July 22nd	12	600	64	30
July 24th	14	600	30	30

The orbital configuration of the Pluto-Earth-Sun system, during the observation dates, meant the Lesedi telescope observed the average sub-Earth latitude of 58.86° North

on the surface of Pluto. The sub-Earth latitude observed by Lorenzi et al. [2016] was 51° North. Figure 15 displays the New Horizons reflectance map covering a $0^\circ - 360^\circ$ longitude range and a $0^\circ - 90^\circ$ latitude range on the surface of Pluto. The coloured crosses indicate the longitude coverage of the observations, and a red horizontal dashed line represents the longitudinal coverage of observations made by Lorenzi et al. [2016].

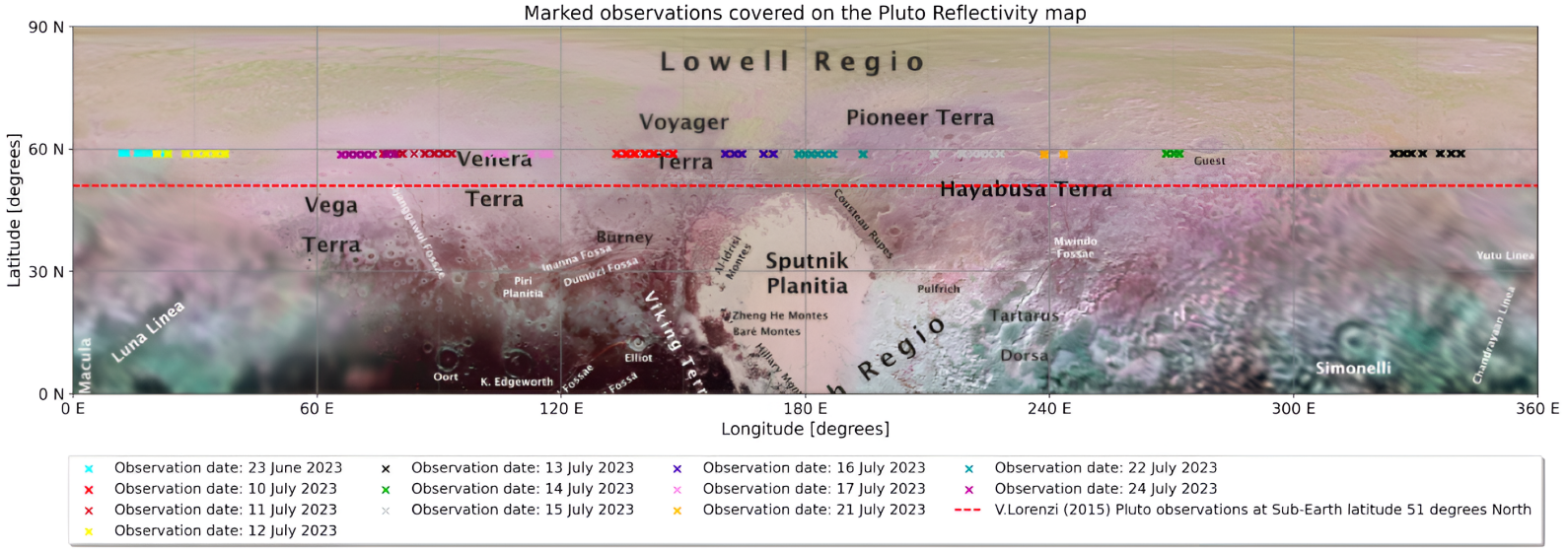

Figure 15: Figure showing the New Horizons Colourmap with marked observations. The Pluto Colourmap has the coordinate grid of Latitude (in degrees) versus Longitude (in degrees). The colour crosses represent the locations where the Lesedi Telescope collected the spectroscopic data and the legend (which is below the reflectance map) is included to indicate the observation date of the marked locations. Source of colourmap: `https://photojournal.jpl.nasa.gov/catalog/PIA11707`

Table 2 summarises the longitude coverages for each of the Lesedi telescope observation dates on the surface of Pluto.

Date	Minimum longitude [deg]	Maximum longitude [deg]
23 June 2023	11.89	23.21
10 July 2023	133.41	147.57
11 July 2023	76.07	93.24
12 July 2023	20.32	37.50
13 July 2023	324.45	341.27
14 July 2023	268.50	272.10
15 July 2023	211.44	228.05
16 July 2023	160.09	172.28
17 July 2023	101.50	117.24
21 July 2023	238.52	243.63
22 July 2023	178.09	194.34
24 July 2023	65.80	79.07

Table 2: Longitude coverages of the Pluto spectroscopic data for each observation date. The table shows the minimum and maximum longitude covered on each observation date. As evident from the table there was approximately 20° of latitude change during the course of an observing night.

4.1.3 Spectra taken at different airmass and parallactic angles

Spectra within the same range of airmass but with different parallactic angles were juxtaposed on a single plot to assess alignment around telluric lines and ensure uniform shape. The results indicate a lack of alignment in both the HD 190617 spectra and their peak wavelengths indicating that the parallactic angle at which observations are taken can have drastic effects on the observed spectral shape. Figure 16 showcases spectra of HD 190617 within the range $1 < airmass < 1.1$ but with varying parallactic angles. It is evident from the plot that telluric lines are misaligned, and the spectral shapes, particularly the peaks, do not match. Additionally, it is noteworthy that the altitude-azimuth coordinates of each HD 190617 spectrum is different. The altitude values of the HD 190617 spectra are close while the azimuth values are significantly different on Figure 16. Note that on Figure 16, the dates of each spectrum are different: the green spectrum was taken on the 15th of July 2023, the orange spectrum was taken on the 17th of July, and the blue spectrum was taken on the 21st of July, but importantly, the main difference is the parallactic angle versus the slit orientation relative to that.

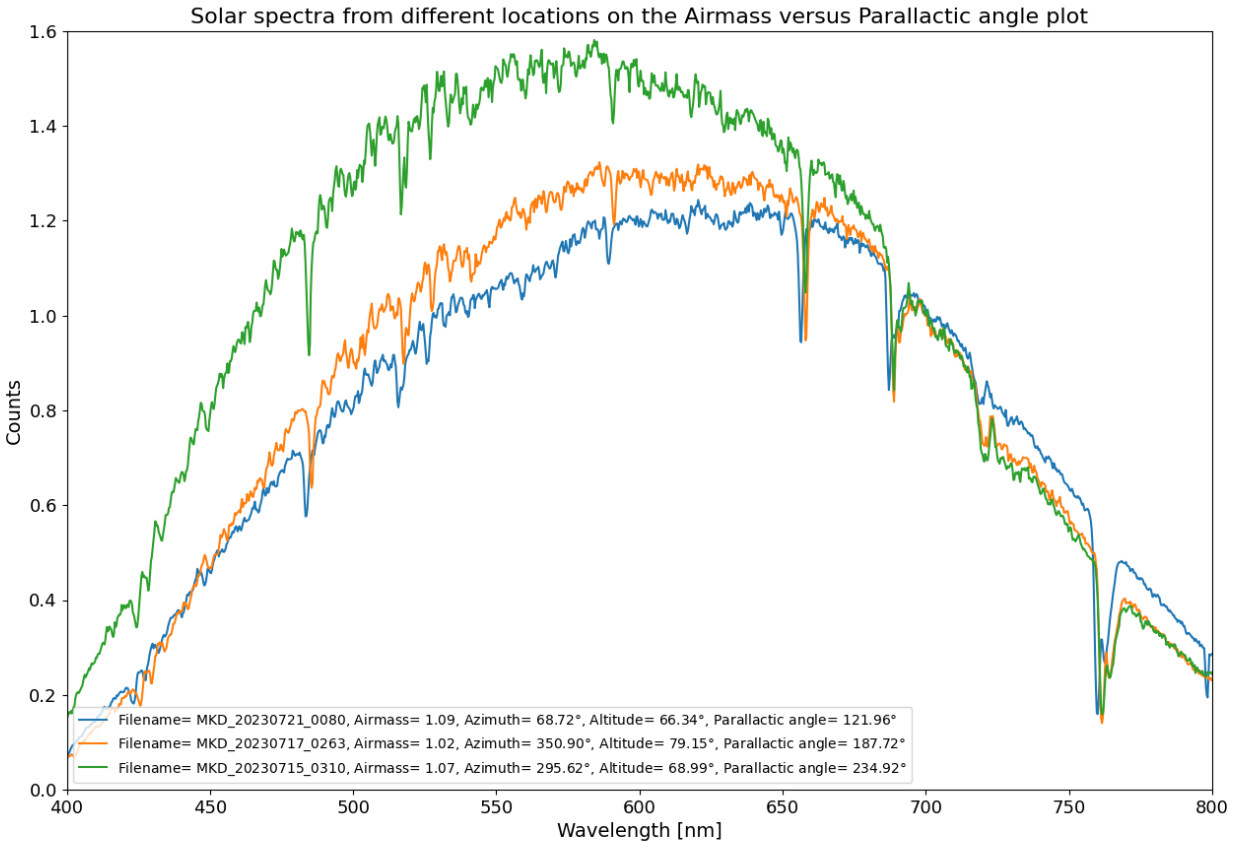

Figure 16: Spectral plot showing three spectra of HD 190617 that are within the airmass range of $1 < X < 1.1$ but different parallactic angles. The blue HD 190617 spectrum has a parallactic angle of 121.96^o, the orange HD 190617 spectrum has a parallactic angle of 187.72^o and the green solar spectrum has a parallactic angle of 234.92^o. The dates for each of the HD 190617 spectra are 21 July 2023 (blue spectrum), 17 July 2023 (orange spectrum) and 15 July 2023 (green spectrum).

4.1.4 Parallactic angle and airmass considerations

The study of ground-based astronomical observations requires a consideration of several atmospheric effects that may influence the accuracy of the collected data. Among these, the parallactic angle and airmass are particularly important as they impact how light from astronomical bodies is altered while passing through the Earth's atmosphere. Given the nature of this project, which aims to analyse the

surface composition variations of Pluto, it is essential to account for such factors to avoid inaccuracies (as motivated in section 4.1.3) in the observed spectral data. Misinterpretation of these atmospheric distortions could lead to incorrect conclusions regarding the features of Pluto's surface. Therefore, a thorough discussion of these effects is necessary to ensure the reliability of the results obtained from the data.

The spectroscopic data were gathered for the selected targets, recording observation parameters such as object name, observation time, airmass, target surface coordinates (longitude and latitude), altitude and azimuth of the telescope, and parallactic angle of the observations. The initial step involved plotting the altitude versus azimuth graph, as illustrated in Figure 17.

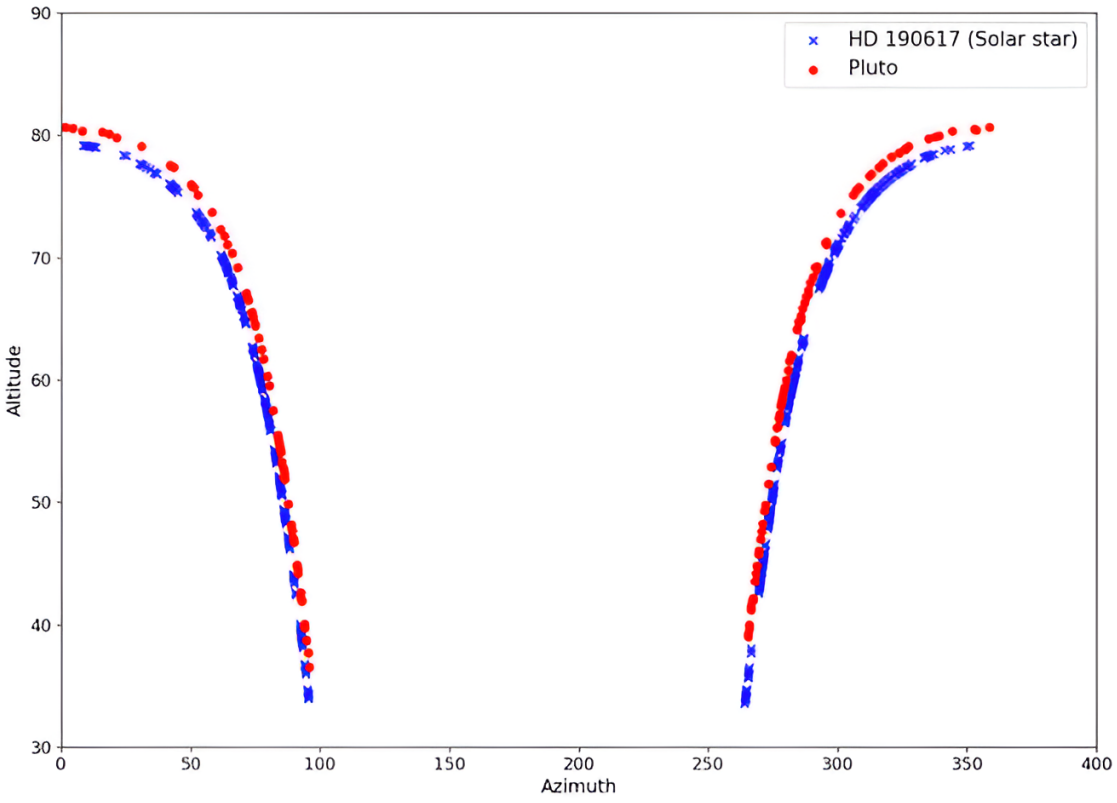

Figure 17: Plot showing the altitude angles versus azimuth angles of spectroscopic observations of Pluto (red dots) and HD 190617 star (blue crosses).

Figure 18 displays the naked-eye views of the Sun just before sunset and after sunrise. The green boxes represent the field of view for two mounting configurations: altitude/azimuth mounting and equatorial mounting. These fields of view are

separated by an angle similar to the one between the great circles passing through the middle of the Sun and the celestial pole, as well as the zenith. This angle is known as the parallactic angle [10], denoted as η in Figure 18.

The parallactic angle typically ranges from -180^o to 180^o, but at the Lesedi telescope, parallactic angles may exceed 180^o. This is due to Mookodi being on a derotator on the Nasmyth port of an altitude/azimuth telescope, with the derotator having a rotation range of 200^o. Consequently, to cover the entire 360^o, the field of view alternates between being aligned with the north-south and flipped to align with the south-north (and hence the slit too).

Figure 19 presents the histogram distribution of parallactic angles, allowing us to assess whether sufficient HD 190617 spectra cover the Pluto spectra with the corresponding parallactic angle. Areas around 180^o and just after 160^o exemplify instances where an inadequate number of HD 190617 spectra are available to cover the corresponding Pluto spectra.

The equations for calculating the parallactic angle are given by:

$$\sin(\eta) = \frac{\sin(A)\cos(\phi)}{\cos(\delta)}$$
$$\cos(\eta) = \frac{\sin(\phi) - \sin(\delta)\cos(z)}{\cos(\delta)\sin(z)}$$
$$\cos(\eta) = \frac{\sin(\phi)\sin(z) - \cos(\phi)\cos(z)\cos(A)}{\cos(\delta)}$$

where ϕ is the observer's latitude, δ is the declination of the target object (e.g., Pluto and HD 190617), z is the zenith distance (altitude $= 90 - z$), and A is the azimuth angle of the target object (e.g., Pluto and HD 190617).

[10] Meadows P.J., Solar Observing: Parallactic Angle. Link: `https://www.petermeadows.com/html/parallactic.html`

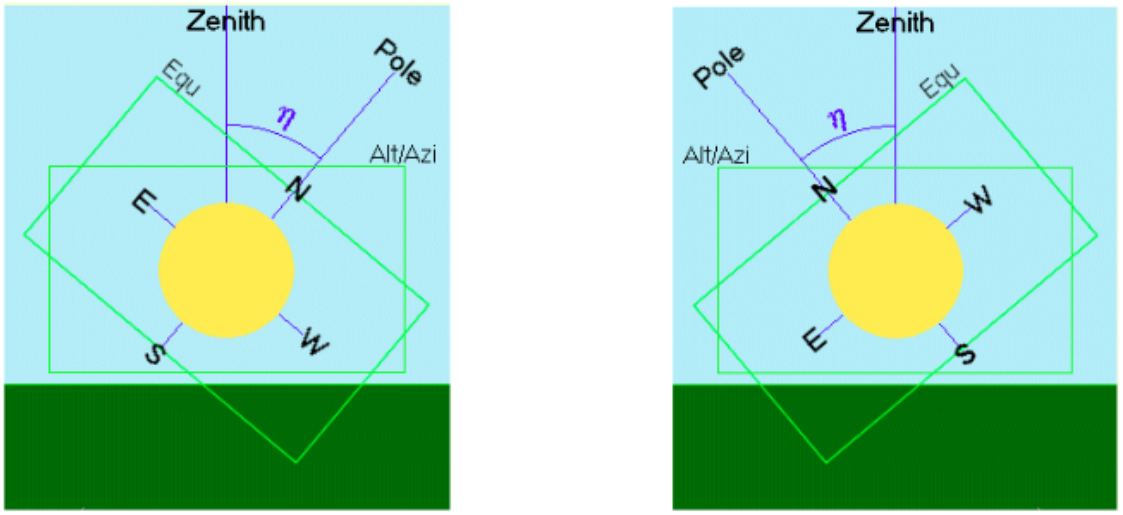

Figure 18: Naked eye views of the Sun just before sunset (figure on the left) and after sunrise(figure on the right) when the Sun is on the celestial equator. The observer is at 50 degrees North. The green rectangles are the field of views of the altitude/azimuth mountings as labeled on the figures. The North, south, west, and east directions are indicated as well. The angle η is the parallactic angle.

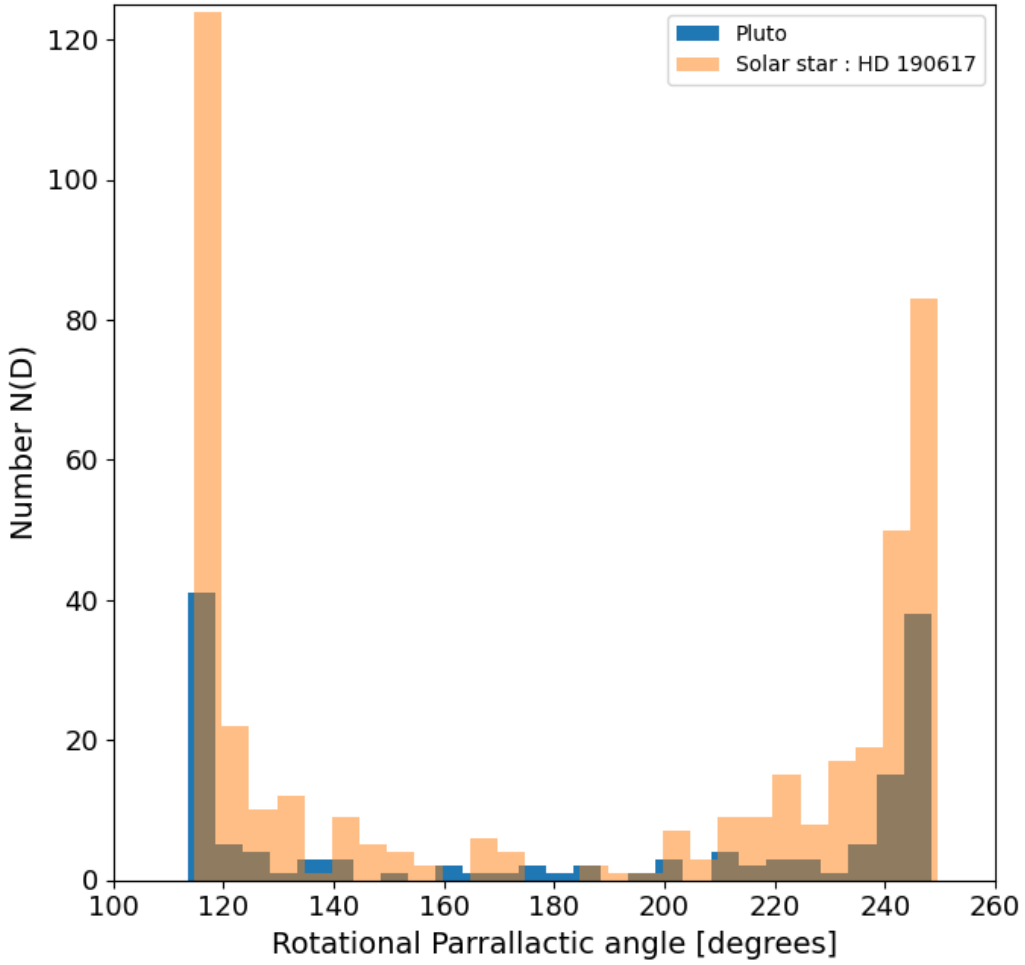

Figure 19: The plot showing the histogram distribution of the Pluto and the HD 190617 star observations. The number on the y-axis represents the number of spectra taken in each bin. The blue bins are for Pluto and the orange bins are for the HD 190617 spectra.

Airmass is a measure of the quantity of air particles that can impact incoming light along the line of sight between the observing telescope and the extremes of altitude above the telescope (Mathar [2015]). It provides insight into the absorption of light from distant objects caused by Earth's atmosphere, as well as the alteration in the angle of incoming light due to the change in refractive index from vacuum to the

refractive index of the atmosphere.

A geometric representation of airmass is illustrated in Figure 20, where z is the zenith angle from the zenith to the direction of the observed object, h is the altitude above the telescope, and x is the distance to the object. Considering this geometry, the equation to calculate the airmass is given by:

$$X = \sec(z)$$

where X represents the airmass and z is the zenith angle.

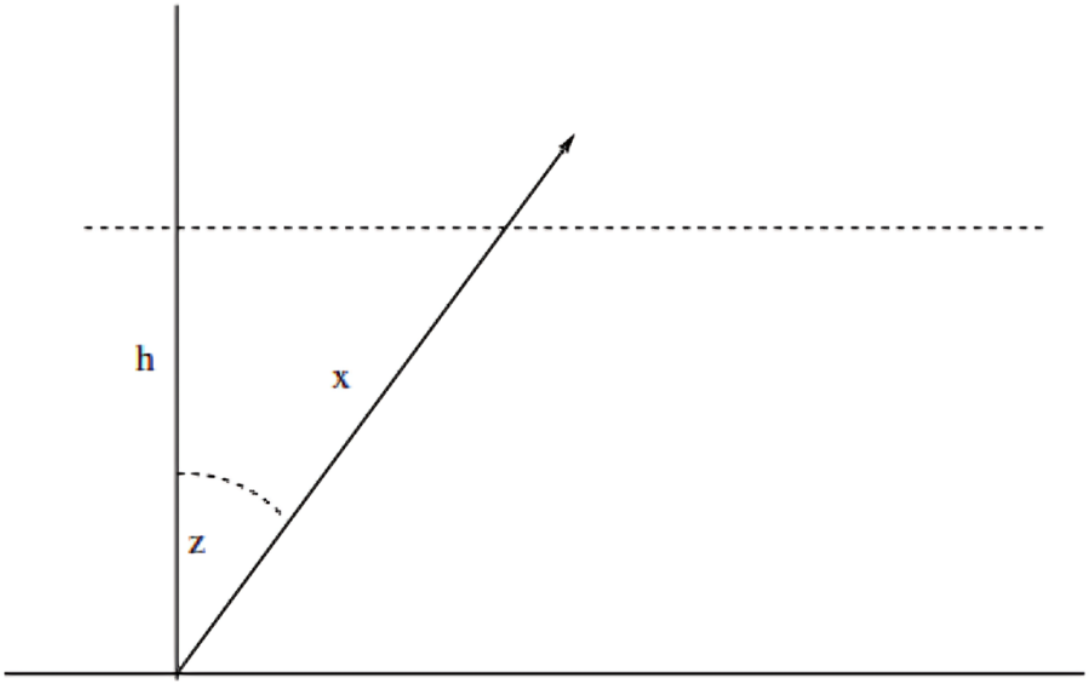

Figure 20: Flat geometry used to calculate and derive the airmass.

The spectroscopic observations conducted for Pluto and the star HD 190617 documented the corresponding airmass values, which are presented in a histogram, as illustrated in Figure 21. The distribution of airmass in the histogram reveals that nearly all HD 190617 spectra encompass the entire range of Pluto spectra, except for a specific region around an airmass value of 1.5.

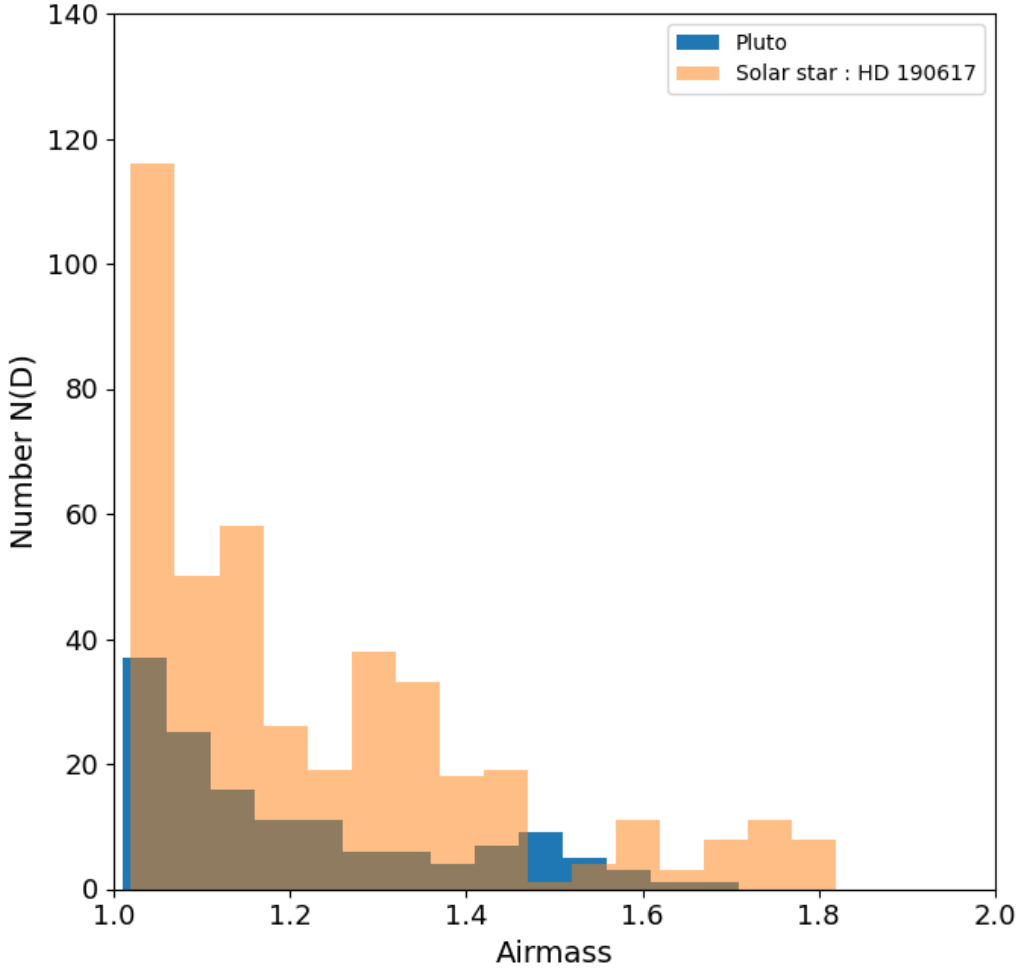

Figure 21: Airmass histogram distribution. The blue bins are for Pluto and the orange bins are for the HD 190617 star. The airmass histogram indicates that nearly all the HD 190617 spectra encompass the entire range of Pluto spectra.

A known correlation between airmass and the parallactic angle has been identified. In Figure 22, the plot illustrates the relationship between airmass and the parallactic angle for both spectroscopic observations of Pluto and the star HD 190617. As the parallactic angle decreases from 180°, there is a corresponding increase in airmass. Conversely, when the parallactic angle increases from 180°, the airmass also increases. In order to negate any effects of airmass and parallactic angle, it is important to

normalise the Pluto spectra with HD 190617 spectra taken at the same airmass and parallactic angle. Figure 22 shows that in most cases, for each Pluto spectrum, there are suitable HD 190617 spectra taken under similar conditions.

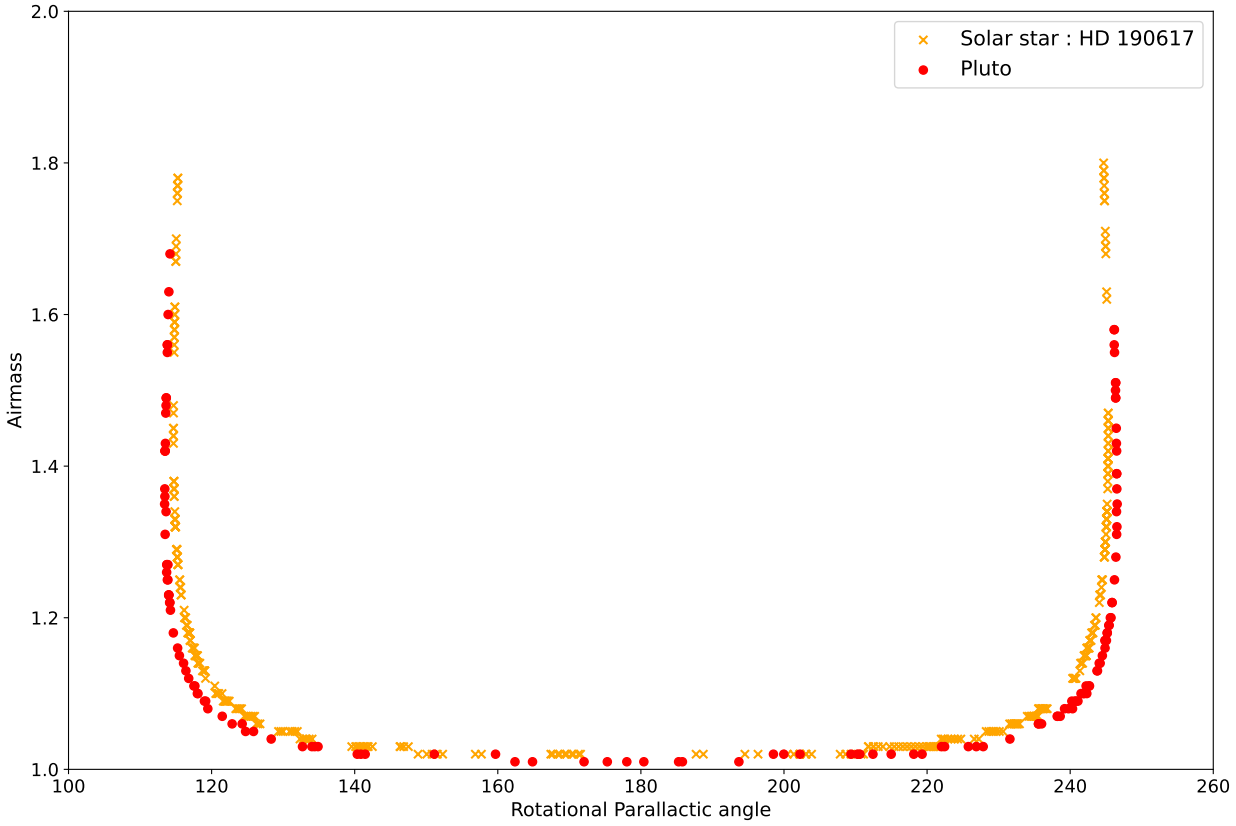

Figure 22: Plot of the airmass versus Parallactic angle for both Pluto (red dots) and the HD 190617 star (orange crosses) spectroscopic observations. The plot shows that as the Parallactic angle decreases from 180^o, the airmass increases. Conversely, as the Parallactic angle increases from 180^o, the airmass also increases.

4.2 Results

4.2.1 Spectroscopy

The reflectance spectra, derived from the spectroscopic data normalised with HD 190617 spectra taken at a similar airmass and parallactic angle (see Figure 22) using

the ASPIRED program, were then binned based on longitude coordinates.

Each longitudinal coordinate bin has a size of 50°. These bins are centered on the longitudinal coordinates from which Lorenzi et al. [2016] collected their spectroscopic data on the surface of Pluto. The respective longitude coordinates are 358.9°, 245°, 141.3°, 197.9°, 49.7°, and 103.7°. Figure 23 displays the normalised relative reflectance spectra, obtained by taking the median of the reflectance spectra within 50° longitude bins centered on the mentioned longitudes. The relative reflectance spectra were normalised at 600 nm. A spectral offset is applied to prevent the spectra from overlapping. The yellow-shaded region represents the area where the 730 nm methane ice absorption band is located. The yellow shaded region has a width of 20 nm. In Figure 23, the black dashed lines denote the positions of the telluric absorption lines, indicating that any residual signals in the spectra at these locations are likely not real.

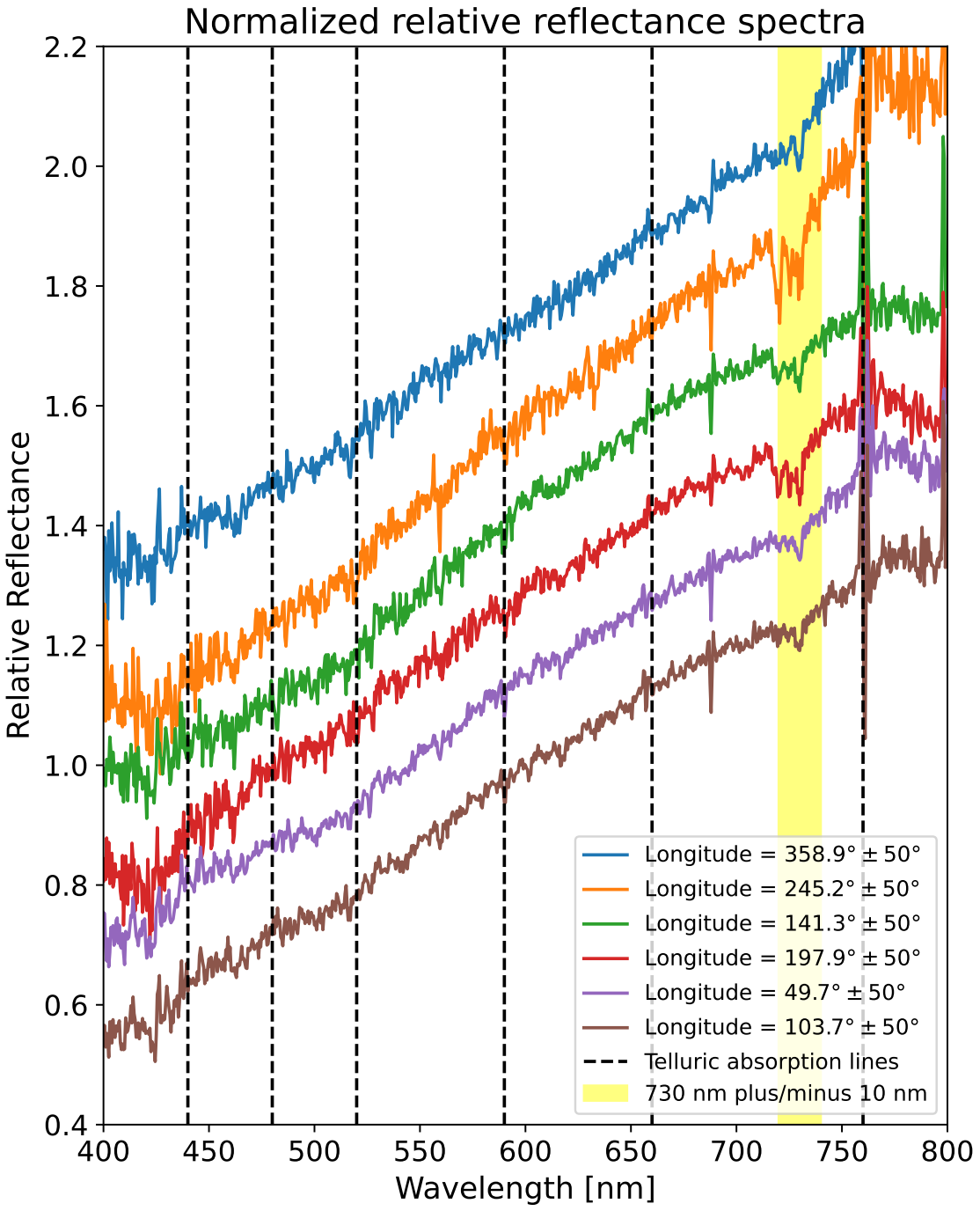

Figure 23: Plot showing the normalised relative reflectance spectra of Pluto that correspond to different sub-Earth longitudes. The spectra resulted from taking the median of multiple spectra that are within 50^o of each longitude. The yellow region on the plot covers the wavelength range from which the methane ice absorption band lies which is 730 $\pm$ 10 nm. Black dashed lines represent the locations of the telluric absorption lines.

The subsequent task involves measuring the methane ice absorption bands within 730 ± 10 nm of the relative reflectance spectra from Figure 23. To facilitate this, the continuum was initially fitted for subsequent removal. Subsequently, the continuum was normalised by dividing it by the fitted straight line, ensuring that the fluctuations in the continuum have a mean of approximately unity (1). The following step involved fitting a 2D Gaussian to obtain essential parameters such as the percentage band depth and the central mean wavelength of the 730 nm methane ice band. Figure 24 shows the resulting illustration of the process in which the methane ice absorption bands are measured.

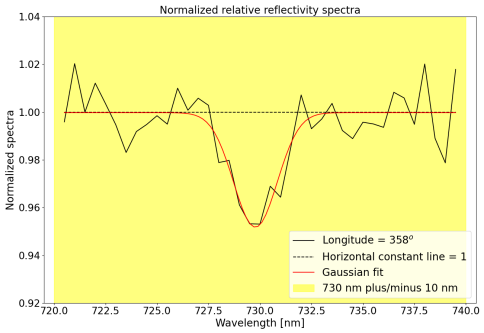

(a) Sub-Earth Longitude= 358^o

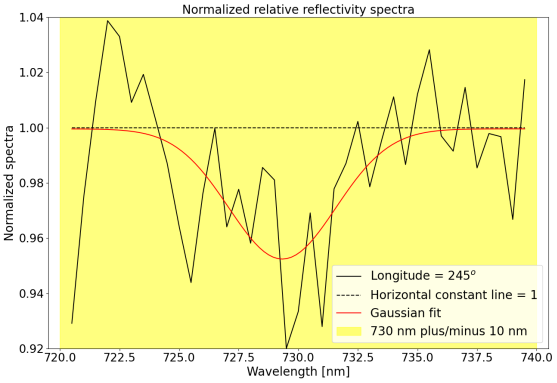

(b) Sub-Earth Longitude= 245^o

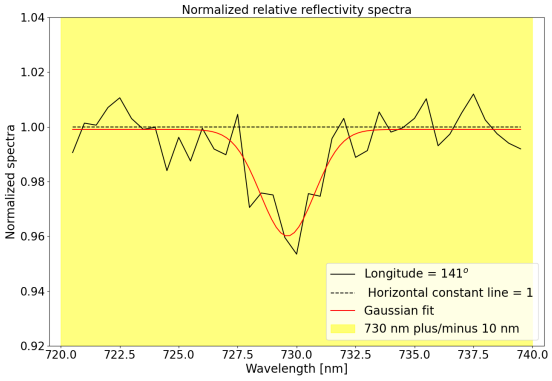

(c) Sub-Earth Longitude= 141^o

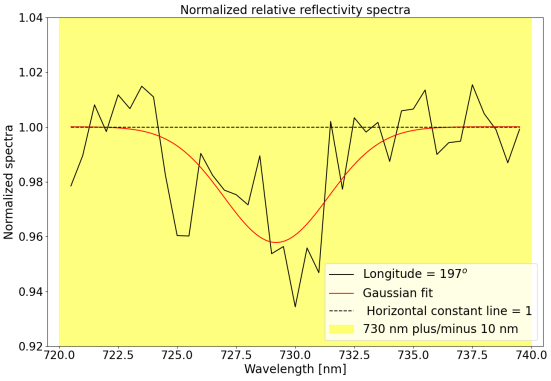

(d) Sub-Earth Longitude= 197^o

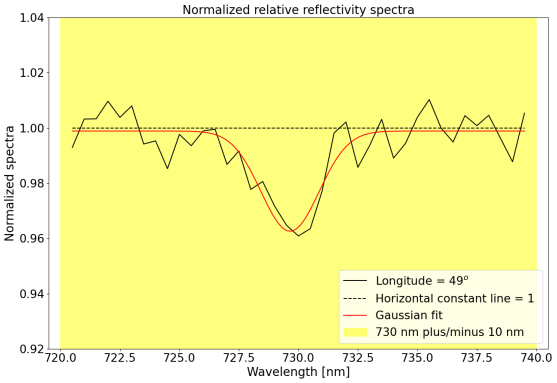

(e) Sub-Earth Longitude= 49^o

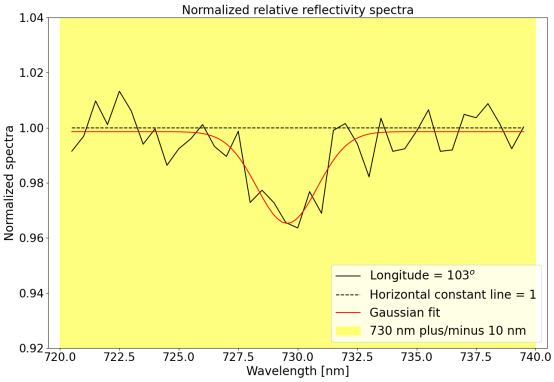

(f) Sub-Earth Longitude= 103^o

Figure 24: Continuum removed reflectance in the region between 720 nm and 740 nm. The methane ice absorption band is centered around 730 nm. The dashed black line represents the continuum level with a value of unity(1). The red curve on the plots represents the 2D Gaussian that was fitted on each absorption band after the continuum had been removed.

The results obtained from the Gaussian function fitted to all absorption bands are presented in Table 3.

Longitude	Band depth % ($\|\|Amplitude\|\| \times 100$)	Central wavelength (Mean)
358^o	4.80 ± 1.18	729.78
245^o	4.71 ± 2.54	729.33
141^o	3.89 ± 0.73	729.61
197^o	4.23 ± 1.12	729.19
49^o	3.63 ± 0.70	729.65
103^o	3.33 ± 0.73	729.56

Table 3: Table showing the percentage band depth and the central wavelength of each absorption band corresponding to each longitude. The uncertainty of the band depth percentage is the RMS of the continuum fluctuations in the absence of the dip of the absorption band.

Equation 2 illustrates the Gaussian equation employed in the analysis, where the mean (b) provides the central wavelength of the methane ice absorption band, and the amplitude (a) represents a fraction of the band depth.

$$f(x) = ae^{-\frac{(x-b)^2}{2c^2}} \tag{2}$$

To assess the inhomogeneity on Pluto in terms of the methane ice spectral band depth, one can plot the band depth values from all spectra against the sub-Earth longitude of the corresponding spectra. Figure 25 depicts this band depth versus longitude plot. The variations in methane ice band depth from Lorenzi et al. [2016] are overlaid with those from this work. Both band depth plots were fitted with a sinusoid (sine function) to observe the variation more clearly, as shown by the solid lines. The band depth variability by the Mookodi instrument is slightly different to the one by Lorenzi et al. [2016] most likely because of the difference in sub-Earth latitudes as illustrated in Figure 14 and 15 but the trend is remarkably similar. The results in Figure 25 underscore the capability of the Mookodi instrument in detecting surface composition inhomogeneity, as evidenced by the agreement between the previous work by Lorenzi et al. [2016] and these results.

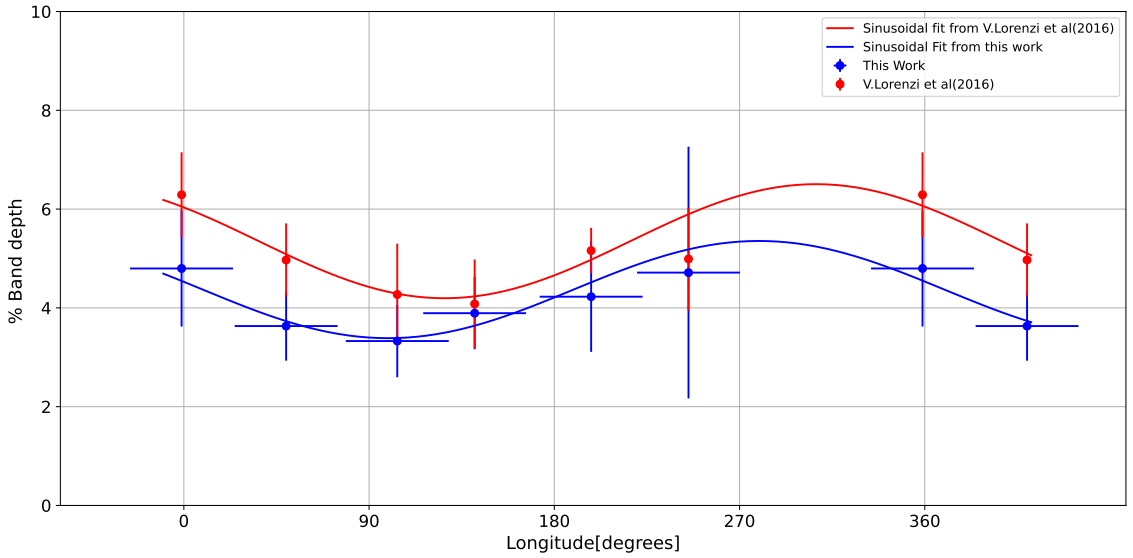

Figure 25: The plot showing the surface composition inhomogeneity in terms of the methane ice band depth plotted against longitude on the surface of Pluto. The red dots are the band depth results from Lorenzi et al. [2016]. The blue dots are the band depth results from this work. The solid lines result from fitting a simple sine trigonometric function. The plot is evidence that the Mookodi instrument is capable of detecting surface composition inhomogeneity, since the results agree within the observational uncertainty.

A residual plot, shown in Figure 26, was generated to assess the alignment between the band depth results obtained in this work and those reported by Lorenzi et al. [2016], as well as to detect any potential systematic errors. The residuals, representing the differences between the two datasets, range from $-4\,\%$ to $4\,\%$, indicating that the discrepancies are small. The error bars, reflecting the uncertainties from both this work and Lorenzi et al. [2016], show that the observed differences lie within the expected variation. This suggests that the residuals are not statistically significant. Furthermore, the reduced chi-squared value, $\chi^2/\nu = 0.96$, indicates a strong agreement between the datasets, as it implies that the deviations fall well within the expected noise levels.

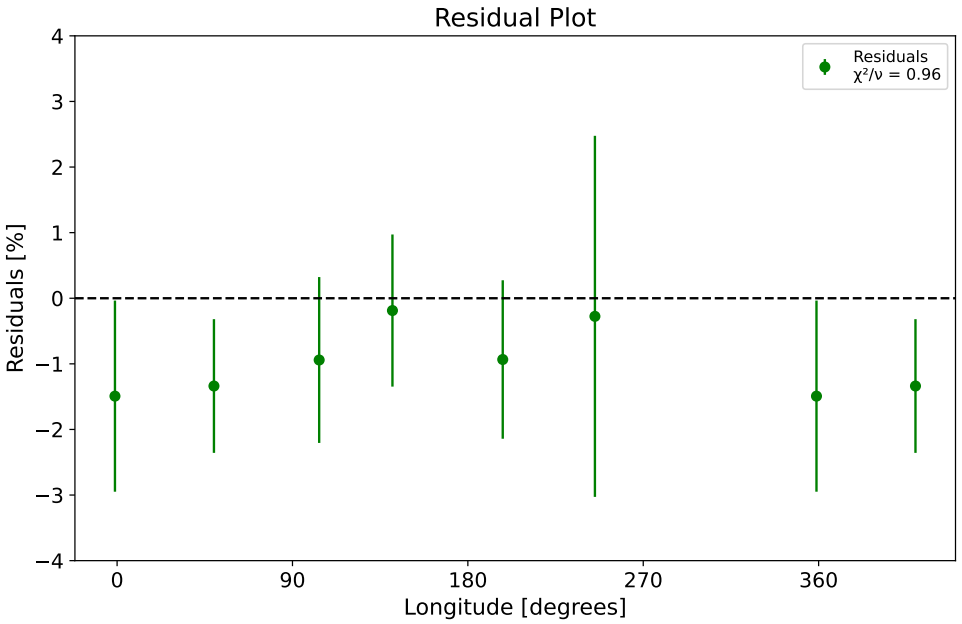

Figure 26: Residual plot comparing the band depth results from this work and Lorenzi et al. [2016]. The residuals, calculated as the differences between the two datasets, are shown with error bars representing uncertainties from both studies. The small range of the residuals ($-4\,\%$ to $4\,\%$) and the reduced chi-squared value of $\chi^2/\nu = 0.96$ indicate a strong agreement between the datasets, with deviations falling within the expected noise levels.

4.2.2 Photometry

After each spectroscopy data collection, photometric data were also collected. The photometry data were processed through the photometry reduction procedure, where the bias frame was subtracted from the raw photometry science image and divided by the flat field frame. The reduced photometric data were then processed through the PHOTOMETRYPIPELINE to obtain the magnitude brightnesses at different dates for the r-filter, i-filter, and g-filter. The main aim was to produce an $r - i$ colour plot (i.e. spectral slope) vs longitude (i.e. rotation phase). The dates of the colour data were also converted to longitudinal coordinates, following a similar approach used for the time-resolved spectroscopy analysis.

Figure 27 shows the generated plot of the r-i colour vs longitude. In this figure, the r-i colour from the observations is overplotted with the spectral slope measurement from the Lorenzi et al. [2016] paper, which spans wavelengths of 0.57 *to* 0.7 μm.

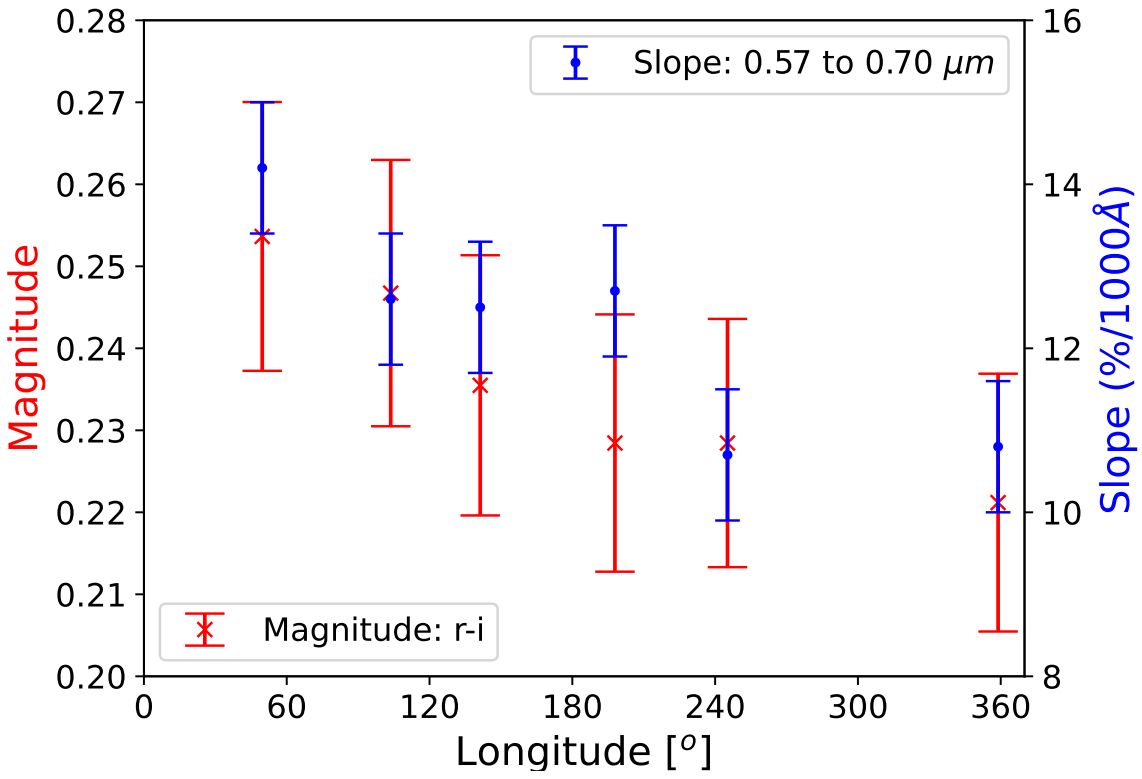

Figure 27: Plot showing the $r - i$ colour (in red crosses) and the spectral slope measurements, from the Lorenzi et al. [2016] paper, as a function of longitude. The two different data sets show an agreement. The reason for comparing the two data sets is because the $r - i$ colour transmittance overlaps with the spectral slope wavelength range of 0.57 to 0.7 μm.

The comparison between the two photometric datasets was made because the $r - i$ colour transmittance, as seen in Figure 28, overlaps with the spectral slope wavelength range (0.57 to 0.7 μm) of the Lorenzi et al. [2016] data.

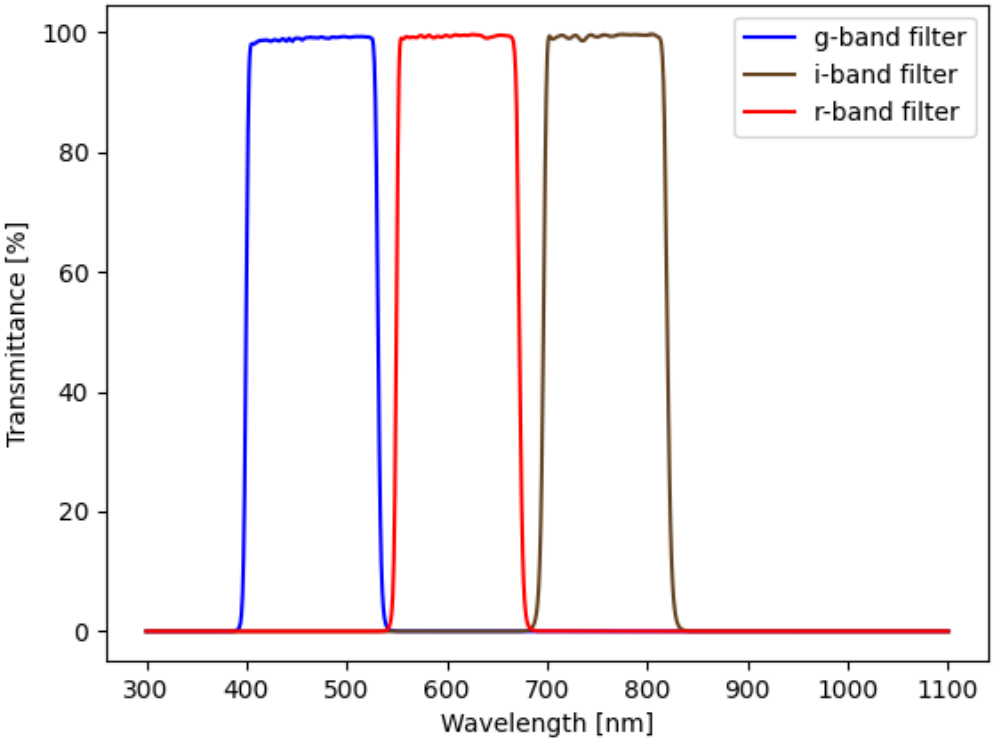

Figure 28: Plot of the different band filters which are the g, r and i. The overlap between the r (in red) and i (in brown) is where the $r - i$ colour lies (about 660 *to* 720 nm) which which approximately overlaps with the Lorenzi et al. [2016] spectral slope wavelength range (between 0.57 *to* 0.70 μm).

From the plot in Figure 27, the spectral slope data (blue dots) from the Lorenzi et al. [2016] data agrees with the $r - i$ colour plot (red crosses). This means that the Mookodi instrument can perform time-resolved photometry for the approach of detecting surface composition inhomogeneity via spectral slope analysis.

4.3 Discussion of results and comparison with the findings of Lorenzi et al. [2016]

The band-depth results from the time-resolved spectroscopy data collected by the Mookodi detector do agree with those of Lorenzi et al. [2016] as shown in Figure 25. The band depth trends of the two curves are not exactly superimposed, likely because of the difference in the sub-Earth latitude as illustrated on Figure 14 and

Figure 15 . The trend of the time-resolved photometry data agrees with the trend of the spectral slope measurements from Lorenzi et al. [2016].

4.4 Conclusion of TEST CASE 1

Based on the analysis of results from the data collected on Pluto using the Mookodi instrument of the Lesedi telescope, the Mookodi detector can perform time-resolved spectroscopy (via the analysis of methane ice band-depth variability) and time-resolved photometry (via spectral slope analysis) as an approach to detect surface composition inhomogeneity on the surface of Pluto.

5 TEST CASE 2: 2005 EK70

Background

2005 EK70 is a near-Earth Asteroid that orbits the sun every 343 days. Its closest distance to the sun is 0.83 AU and its furthest distance from the sun is 1.09 AU. It has a Minimum Orbit Intersection Distance (MOID) of 38.12 Lunar Distances (LD). The closest approaches of asteroid 2005 EK70 to Earth occur on the following dates: 27 August 2023, at a distance of 69.88 LD; 20 February 2024, at 37.70 LD; 23 July 2024, at 133.92 LD; 22 February 2025, at 126.35 LD; and 17 September 2038, at 115.56 LD. Using the JPL Horizon's ephemeris calculating tool [11], it was determined what the RA and Dec of the asteroid was at the time of the planned observations. The precise coordinates could be determined at the time of the planned observations; however, for the observations performed on 24 February 2024, the RA and Dec were approximately $08:42:00$ and $-04:17:00$, with a sky rate of about -500 arcseconds per hour in both RA and Dec. Time-series spectroscopy was performed on the object to test the Mookodi detector's ability to detect surface composition inhomogeneity on a fast non-sidereal moving object. A summary table of the observations of 2005 EK70 conducted with the Lesedi telescope is provided in Appendix B.

Asteroids, unlike stars, do not emit light. Instead, they reflect light emanating from nearby sources, such as the Sun in our Solar System. This reflected light produces a specific type of spectrum known as the reflectance spectrum. Analysing the reflectance spectra from asteroids unveils valuable information about the underlying minerals constituting these objects. The unique reflective properties of various minerals result in distinct spectral signatures, enabling the determination of the composition of asteroids.

[11] JPL Horizons. Link: `https://ssd.jpl.nasa.gov/horizons/`

To determine the taxonomic type of asteroids, their reflectance spectra are compared to the average spectral behaviours of the high quality spectra from the Bus-DeMeo taxonomic classification scheme. Figure 29 shows the average Bus-DeMeo spectra (DeMeo et al. [2009]). The taxonomic classification is divided into classes which are S-complex class (S-, Sa-, Sq-, Sr- and Sv-type), C-complex class (B-, C-, Cb-, Cg-, Cgh- and Ch-type), X-complex class (X-, Xc-, Xe-, Xk- and Xn-type) and end members (D-, K-, L-, T-, A-, O-, Q-, R- and V-type) class. Some of these classes like the O- and R-type classes overlap significantly with the other classes. Therefore, the classes usually considered when classifying asteroids are S-complex, C-complex, and X-complex, while the end members generally considered are D-, Q-, and V-type.

S-complex asteroids, composed primarily of silicates like olivine and pyroxene, have moderate albedos and distinct absorption features, linking them to ordinary chondrite meteorites (Burbine et al. [2024]). In contrast, C-complex asteroids are characterized by low albedos and featureless spectra that indicate a high carbonaceous content. The X-complex encompasses a diverse range of asteroids, including both metallic and carbon-rich types, with spectra that may lack distinctive features but nonetheless suggest a variety of compositions. D-type asteroids possess red-sloped spectra and low albedos, implying the presence of organic-rich and volatile materials. Q-type asteroids exhibit strong absorption bands similar to those of unweathered ordinary chondrites, signifying less space weathering and relatively fresh surfaces. V-type asteroids, with basaltic compositions, are closely associated with differentiated bodies like Vesta, exhibiting clear absorption features related to pyroxenes.

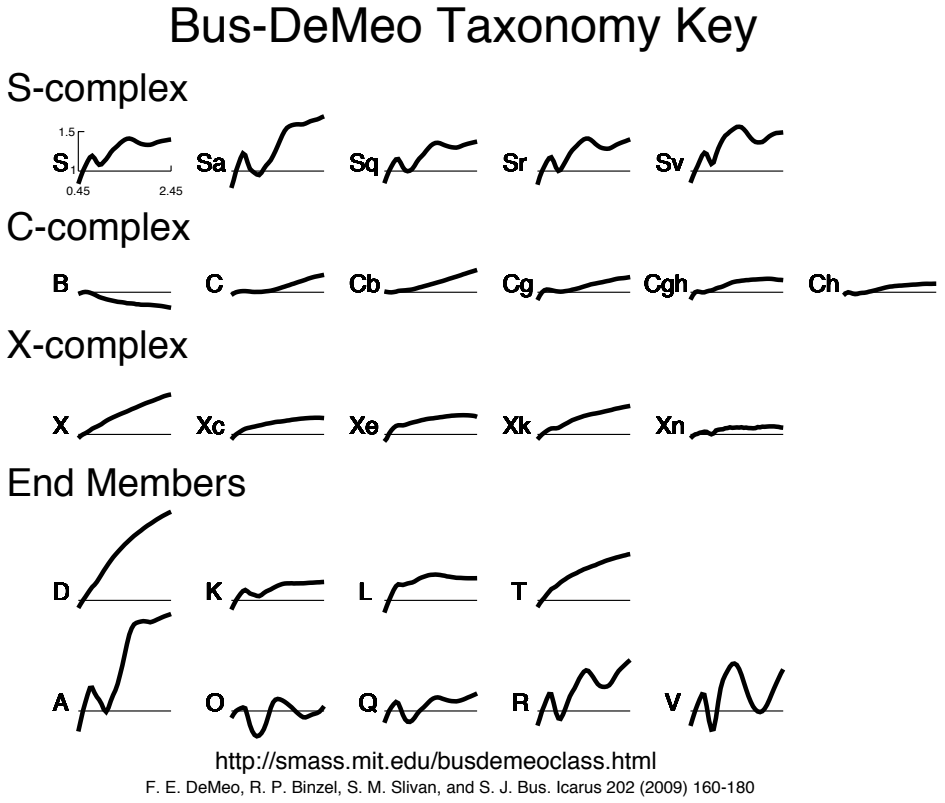

Figure 29: Average Bus-DeMeo spectra (in solid bold lines) of the S-complex class (S-, Sa-, Sq-, Sr- and Sv-type), C-complex class (C-, Cb-, Cg-, Cgh- and Ch-type), X-complex class (X-, Xc-, Xe- and Xk-type) and end members (D-, K-, L-, T-, A-, O-, Q-, R- and V-type). The horizontal axis represents the wavelength range from visible to near-infrared spectrum (0.45 to 2.45 μm), with the horizontal axis aligned where the vertical axis has a reflectance value of 1. Source: DeMeo et al. [2009].

5.1 Observing Strategy

On 21st and 22nd February 2024, r-band photometric data were collected with a few 4-second exposures but mostly of 10-second exposures. Initial observations were conducted with a few 4-second exposures, but it was determined that the exposure time could be increased without saturating the detector. Consequently, longer exposure times were used for the remainder of the observations. However, the exposure times were not extended excessively to avoid streaking of the background stars during non-sidereal tracking, as the photometry pipeline (PP) does not handle streaked

sources. There are 317 raw photometric images collected on 21 February 2024 and 784 on the 22nd of February 2024, which makes a total of 1101 raw photometric images. After the collection of data, poor quality photometric images were discarded among these 1101 raw photometric images to insure precise brightness measurements. On 24th February, there are a total of 25 60-second exposure spectroscopy science images of 2005 EK70 and 17 5-second exposure spectroscopy science images of a standard star HD 76151.

From the Pluto observations, it was realised how important the parallactic angle can be in spectral slopes, so for the spectroscopic observations for Test Case 2, the decision was made to conduct the observations manually, which allowed access to the backend control software of the telescope, enabling adjustments to the parallactic angle for the derotators. This is not possible in robotic mode. The observing strategy was to first, identify a future time approximately 10 minutes ahead into the future because that is roughly the time it took us to manually point the telescope and take an acquisition image and identify the target after taking a test image. Using the future time, The RA and Dec were obtained from JPL and the telescope was then pointed at those RA and Dec coordinates. The parallactic angle for the time, location, and telescope pointing was calculated (Lesedi's TCS does display this), and the sky-angle of the derotator was adjusted to align the slit along the parallactic angle. The camera was set to semi video-mode via short (e.g 1 second) continued exposures and the field was monitored until the moving target appeared in the frame and was identified (at the expected RA and Dec location around the future selected time). The telescope was then placed in non-sidereal tracking mode, by entering the non-sidereal rates from JPL into TCS.

The rates were adjusted until the target remained stationary during repeat exposure mode. The telescope was nudged in small steps of RA/Dec while non-sidereal tracking was activated at the correct rate until the target was located on the "magic pixel" corresponding to the spectrograph slit location. The instrument was placed in spectrograph mode (i.e., the grism and slit were moved into the beam), and the camera settings were adjusted for the desired spectroscopic exposure. Repeated exposures were taken, monitoring the maximum count on spectrum traces. When counts began to drop, the instrument was returned to imaging mode. The sky angle was tweaked to re-align the slit to the parallactic angle, and with short repeat exposures, the target's location was readjusted with small nudges to bring it back onto the "magic pixel". The process was then repeated by placing the instrument back in spectrograph mode and adjusting the camera settings for the desired spectroscopic exposure.

5.2 Apparent Magnitude versus Absolute Magnitude

To assess whether the time-series spectroscopy covered a full rotation period, additional photometric data were collected with Mookodi to determine a rotation period of 2005 EK70 via light-curve analysis. Archival data from the Minor Planet Center (MPC) were also included. Since these observations covered slightly over 3 months, the viewing geometry can change. Since additional photometric data of 2005 EK70 were collected, and the viewing geometry of Near-Earth Asteroids (NEAs) can change significantly over a short period of time (for example, over the course of a few days), some additional processing of the obtained photometry (i.e., the apparent magnitudes) is necessary. The apparent magnitude indicates how bright the object appears to an observer on Earth. To measure the true brightness of an asteroid, the apparent visual magnitude must first be converted to the reduced magnitude, $H(\alpha)$, in order to account for the effects of distance. Equation 3 (Dymock [2007]) can be used to calculate the reduced magnitude, $H(\alpha)$:

$$H(\alpha) \; = \; V \; - 5log(r\Delta) \tag{3}$$

where V is the observed magnitude, r is the distance of the asteroid from the Sun, Δ is the distance of the asteroid from the Earth and α is the phase angle (Sun/Asteroid/Earth angle).
Figure 30 shows a visual presentation of an asteroid that is at some distance from the Earth and the Sun. The geometry of this Sun-asteroid-Earth reveals a subtended angle called the phase angle α. The reduced magnitude was used to further calculate the true brightness of the asteroid if it were placed 1 AU from the Earth and 1 AU and fully illuminated. The absolute magnitude can be calculated from Equation 4:

$$H \; = \; H(\alpha) \; + \; 2.5log[(1-G)\phi_1(\alpha) + G\phi_2(\alpha)] \tag{4}$$

where :

$$\phi_i(\alpha) \; = \; exp\{-A_i(tan(\frac{1}{2}\alpha))^{B_i}\} \tag{5}$$

$i = 1$ or 2, $A_1 = 2.33$, $A_2 = 1.87$, $B_1 = 0.63$, and $B_2 = 1.22$. α is the phase angle in degrees. G is the slope parameter. this equation only predicts accurate H magnitudes if the phase angle is below 120°.

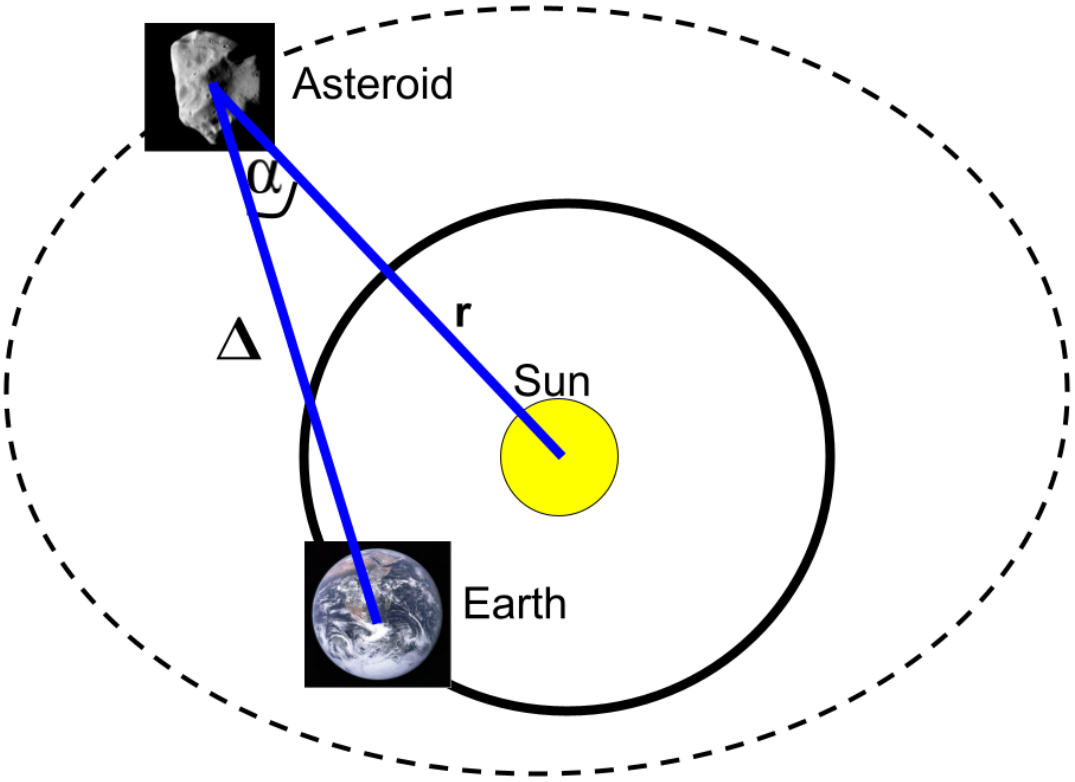

Figure 30: Artistic illustration showing a drawing of the Sun-asteroid-Earth system. The phase angle, α , is the subtended angle between the Δ (distance of the asteroid from the Earth) and r (distance of the asteroid from the Sun).

5.3 Results

5.3.1 Light curve and rotation period estimations

Photometric data from databases were collected to calculate the rotation period of the asteroid 2005 EK70, as the full length of the observation time in database surveys spans days to weeks. All the observed data are plotted in Figure 31, where the vertical axis represents the observed magnitude and the horizontal axis represents time in Modified Julian days (MJD).

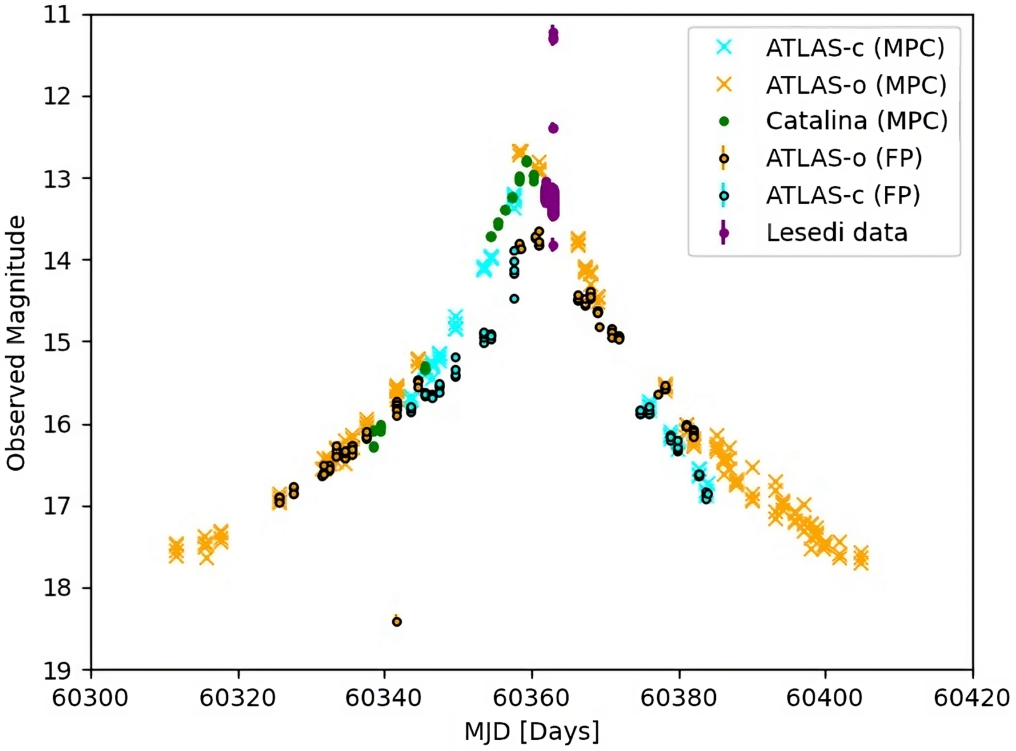

Figure 31: Plot showing the observed magnitude light curve of the available data. Orange crosses: ATLAS data (from MPC) from the *o*-filter. Cyan crosses: ATLAS data (from MPC) from the *c*-filter. Green dots: Catalina Sky Survey data (from MPC). Orange dots with black borders and errorbars: Forced Photometry (FP) ATLAS data from the *o*-filter. Cyan dots with black borders and errorbars: Forced Photometry ATLAS data from the cyan filter. Purple dots with errorbars: Lesedi data.

The observed magnitude data were converted to absolute magnitude by removing the effects of heliocentric distance, distance from the Earth, and phase angle. The equations used to convert the observed magnitude into absolute magnitude are presented in equations 3 and 4. Figure 32 shows a light curve of the overall photometry data in absolute magnitudes (H). It was noted that the ATLAS data, taken through forced photometry, exhibited a significant drop, while the data from MPC did not show such a drop in brightness. This led to the speculation that the object was streaked in photometric observations, causing a substantial drop at closest approach to Earth when the sky-rate was the highest. The Forced Photometry (FP) server

cannot handle streaked objects. Therefore, it is crucial to avoid performing forced photometry when the object is streaked in the data. Consequently, the forced photometry ATLAS data were discarded, and the MPC data were used to measure the rotation period of the asteroid 2005 EK70.

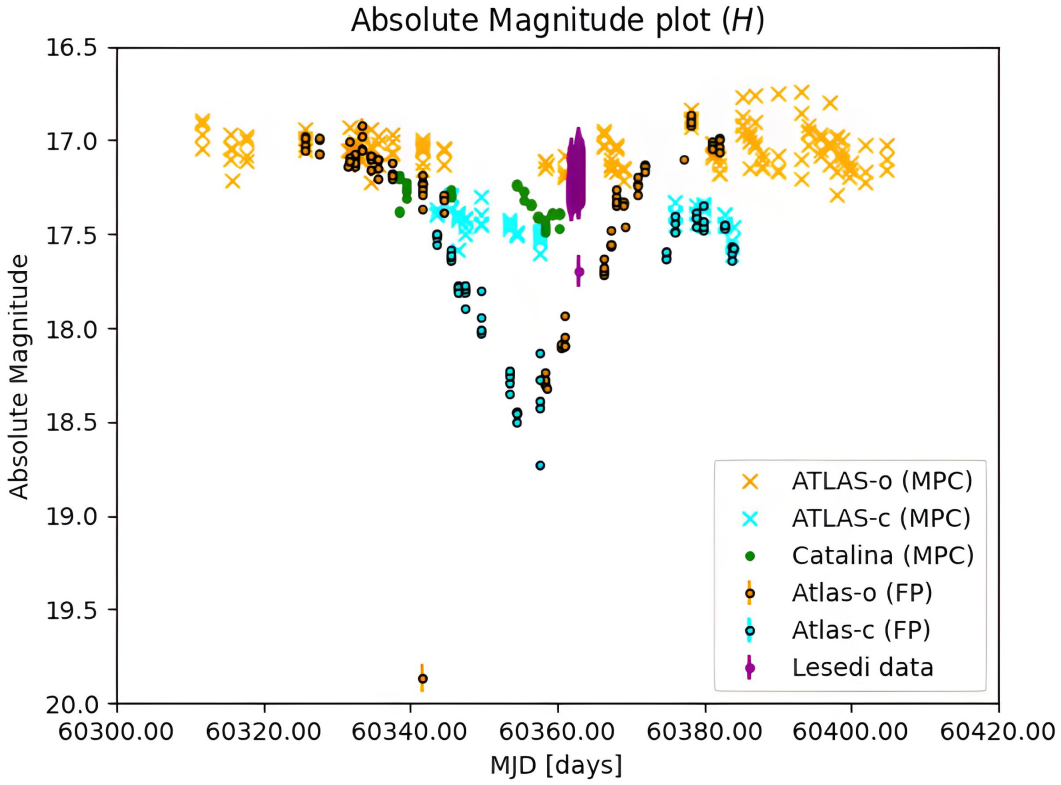

Figure 32: Plot showing the absolute magnitude light curve of the available data. Orange crosses: ATLAS data (from MPC) from the *o*-filter. Cyan crosses: ATLAS data (from MPC) from the *c*-filter. Green dots: Catalina Sky Survey data (from MPC). Orange dots with black borders and errorbars: Forced Photometry (FP) ATLAS data from the *o*-filter. Cyan dots with black borders and errorbars: Forced Photometry ATLAS data from the *c*-filter. Purple dots with errorbars: Lesedi data.

Colour corrections were performed on the photometric data, and they were normalised relative to the ATLAS data (from MPC) from the *o*-filter. Figure 33 shows the final photometric plot after the colour corrections, including the Lesedi data that were collected.

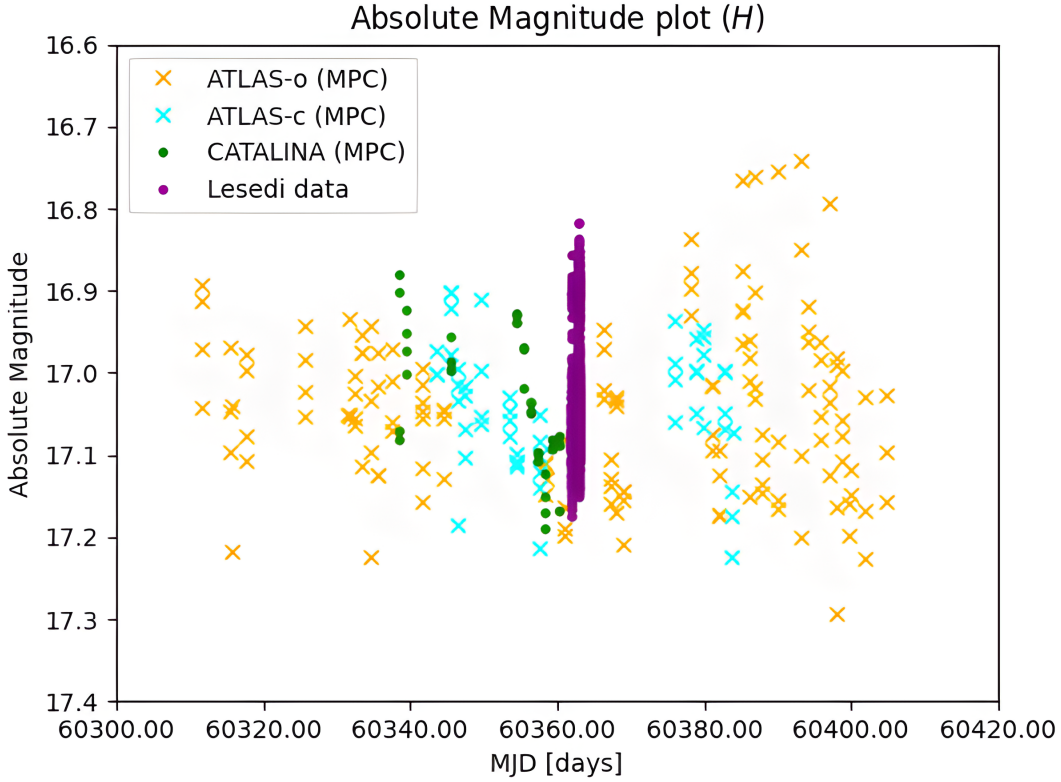

Figure 33: This is the plot resulting from removing the streaked ATLAS data from forced photometry and performing colour corrections using the ATLAS *o*-filter MPC data as a reference. The Lesedi data have also been added in addition to the data from the previous plot after colour correction.

The Lomb-Scargle periodogram method (Lomb [1976] and Scargle [1982]) was used on the photometric data to calculate the rotation period of the asteroid 2005 EK70. The Lomb-Scargle periodogram is used to detect periodic signals (or periodicity) in unevenly sampled time-series photometric data. It computes power at different frequencies, which correspond to potential periods of variation in the data. For each frequency, the Lomb-Scargle periodogram algorithm calculates a measure of spectral power, representing the strength of the periodic signal at each tested frequency. The photometric data were passed through Lomb-Scargle, and the output plot is the power versus period (in hours), as shown in Figure 34. The Lomb-Scargle plot reveals two peaks, with the highest power peak corresponding to an approximate period value of 2.17 ± 0.0021 hours. The Lomb-Scargle periodogram yields the period of the light curve; however, the actual rotation period of the asteroid is twice the value

obtained, i.e., 4.34 ± 0.0021 hours is the rotation period of 2005 EK70.

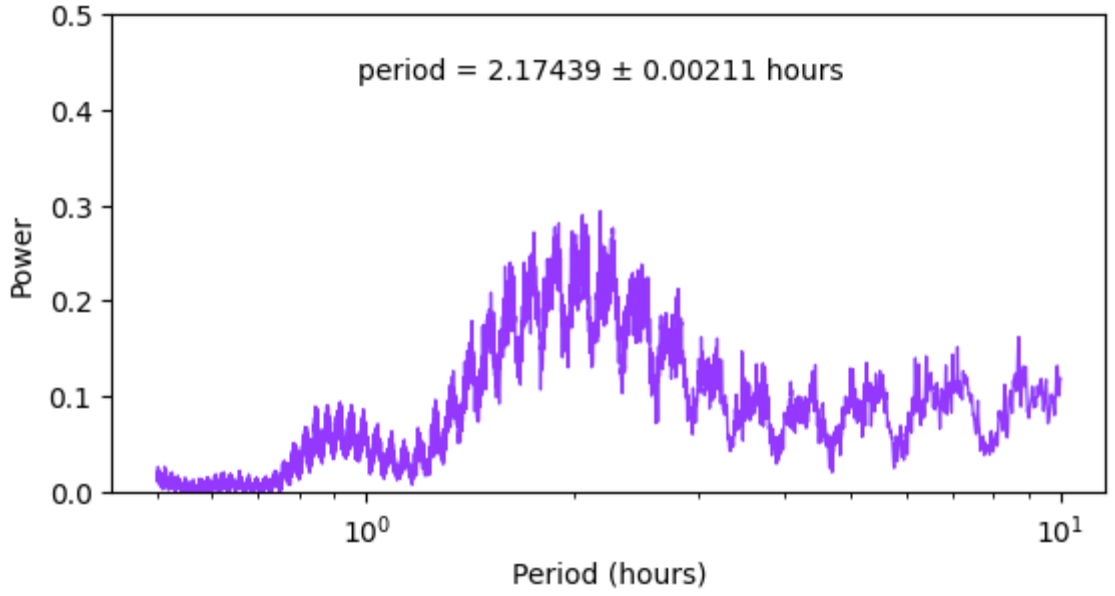

Figure 34: This is the resulting periodogram power plot after using Lombscargle. This is a plot of Power versus Period (in hours). The period measured is indicated on the plot and it is 2.17 ± 0.0021 hours. The Lomb-Scargle periodogram yields a light curve period; however, the actual rotation period of the asteroid is 4.34 ± 0.0021 hours, which is twice the value obtained from the light curve.

A phased light curve was then generated using the rotation period of 4.34 ± 0.0021 hours as shown on Figure 35. The black dots in the plot represent the normalised photometric data according to the *o*-filter ATLAS data that is folded using a period of 4.34 ± 0.0021 hours. Additionally, a Fourier fit was applied to the folded photometric data using Equation 6. The red curve represents the Fourier series fit.

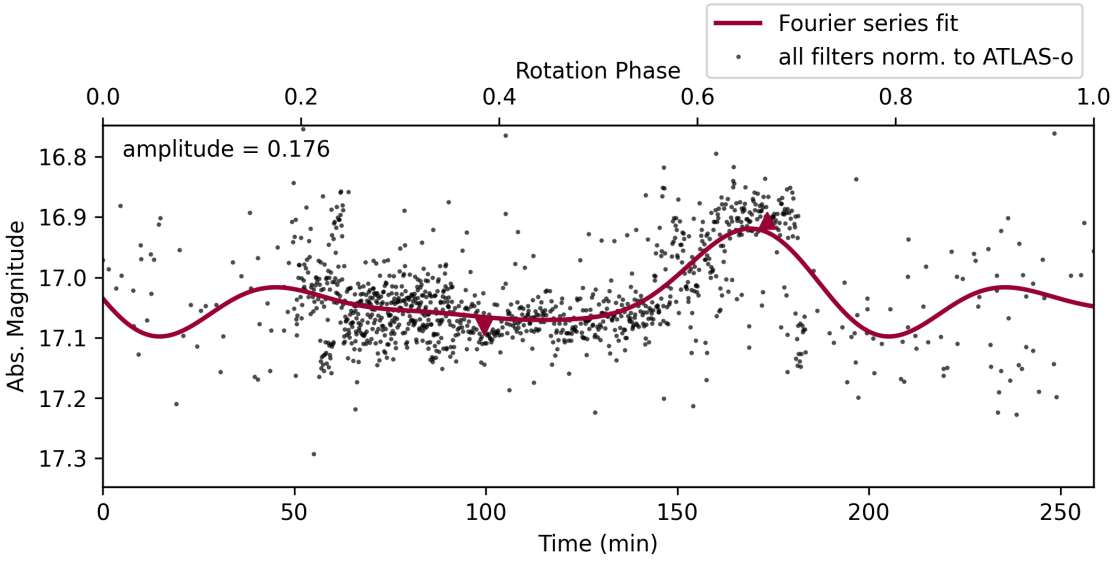

Figure 35: This is a folded light curve plot after applying the determined rotation period of the asteroid which is 4.34 ± 0.0021 hours. The mean absolute magnitude brightness of the asteroid is $H = 17.03 \pm 0.002$ magnitudes. On the plot, a Fourier fit solution is overplotted (in red).

$$f(t) \approx \frac{a_0}{2} + \sum_{n=1}^{4} \left(a_n \cos\left(\frac{2\pi nt}{T}\right) + b_n \sin\left(\frac{2\pi nt}{T}\right) \right) \tag{6}$$

5.3.2 Time series spectroscopy

All the raw spectra collected for 2005 EK70, in the form of counts versus wavelength, were used to calculate the median of all the raw counts spectra. Similarly, the collected HD 76151 (standard star) raw spectra taken at a close observing time to the 2005 EK70 raw spectra were used to calculate the median spectrum. The median counts spectrum of 2005 EK70 was then normalised by dividing it by the median of the HD 76151 counts spectra to obtain the reflectance spectrum of 2005 EK70. Figure 36 shows the final median reflectance spectrum of 2005 EK70. The Bus-DeMeo mean spectral classifications for S-type, Sq-type, and Sv-type asteroids are overplotted on the same figure. The figure indicates that 2005 EK70 has characteristics similar to those of Sv-type asteroids.

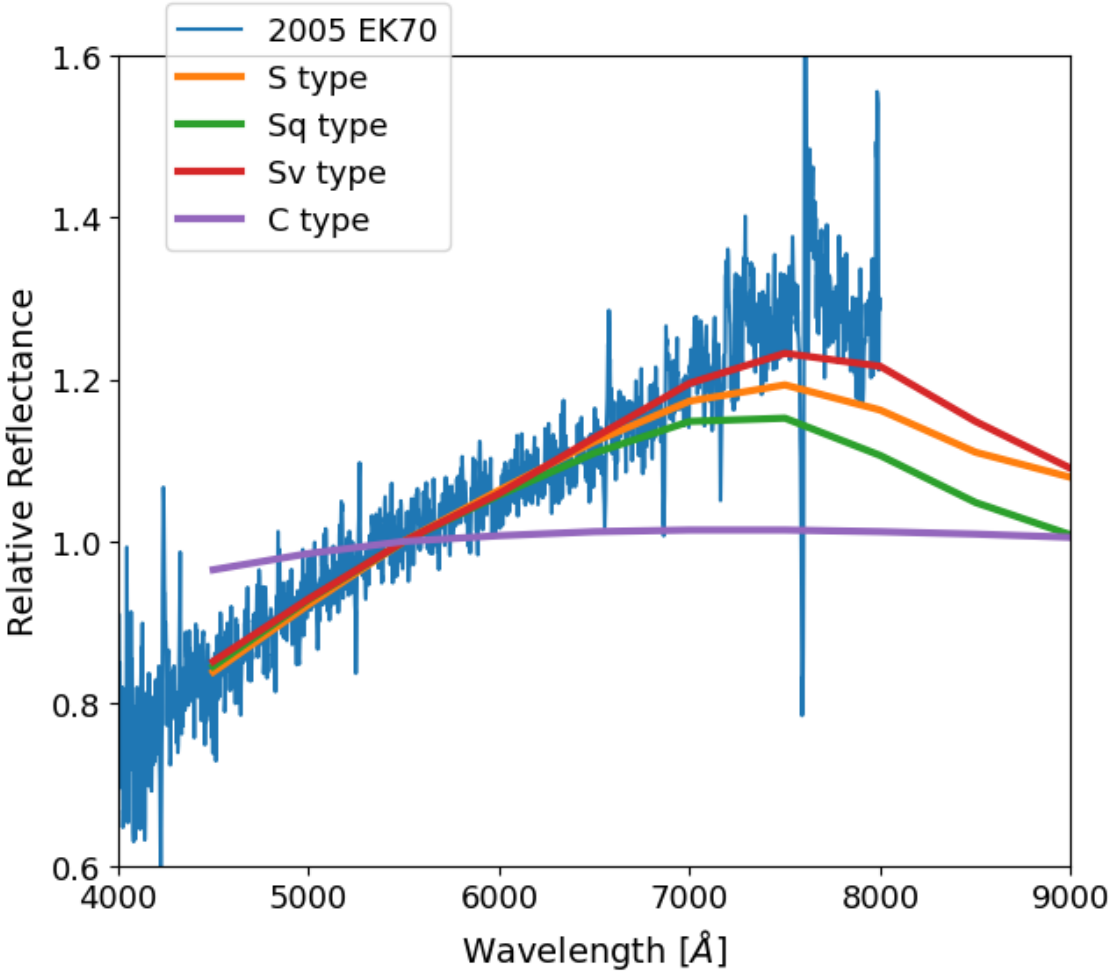

Figure 36: This is a plot of relative reflectance versus wavelength. The plot shows the median reflectance spectrum of 2005 EK70 (in blue) normalised at 5500 Å. The large spikes visible in the blue spectrum correspond to the locations of the telluric lines. The other lines are the Bus-DeMeo asteroid taxonomy classifications which are S-type (in orange), Sq-type (in green), Sv-type (in red), and C-type (in purple). The spectral range of 2005 EK70 is between 4000 Å and 8000 Å. The spectral range for the shown taxonomy spectra is between 4500 Å and 9000 Å.

Binzel et al. [2019] classified 2005 EK70 as an Sq-type asteroid using a wavelength range of 0.4 to 2.5 μm, observed through the MITHNEOS (MIT-Hawaii Near-Earth Object Spectroscopic Survey) program. The Sq-type and S-type mean spectrum agree with the 2005 EK70 reflectance spectrum at a wavelength range less than about 7000 Å and then deviates above 7000 Å. The mean spectrum of C-type asteroids

does not agree at all with the reflectance spectrum of 2005 EK70, indicating that the asteroid is almost certainly one of the S-complexes. The letter S on Sv means that the asteroid 2005 EK70 is a silicaceous or stony-iron meteorite. Sv-type asteroids [12] have a moderate albedo and features at 1 μm and 2 μm similar to V class, but shallower at 1 μm. The spectra were divided into groups of five based on observation times, and the median of each group was calculated. The time given for each group corresponds to the observation time of the median spectrum at the center of the group.

Each calculated median spectrum of five spectra in each group was plotted on a single plot, as shown in Figure 37. In this Figure, four median spectra are shown with offsets to observe any changes in the spectral shape. The spectral shape appears not to change, indicating that either the detector is not sensitive enough to detect any change or that there was no intrinsic inhomogeneity present in the asteroid, with the latter being the most plausible. The areas between $4000 < X < 4500$ Å and $7500 < X < 8000$ Å are not considered for observable changes due to the limited throughput in these areas, based on the design of the spectrograph.

[12] https://vissiniti.com/asteroid-classification/

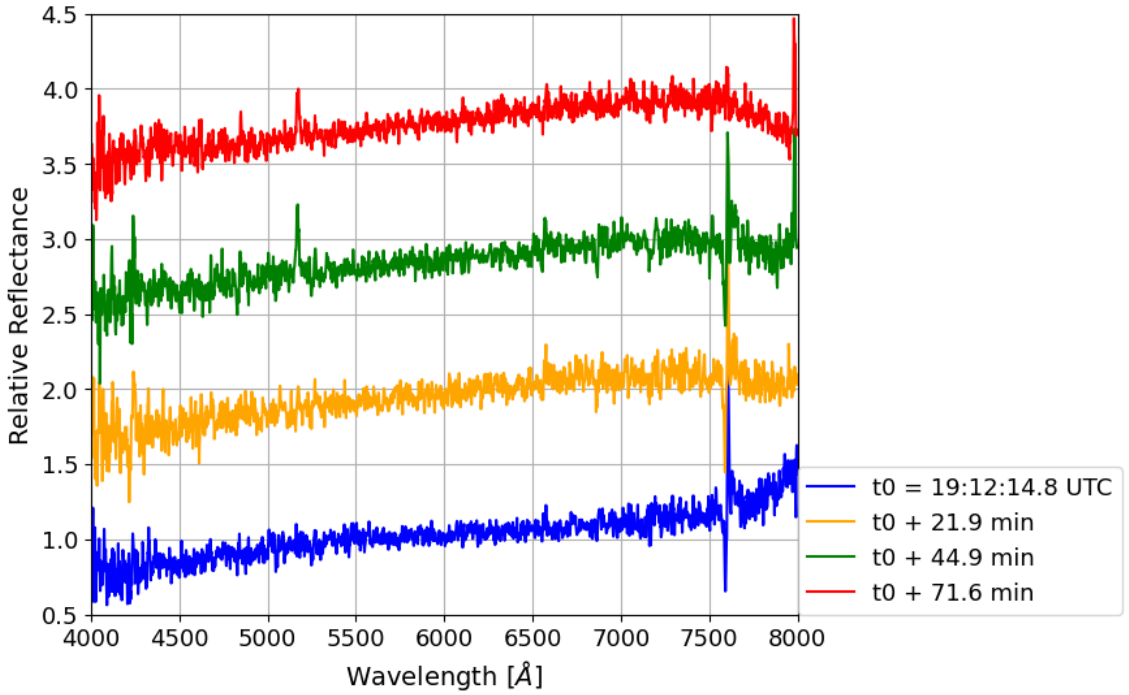

Figure 37: This is a plot of relative reflectance versus wavelength (in Å).This is the plot of median spectra of different sets of times. The first median spectrum was taken at $t0 = 19:12:14.8$ UTC, the second median spectrum was taken 21.9 minutes ahead relative to $t0$, the third median spectrum was taken 44.9 minutes ahead relative to $t0$ and the forth median spectrum was taken 71.6 minutes ahead of $t0$. The asteroid appears to not have any change in the spectral shape with changing time and therefore no surface composition inhomogeneity was detected. The large spikes visible in the spectra correspond to the locations of the telluric lines and can be disregarded when comparing the median spectra.

To do a more quantitative analysis, straight lines were drawn were fitted to each of the median spectra to observe how the gradient changes over time between a wavelength range of $4000 < X < 4500$ Å and $7500 < X < 8000$ Å, as shown on Figure 38.

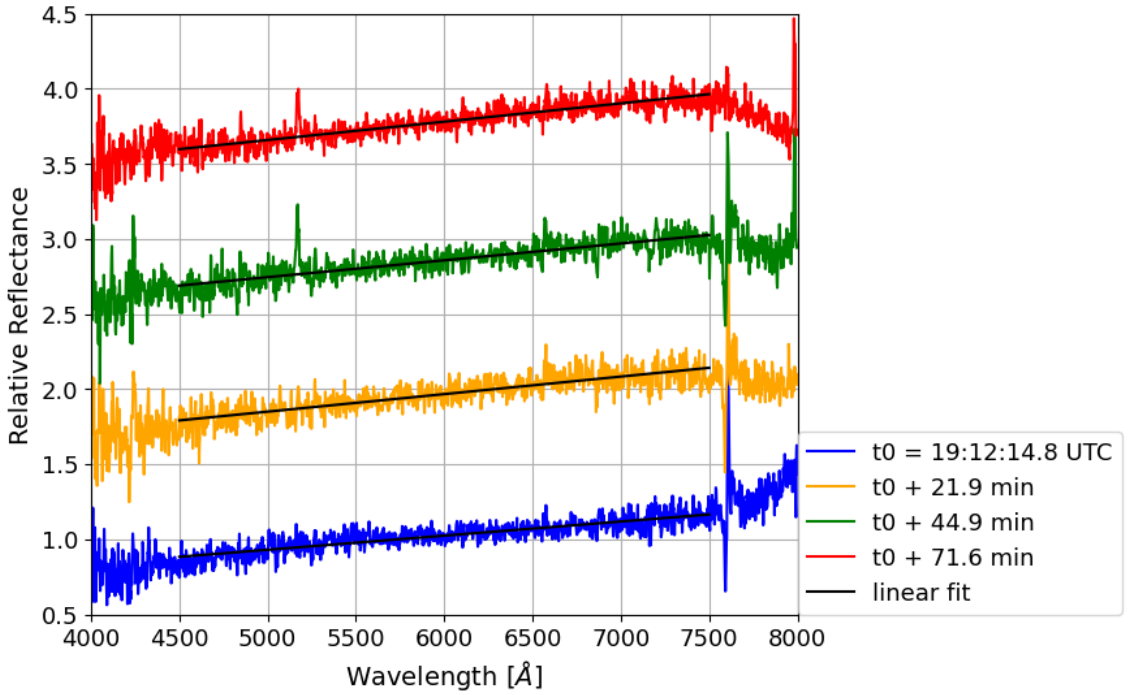

Figure 38: This is a plot of relative reflectance versus wavelength (in Å).The plot shows the median spectra of different sets of times starting from $t0 = 19:12:14.8$ UTC and ending at $t0 + 71.6$ minutes. Straight lines (thin black lines) were fitted to each of the median spectra within the range where there is enough throughput in the Mookodi detector (i.e., between 4500 Å and 7500 Å).

The value of the gradient of the first median spectrum (blue spectrum) is $9.40 \times 10^{-5} \pm 1.51 \times 10^{-6}$, the second median spectrum (orange spectrum) slope is $1.17 \times 10^{-4} \pm 1.92 \times 10^{-6}$, the third spectrum (green spectrum) slope is $1.12 \times 10^{-4} \pm 2 \times 10^{-6}$ and the fourth spectrum (red spectrum) slope is $1.22 \times 10^{-4} \pm 1.7 \times 10^{-6}$. Figure 39 presents a plot of the spectral slopes as a function of observation time. The mean spectral slope is 0.0111 ± 0.0016 %. Consequently, the Mookodi detector would be capable of detecting any spectral slope change greater than 14.44 % ($\frac{0.0016\%}{0.0111\%} \times 100$). A sinusoidal trigonometric function, based on the asteroid's rotation period of 4.34 ± 0.0021 hours, was fitted to the data. The variability of the fitted curve is 0.0052 %. Given that this variability is much smaller than the detection threshold of 14.44 %, it is concluded that the surface composition of 2005 EK70 is homogeneous over approximately a quarter of its surface, as the total observation time spans 1.19 hours.

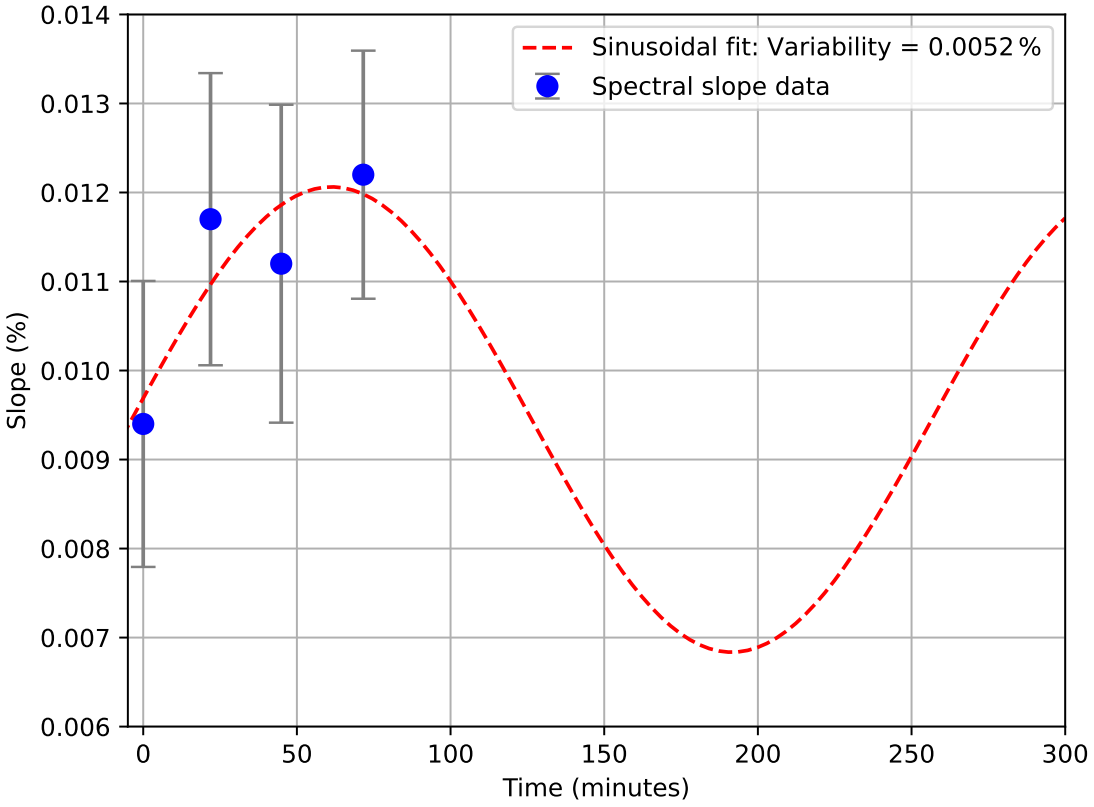

Figure 39: Plot of the percentage spectral slope versus observation time. The spectral slope data (blue dots) is fitted with a sinusoidal curve (red dashed line), corresponding to the asteroid's rotation period of 4.34 ± 0.0021 hours. The variability of the sinusoidal fit is 0.0052 %.

5.3.3 The size and characterisation of 2005 EK70

Since the mean brightness of 2005 EK70 is $H = 17.03 \pm 0.002$ magnitudes (as found in section 5.3.1), and it is known to be an Sv-type asteroid (the albedo range can be referenced from records of known Sv-type asteroids), the diameter of the asteroid can be determined. S-type asteroids are known to have an albedo, p_v, that ranges between 0.10 to 0.22 (Dymock [2010]). Using this range to get an average albedo, $\bar{p_v}$, results in $\bar{p_v} = 0.20 \pm 0.079$. Equation 7 (Harris and Harris [1997]) is used to calculate the diameter of the asteroid 2005 EK70. The calculated diameter of the asteroid 2005 EK70, with uncertainty, is 1.25 ± 0.26 km. The rotation period of the asteroid 2005 EK70 is 4.34 ± 0.0021 hours. This is a large, slow-rotating asteroid. The spin barrier of large asteroids is 2.2 hours. Large asteroids rotating faster than the spin barrier will break apart due to centrifugal forces, which overpower the

gravitational forces and cohesive strength that hold the asteroid together, causing its structure to become unstable and fragments to separate. Since the rotation period of the asteroid is longer than the spin barrier, it is unlikely for the asteroid to break apart, as the internal gravity holding the asteroid is greater than the centrifugal forces. The spin period and diameter of 2005 EK70 can be marked (in purple) on the frequency/rotation period versus diameter plot (Warner et al. [2009]) of known targets (including the spin barrier region), as shown in Figure 40. The Lomb-Scargle periodogram (see Figure 34) appears noisy, and the folded light curve (see Figure 35) lacks clarity, leading to low confidence in the derived rotation period. However, as shown in Figure 40, the asteroid's estimated rotation period falls within a region of the light curve database where many asteroids are located, suggesting that the rotation period is plausible.

$$d = 10^{[3.1236 - 0.5log_{10}(a) - 0.2H]} \tag{7}$$

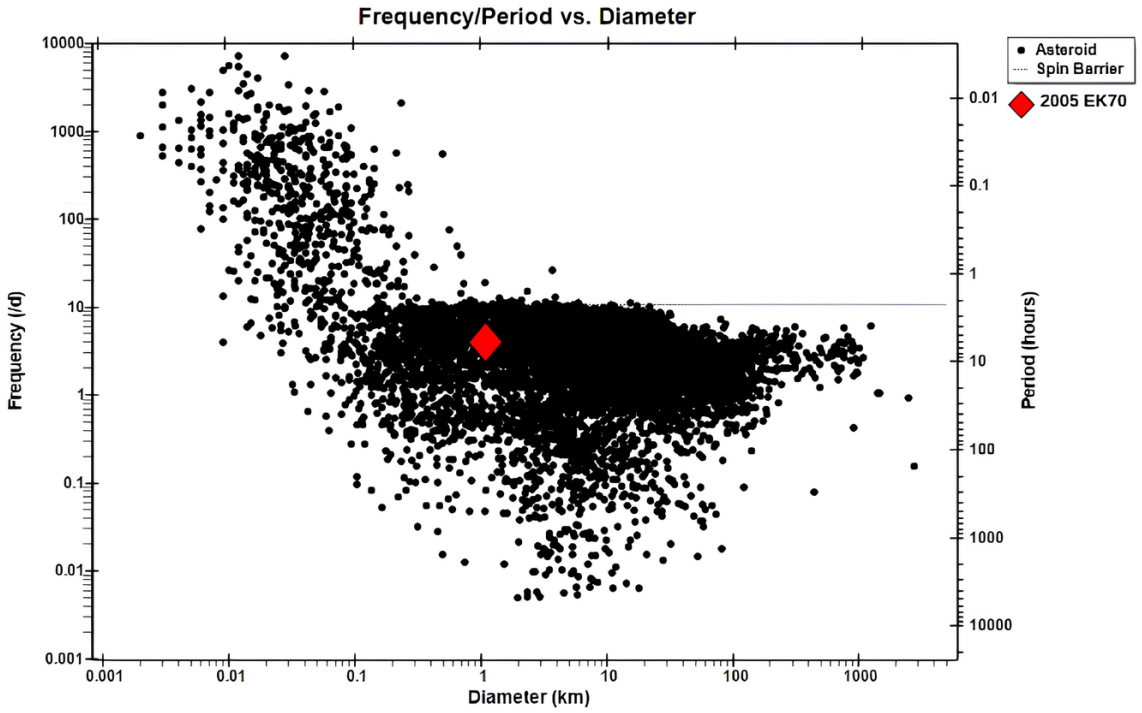

Figure 40: Spin period versus diameter of known asteroid targets. The point marked in purple is the target 2005 EK70 and this indicates that it is a large slow rotating asteroid. The horizontal dashed line indicates the spin barrier. The asteroid's estimated rotation period falls within a region of the light curve database where many asteroids are located, suggesting that the rotation period is plausible. Source: Warner et al. [2009].

5.4 Discussion and Conclusion of TEST CASE 2

The rotation period determined for 2005 EK70 is 4.34 ± 0.0021 hours, with the data collection spanning approximately 93.16 days. The time-resolved spectroscopy data covers 1.19 hours, which represents about a quarter of the asteroid's full rotation. Although the full rotation phase was not observed, no significant spectral changes were detected over this large portion of the rotation. Therefore, it can be concluded that 2005 EK70 likely has a homogeneous surface composition over at least a quarter of its surface.

The asteroid has been classified as an Sv-type, as its median spectrum closely matches the mean spectrum of the Sv-type taxonomy. With an estimated diameter of 1.25 ± 0.26 km, the asteroid is also slower than the spin barrier, meaning

it is stable and will not break apart due to centrifugal forces. Consequently, 2005 EK70 is identified as a slow-rotating, large Sv-type asteroid with a brightness of $H = 17.03 \pm 0.002$ magnitudes.

6 TEST CASE 3: Meteosat-11

Introduction

The third test object aims to simulate an observation on a bright asteroid-like object that has a high likelihood of showing changes in spectral signatures across its surface. The chosen object was Meteosat-11, a geostationary satellite. Geostationary satellites are positioned at an altitude of approximately 35,800 km directly above the equator. These satellites orbit in the same direction as the Earth's rotation, from west to east, with an orbital period of exactly 24 hours, corresponding to the time it takes the Earth to complete one full rotation about its axis. Geostationary satellites offer notable benefits across various applications due to their fixed orbital position above the equator (Zhao et al. [2022]). This unique placement enables continuous monitoring of specific geographic regions on Earth, which is essential for real-time data collection in weather forecasting (and natural disaster management), environmental assessment (i.e., environmental changes, land use and urban development), and telecommunications (e.g., television broadcasting, internet services and mobile communications).

Figure 41 illustrates a sketch of several geostationary satellites. Meteosat-11 was launched on 15 July 2015 and is positioned at a longitude of 9.5° East[13]. This location is approximately 10.9° East from the geographical longitude of the Lesedi Telescope. This longitudinal separation is sufficiently small to enable the Lesedi Telescope to observe the satellite effectively. Meteosat-11 is a 4th flight unit of the Meteosat Second Generation programme.

[13]Link to the satellite details by OSCAR: `https://space.oscar.wmo.int/satellites/view/meteosat_11`

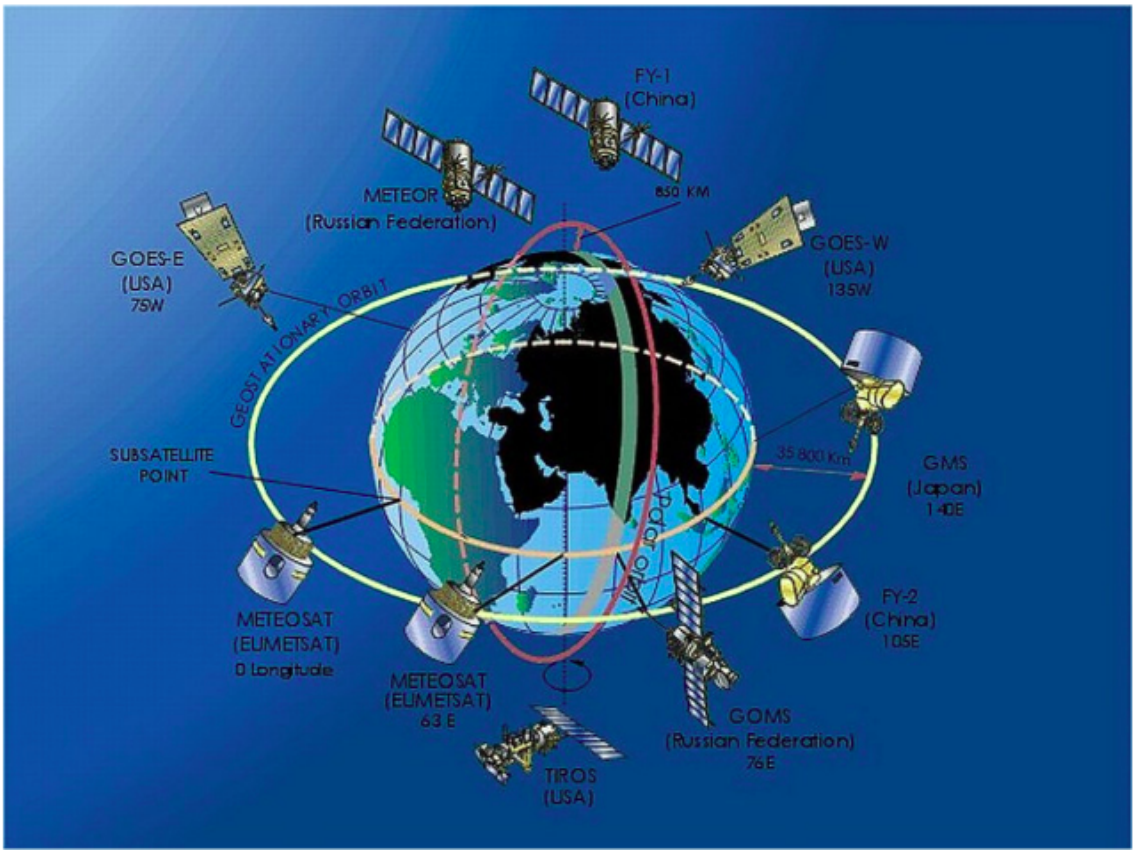

Figure 41: Figure showing a distribution of a few geostationary satellites. These geostationary satellites are positioned over specific locations on Earth, remaining fixed relative to certain regions or countries. This stationary orbit enables efficient communication services, satellite television broadcasting, and continuous weather monitoring for the areas they cover. Their coverage is useful for providing real-time data for meteorological services, disaster management, and secure telecommunications. Source: Liang and Wang [2019].

Initially, the objective was to test the Mookodi instrument on a tumbling satellite because a tumbling satellite would ensure that we observe different orientations. However, it was noted that a potential tumbling target, identified as Juno Centaur Stage, would only be visible in 2025. Therefore, the Mookodi instrument was instead tested on Meteosat-11, a stationary satellite with no tumbling motion. However, it is hoped that there may be some rotation (reorientation) present that could be detected through spectroscopic signature changes. Another relevant factor is the known composition of the target, specifically the external materials of Meteosat-11. Figure 42 presents the design of the Meteosat-11 satellite in its orbital configuration

around the Earth. The satellite features a cylindrical body with stacked components on top. The electronics onboard include a radiometer and solar panels. A smaller drum-shaped section at the top of the satellite houses antennas, while two additional cylinders are positioned above this drum to facilitate communication between the satellite and Earth. Additionally, the satellite is equipped with a high-technology camera known as the Meteosat Visible and InfraRed Imager (MVRI).

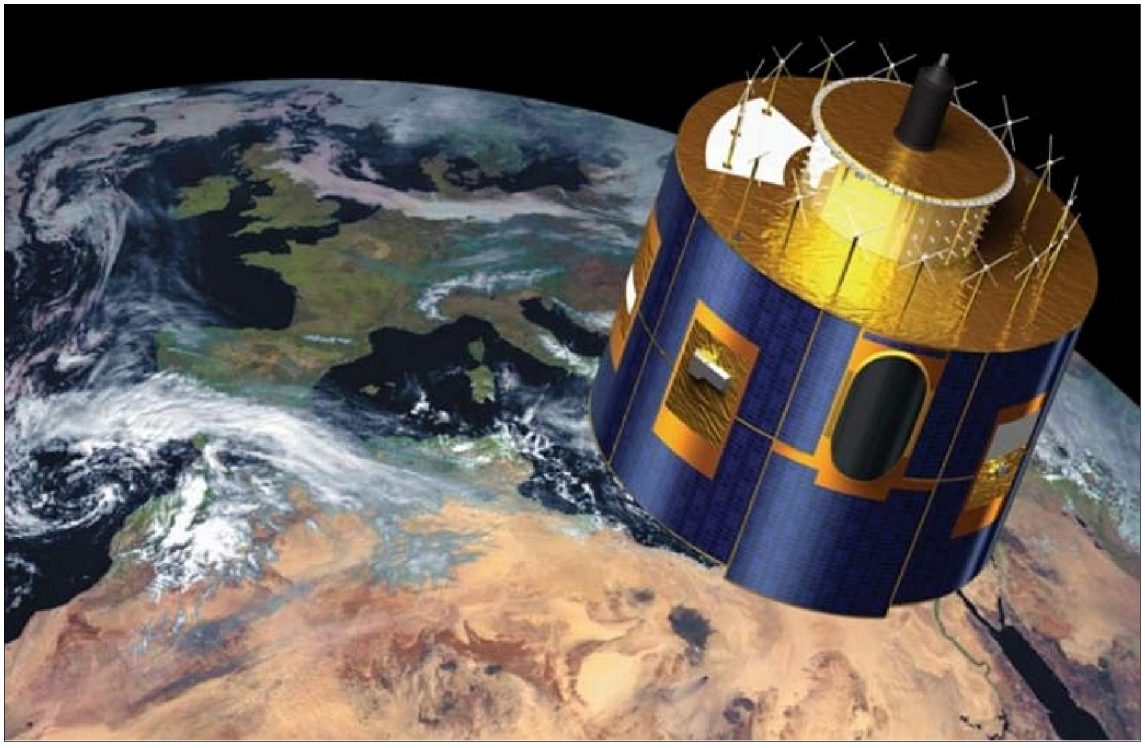

Figure 42: Figure showing the material components of Meteosat-11 satellite. Meteosat is mostly made of a big cylindrical body with some other parts stacked on top. There is a radiometer and solar panels present in the main body of Meteosat. There is a smaller drum-shaped part on top that has antennas for communicating with Earth. Inside the drum, there are electronics that control the antennas. There are also two other cylinders on top of the drum that are used for communication. Meteosat-11 consists of a advanced imaging camera that takes images of the Earth's weather called the Meteosat Visible and InfraRed Imager (MVRI). Source: Osgood [2017]

6.1 Observing Strategy

On 25th February, g-band photometric data were collected with a few of 30-second exposures but mostly 1-second exposures. There are a total of 17 raw g-band photometric images and 47 60-second exposure spectroscopy science images. After the

collection of data, 6 poor quality spectroscopic science images were discarded. The total time length of the continuous observations was 1 hour and 43 minutes. The airmass and the parallactic angle were fixed at 1.3 and 197° respectively during the observations because this is a geostationary satellite and therefore the telescope effectively points at the same altitude and azimuth for the entire observation.

The observing strategy for the Meteosat-11 test mirrors that of the 2005 EK70 test case. Initially, a future time, typically 10 minutes ahead, is selected to facilitate the manual pointing of the telescope and target identification. The Right Ascension (RA) and Declination (Dec) coordinates are then obtained, and the telescope is pointed accordingly. The parallactic angle is calculated and adjusted, and the camera is set to semi video-mode for tracking the moving target. Once identified, the telescope is switched to non-sidereal tracking, and fine adjustments are made to keep the target aligned with the spectrograph slit. The instrument is then placed in spectrograph mode for repeated exposures, which are monitored for maximum counts. Once counts drop, the instrument returns to imaging mode for realignment before repeating the spectroscopic process. For a detailed description of this procedure, please refer to Section 5.1.

Figure 43 presents two images with a 30-second exposure time from this observing strategy of Meteosat-11. The diagonal streaks indicate the paths of the background stars, while the stationary point at the center of the field of view represents the satellite.

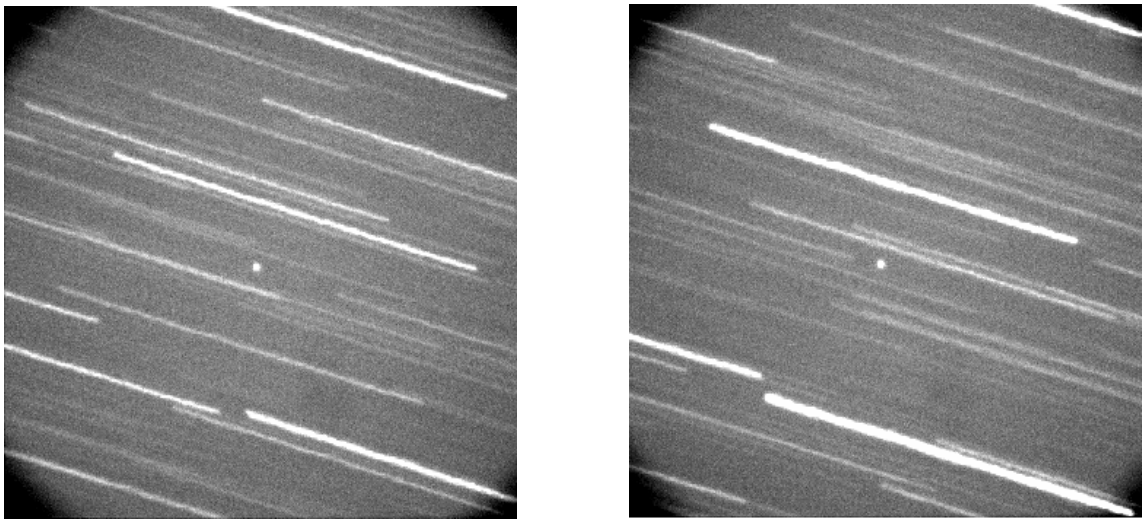

Figure 43: Two of the images obtained from the process of non-sidereal tracking on a fast moving geosynchronous satellite with high sidereal rates and an exposure time of 30 seconds. The diagonal lines represent the paths that the background stars are following while the dot at the center is Meteosat-11 satellite which is appearing to be stationary relative to the background stars.

During the observation period, both the airmass and parallactic angle remained the same, a key factor that helps rule out any changes in the spectra caused by airmass variations. Tracking a geosynchronous object essentially means that the telescope remains fixed, pointing at a stationary point in the sky i.e. the altitude and azimuth of the telescope do not change. This contrasts with the observations of other targets, such as Pluto and 2005 EK70, where these conditions were not constant. The full summary of the observations performed on Meteosat-11 can be found in Appendix C. To estimate the apparent magnitude of the satellite, a comparison method was used with nearby stars in the field of view. The Right Ascension (RA) and Declination (Dec) coordinates from the FITS file header were used to identify stars present in the photometry image. Using astrometric analysis [14], several stars were identified, including Tycho 160-974-1, which has coordinates RA = 103.02° and Dec = 6.14°. The flux of Tycho 160-974-1 was determined to be similar to that of the satellite, indicating a comparable brightness. From the GAIA catalog, the G-magnitude of Tycho 160-974-1 is 11.34 ± 0.003 (Gaia Collaboration [2020]). Based on this similarity in flux, the satellite's apparent magnitude is estimated to be approximately 11.34. Due to the streaking of stars in the image, an exact measurement of the satellite's

[14] Astrometry page used to perform astrometry: `Astrometry.net`

apparent magnitude using the photometric pipeline (PP) was not feasible. However, this comparison method provides a reasonable estimate of the satellite's magnitude based on the similar flux of Tycho 160-974-1.

6.2 Results

The ASPIRED software was used to process the raw spectroscopy FITS files and generate counts spectra. For each counts spectrum, the corresponding observation time was recorded. Figure 44 shows six of the counts spectra of Meteosat-11 with different observation times. Since the airmass and the parallactic angle are constant, it is clear from the plot that there are no noticeable changes in the spectral slope between wavelengths 4500 Å and 7500 Å. Areas outside below 4500 Å and above 7500 Å are not considered due to the limited throughput in these areas, based on the design of the spectrograph.

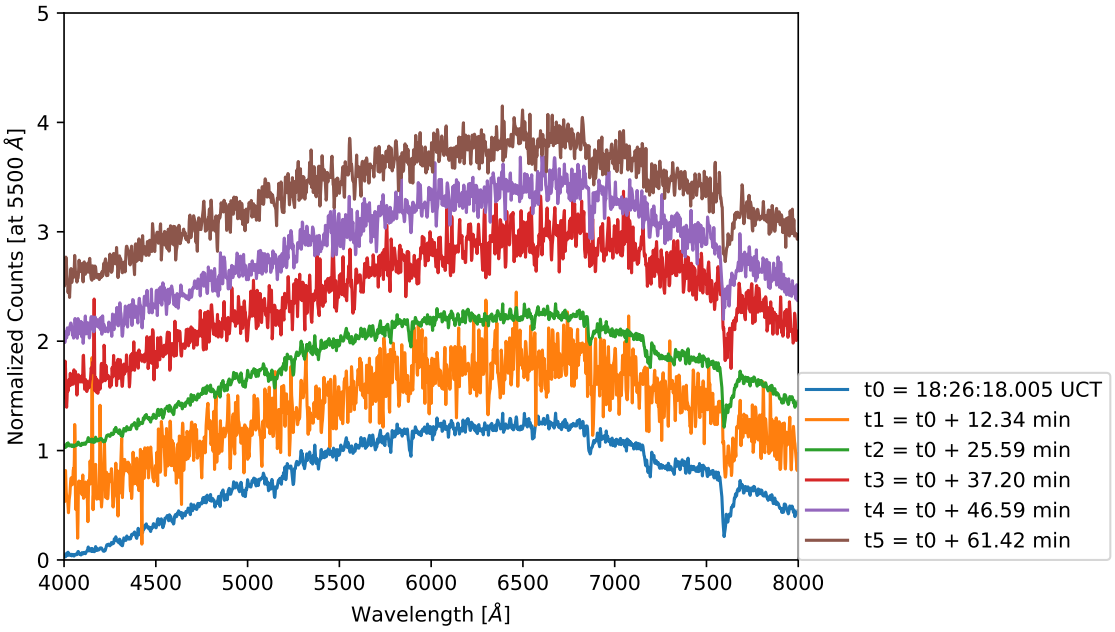

Figure 44: This is a plot of normalised counts versus wavelength (in Å). Few of the spectra are plotted (having different observation times) and offset 0.5 units apart for clarity. The first spectrum was taken at $t0 = 18:26:18.005$ UTC, the second spectrum was taken 12.34 minutes ahead relative to t0, the third spectrum was taken 25.59 minutes ahead of t0, the fourth spectrum was taken 37.20 minutes ahead of t0, the fifth spectrum was taken 46.59 minutes ahead of t0 and the sixth spectrum was taken 61.42 minutes ahead of t0. All spectra were normalised at 550 nm.

A 2D colour map was plotted to represent all collected counts spectra (Figure 46), showing observation time versus wavelength, with the colour intensity indicating the counts. Prior to plotting, the counts were normalised at 550 nm and a Gaussian fit was applied to determine the best-fit wavelength peak for each spectrum. Figure 45 shows a demonstration of one of the normalised spectra (in blue) fitted with a Gaussian model (red curve).

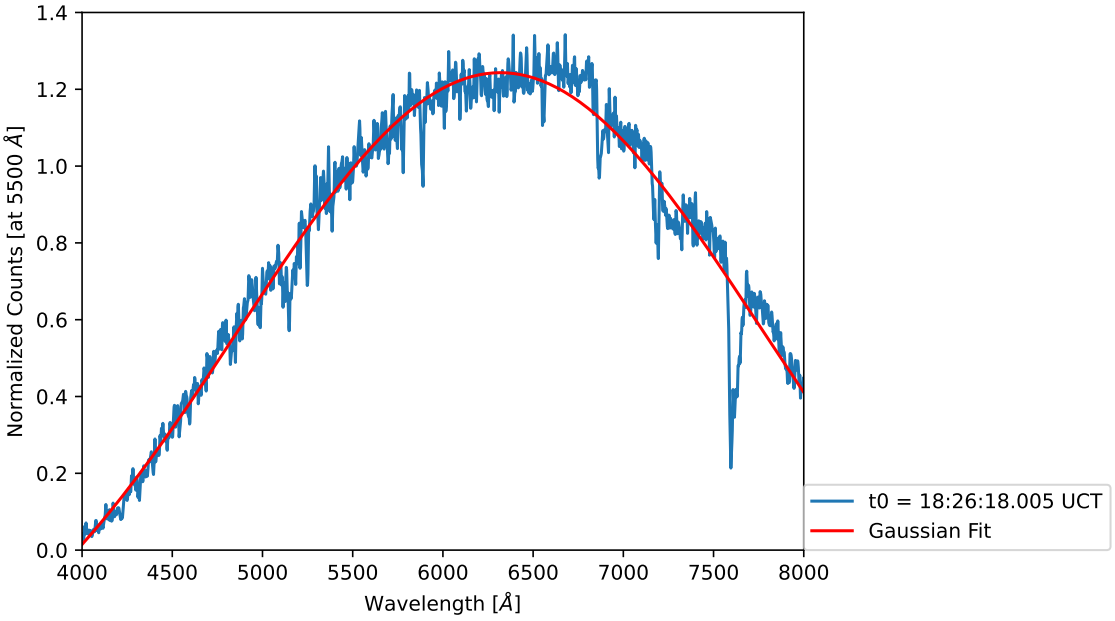

Figure 45: Demonstration plot of a Gaussian fit process on a normalised counts spectrum (in blue) with an observation time of $t0 = 18 : 26 : 18.005$ UTC. The Gaussian curve (in red) makes a plausible fit.

These peak wavelengths are denoted by thick vertical blue lines on Figure 46 in order to determine if there was any shift in the peak of the spectrum as a function of time. Horizontal dark blue regions indicate time gaps between consecutive spectra where no data was collected (i.e when realignment onto the slit was performed).

The Gaussian peak wavelengths displayed random shifts, moving left and right. Initially, it was hypothesised that these shifts could be attributed to the high right ascension and declination rates of Meteosat-11, potentially causing the target to drift off the slit during non-sidereal tracking. However, upon further examination, this explanation was dismissed, as target drift should primarily affect the intensity rather than the wavelength position. A deeper investigation into this phenomenon is explored in the following section.

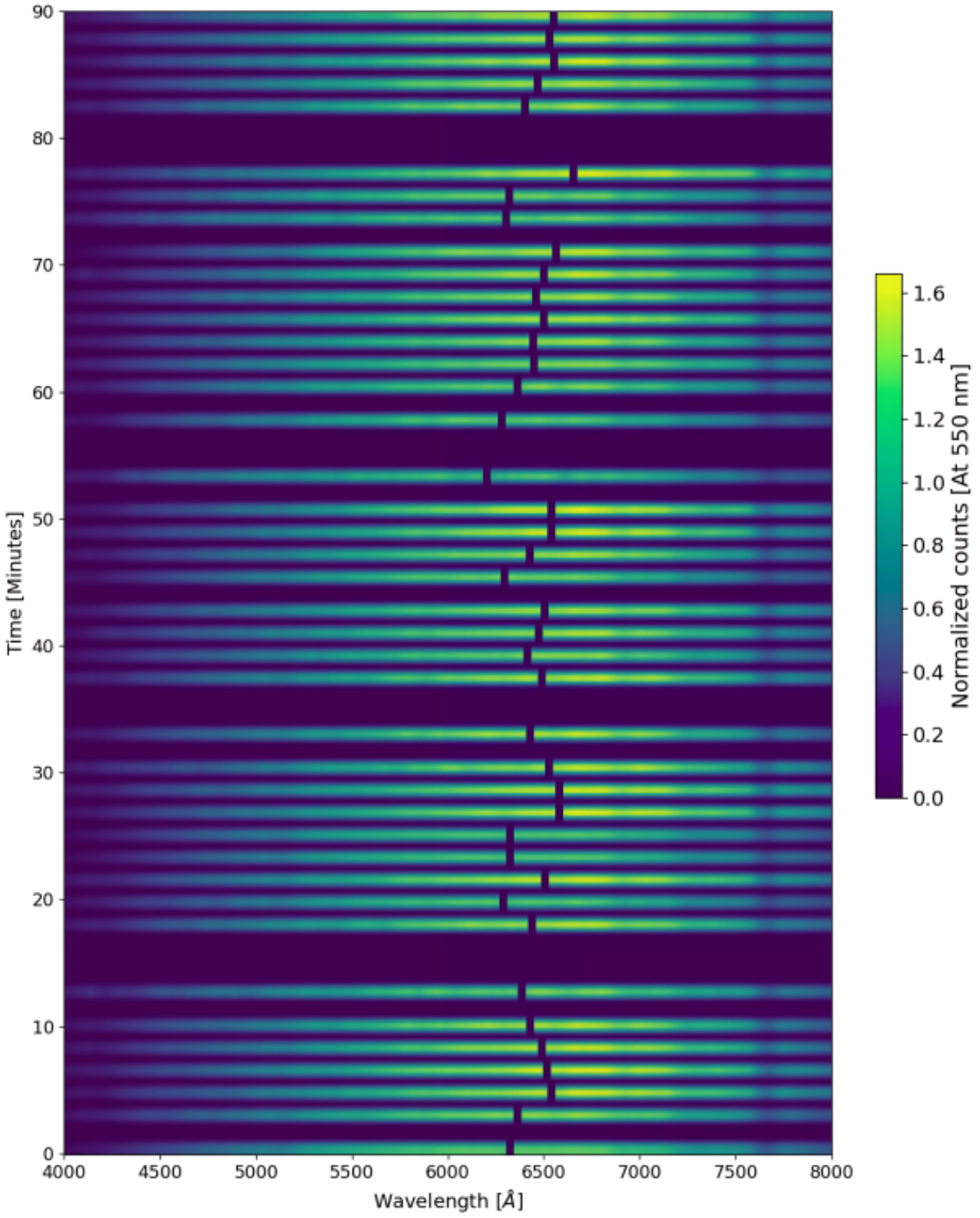

Figure 46: The spectral map displays the normalised counts as a function of wavelength and observation time. The vertical axis represents the observing time, while the horizontal axis corresponds to the wavelength. The colour scale illustrates the intensity of the normalised counts, which have been normalised at 5500 Å. Dark blue horizontal bands between the spectra indicate time gaps between consecutive observations where no data was collected. The thick vertical dark blue features observed between 6000 Å and 7000 Å in each normalised spectrum highlight the location of the best-fit Gaussian peaks. The colour bar on the side provides a reference for the intensity values of the normalised counts across the spectrum.

6.3 Studying the variation of the peak counts

From the 2D colourmap (Figure 46), the central positions of the Gaussian-fitted wavelength peaks were extracted and plotted as a function of observation time (Figure 47). This dataset was subsequently analysed using the Lomb-Scargle periodogram (Lomb [1976] and Scargle [1982]), which revealed three potential period peaks (A, B, and C), as displayed in Figure 48. The periods are constrained by the exposure time of 60 seconds (limiting resolution of periods shorter than this) and the total observation window of 90 minutes (limiting periods longer than this).

Gaussian curves were fitted to each of the identified periodogram peaks, resulting in the period values $Peak\ A = 7.24 \pm 0.0012$ minutes (Figure 49), $Peak\ B = 10.28 \pm 0.0019$ minutes (Figure 50) and $Peak\ C = 19.81 \pm 0.0010$ minutes. No specific records were found corresponding to these periods, but it is known that weather satellites, such as Meteosat-11, make periodic adjustments to maintain their orbits and orientations. It remains uncertain whether such adjustments occurred during the observation window.

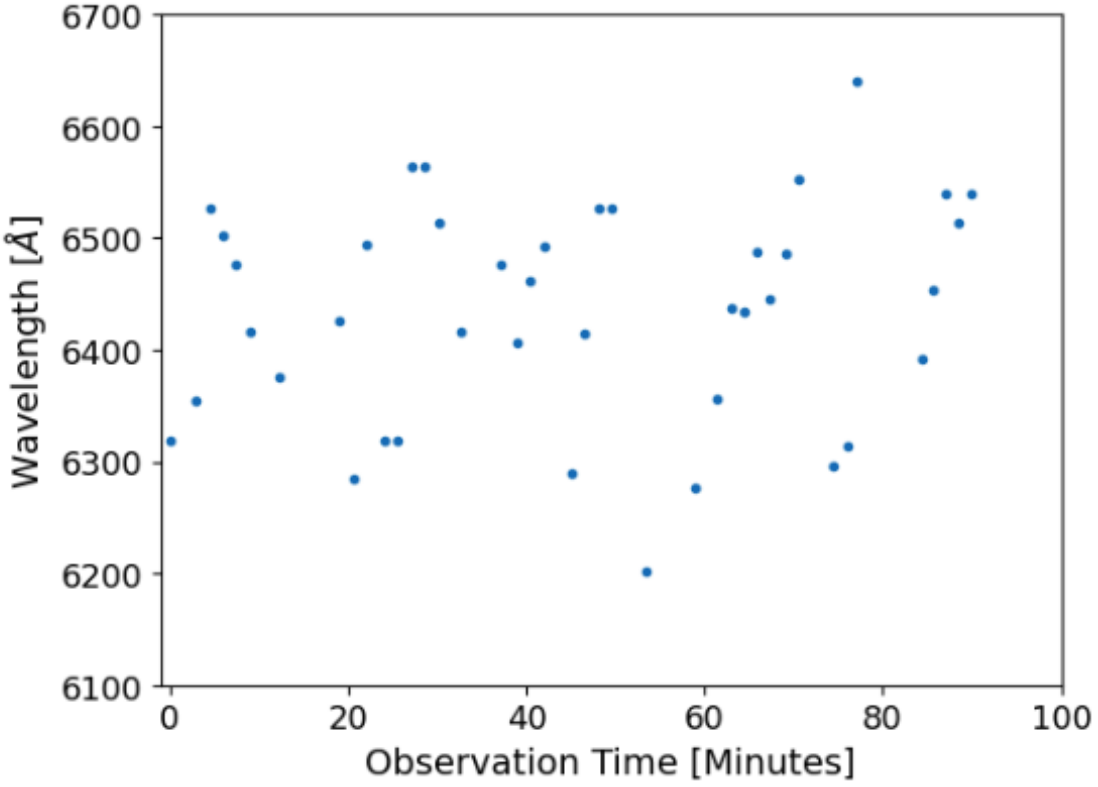

Figure 47: Plot showing the wavelength peak positions (in Å) versus the observation time (in minutes).

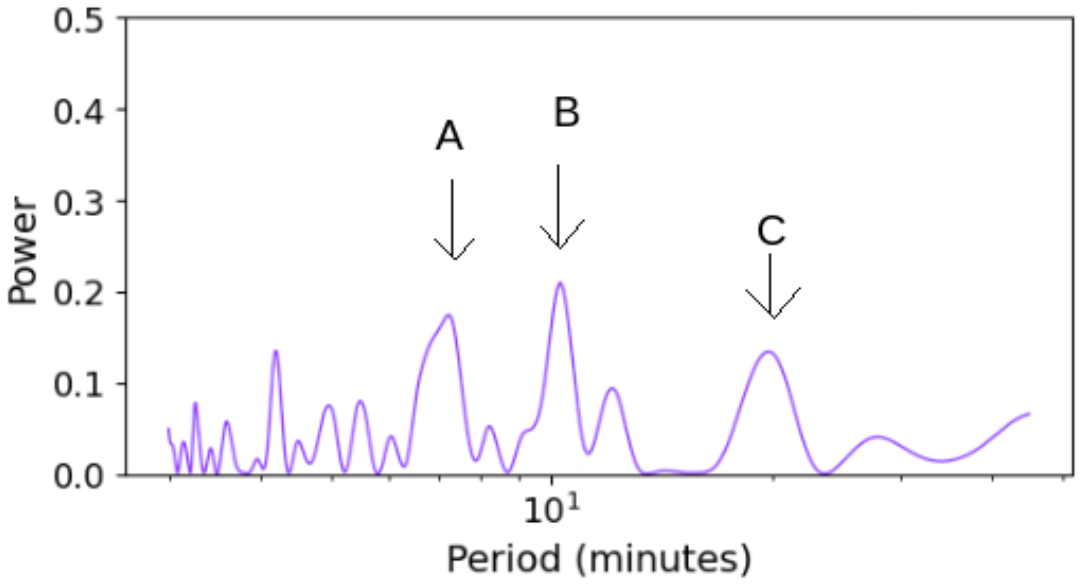

Figure 48: Power spectrum of the Wavelength versus observation time plot. The marked peaks A, B and C are the possible peaks to explain the variation of peak wavelengths. The Power of the peaks is less than 0.3 and the highest peak is peak B.

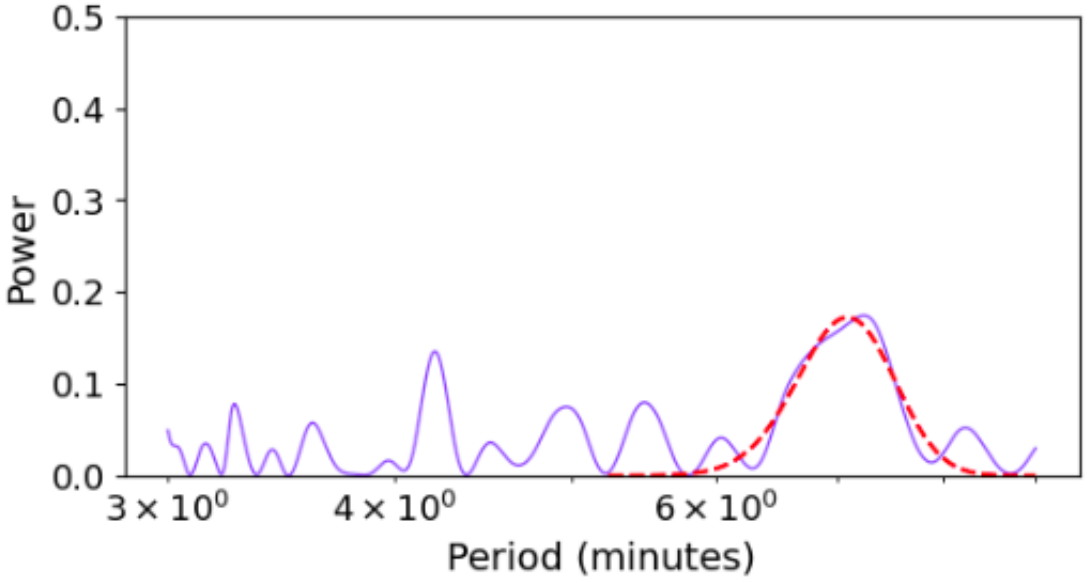

Figure 49: The power spectrum is derived from the plot of wavelength versus observation time. A Gaussian curve has been fitted to Peak A, resulting in a calculated period of 7.24 ± 0.0012 minutes.

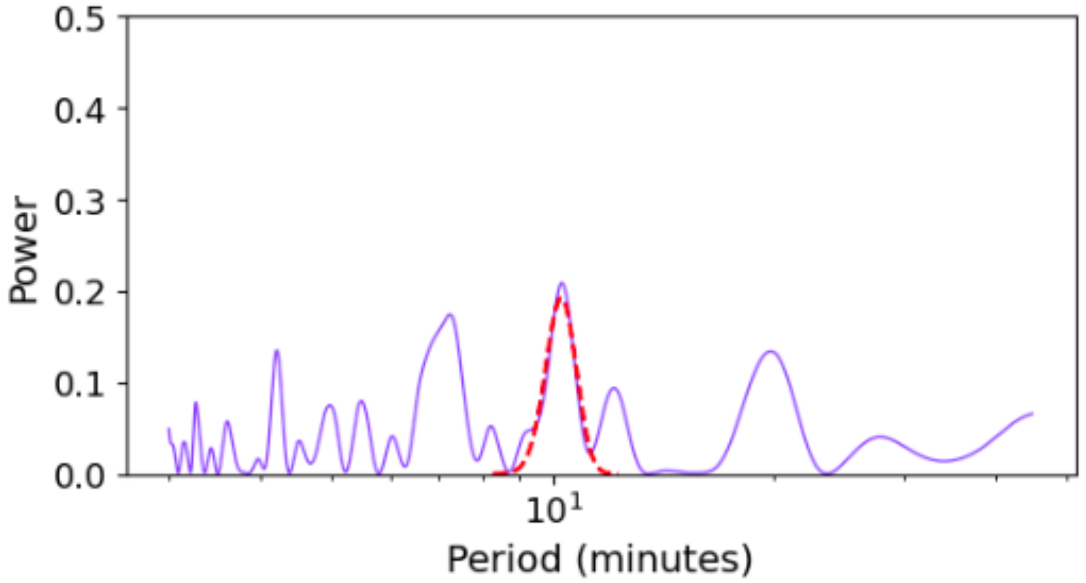

Figure 50: The power spectrum is based on the wavelength versus observation time plot. A Gaussian curve has been fitted to Peak B, yielding a period of 10.28 ± 0.0019 minutes.

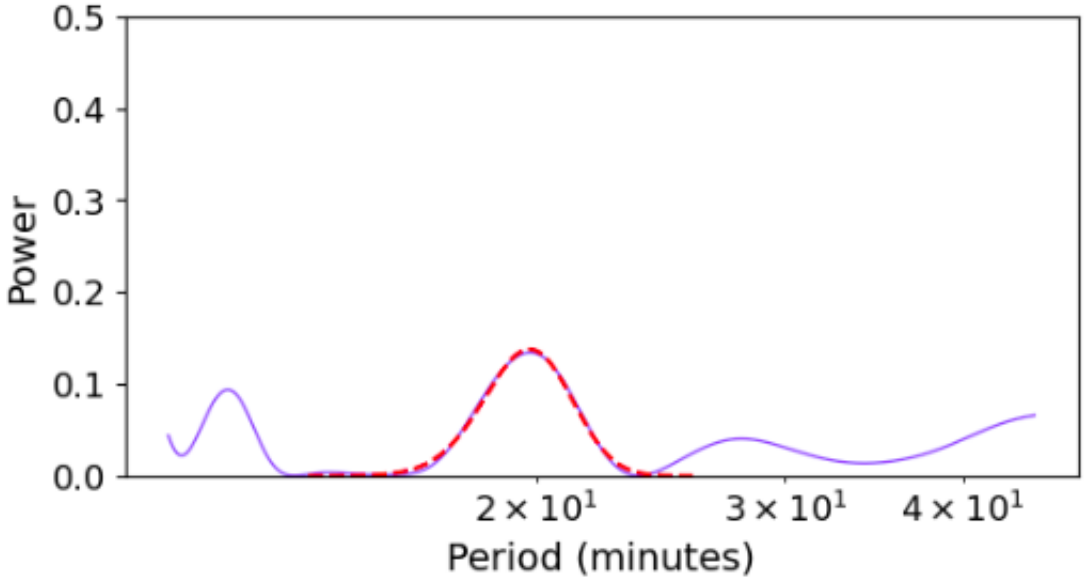

Figure 51: The power spectrum is generated from the wavelength versus observation time plot. A Gaussian curve has been fitted to Peak C, resulting in a period of 19.81 ± 0.0010 minutes.

6.4 Discussion and Conclusion of Test CASE 3

The counts spectra of Meteosat-11 were plotted to investigate potential changes in the spectral shape. The normalised counts spectra in Figure 44 and the 2D spectral map in Figure 46 show no significant alterations in spectral shape, indicating that the Mookodi instrument is capable of detecting the lack of surface changes on a geosynchronous satellite like Meteosat-11. However, variations were observed in the peak wavelength positions, from which three periodogram periods of peak wavelength variations were derived.

7 Conclusion and Future Work

The analysis of Pluto in Chapter 4 showed methane ice band-depth variations versus rotation phase. The results from Pluto's spectra, obtained using time-resolved spectroscopy and photometry, aligned with previous observations by Lorenzi et al. [2016], confirming that Mookodi can detect surface composition inhomogeneity on a target with the same brightness as large main-belt asteroids and that also moves slowly in both rotation and orbital motion.

The analysis of 2005 EK70 in Chapter 5 demonstrated that the average reflectance spectrum aligns with the existing taxonomic classification reported by Binzel et al. [2019]. However, as the spectra were collected over only a quarter of the asteroid's rotation phase, this is insufficient to validate whether Mookodi can detect surface composition inhomogeneity for a near-Earth asteroid with faster on-sky motion. The observations suggest a relatively uniform surface composition over the quarter phase observed, but further data is needed to cover the complete rotation period of 4.34 ± 0.0021 hours.

The test involving Meteosat-11 showed the expected absence of changes in the spectral slope, however, horizontal shifts of the counts spectrum peaks were measured and it is unclear whether there was any adjustments done on the satellite during observations.

To extend this research, an additional TEST CASE would be to observe a target that is not in geosynchronous orbit and exhibits tumbling motion. For future observations, the Juno Centaur Stage presents a suitable target on 27 January 2025, the date when it will be visible. This date has been confirmed using the JPL Horizons database. An animation depicting the Juno spacecraft separating from the Centaur upper stage, which was used to propel the spacecraft toward Jupiter, is shown in Figure 52. For future observers, who would investigate on this target or any other

asteroid-like target, it is critical for adjustments to be made on the parallactic angle for telescope derotators because the parallactic angle is important in spectral slopes. If possibly measured, the rotation period of a future target can give an idea of how much spectroscopic coverage can be done so that changes in the spectra can be monitored over a full rotation phase of the target. In order to ensure that the measured rotation period is plausible, the light curve databases can be found useful to compare to because light curve databases have many recorded targets to date based on their physical astronomical parameters. Examining spectral shape or linespacing can be more challenging, and parallactic angles and airmass factors are essential considerations. However, focusing on peak wavelengths of a broad spectrum might allow for the detection of surface inhomogeneity.

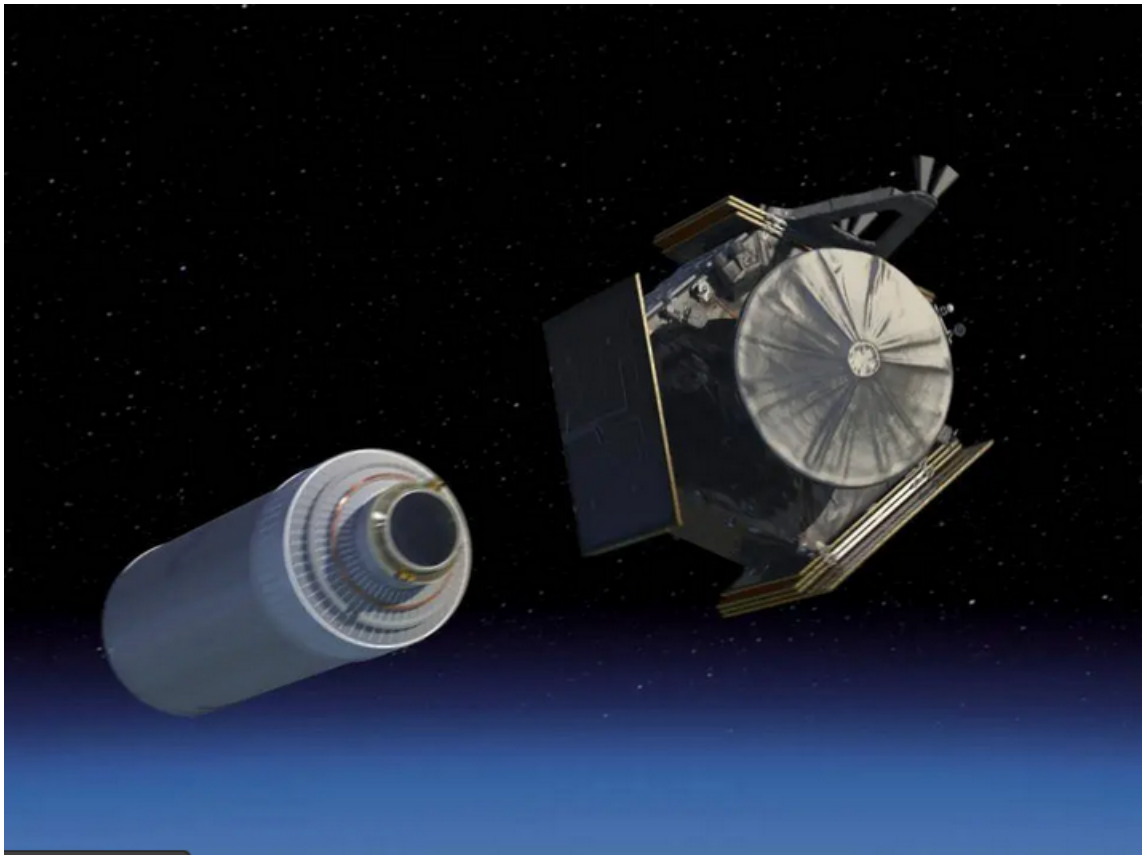

Figure 52: Artist's rendering of the Juno spacecraft separating from the Centaur upper stage. After completing its boost phase, the Centaur stage is jettisoned, allowing Juno to begin its interplanetary voyage to Jupiter. The cylindrical object on the left represents the Centaur stage, while the spacecraft on the right is Juno, showcasing its main engine, high-gain antenna, and magnetometer boom, which will be deployed later in the mission. The Centaur stage is jettisoned uncontrollably, causing the object to tumble indefinitely through space. Source: NASA/JPL-Caltech

References

V. Lorenzi, N. Pinilla-Alonso, J. Licandro, D. P. Cruikshank, W. M. Grundy, R. P. Binzel, and J. P. Emery. The spectrum of Pluto, 0.40-0.93 μm. I. Secular and longitudinal distribution of ices and complex organics. A&A, 585:A131, January 2016. doi: 10.1051/0004-6361/201527281.

B. Carry, C. Dumas, M. Fulchignoni, W. J. Merline, J. Berthier, D. Hestroffer, T. Fusco, and P. Tamblyn. Near-infrared mapping and physical properties of the dwarf-planet Ceres. A&A, 478(1):235–244, January 2008. doi: 10.1051/0004-6361:20078166.

Thomas B. McCord and Francesca Zambon. The surface composition of Ceres from the Dawn mission. icarus, 318:2–13, January 2019. doi: 10.1016/j.icarus.2018.03.004.

O. Ruesch, T. Platz, P. Schenk, L. A. McFadden, J. C. Castillo-Rogez, L. C. Quick, S. Byrne, F. Preusker, D. P. O'Brien, N. Schmedemann, D. A. Williams, J. Y. Li, M. T. Bland, H. Hiesinger, T. Kneissl, A. Neesemann, M. Schaefer, J. H. Pasckert, B. E. Schmidt, D. L. Buczkowski, M. V. Sykes, A. Nathues, T. Roatsch, M. Hoffmann, C. A. Raymond, and C. T. Russell. Cryovolcanism on Ceres. *Science*, 353(6303):aaf4286, September 2016. doi: 10.1126/science.aaf4286.

Michael K. Shepard, Katherine de Kleer, Saverio Cambioni, Patrick A. Taylor, Anne K. Virkki, Edgard G. Rívera-Valentin, Carolina Rodriguez Sanchez-Vahamonde, Luisa Fernanda Zambrano-Marin, Christopher Magri, David Dunham, John Moore, and Maria Camarca. Asteroid 16 Psyche: Shape, Features, and Global Map. psj, 2(4):125, August 2021. doi: 10.3847/PSJ/abfdba.

Brandon C. Johnson, Michael M. Sori, and Alexander J. Evans. Ferrovolcanism on metal worlds and the origin of pallasites. *Nature Astronomy*, 4:41–44, January 2020. doi: 10.1038/s41550-019-0885-x.

Konstantin Batygin and Michael E. Brown. Early Dynamical Evolution of the Solar System: Pinning Down the Initial Conditions of the Nice Model. ApJ, 716(2):1323–1331, June 2010. doi: 10.1088/0004-637X/716/2/1323.

P. Griveaud, A. Crida, A. C. Petit, E. Lega, and A. Morbidelli. The Solar System could have formed in a low-viscosity disc: A dynamical study from giant planet migration to the Nice model. A&A, 688:A202, August 2024. doi: 10.1051/0004-6361/202450340.

Andreas M. Hein, Michael Saidani, and Hortense Tollu. Exploring Potential Environmental Benefits of Asteroid Mining. *arXiv e-prints*, art. arXiv:1810.04749, October 2018. doi: 10.48550/arXiv.1810.04749.

Pablo Calla, Dan Fries, and Chris Welch. Asteroid mining with small spacecraft and its economic feasibility. *arXiv e-prints*, art. arXiv:1808.05099, August 2018. doi: 10.48550/arXiv.1808.05099.

Juan A. Sanchez, Vishnu Reddy, Michael K. Shepard, Cristina Thomas, Edward A. Cloutis, Driss Takir, Albert Conrad, Cain Kiddell, and Daniel Applin. Detection of Rotational Spectral Variation on the M-type Asteroid (16) Psyche. AJ, 153(1): 29, January 2017. doi: 10.3847/1538-3881/153/1/29.

Nicolas Erasmus, Iain A. Steele, Andrzej S. Piascik, Stuart D. Bates, Christopher J. Mottram, Kathryn A. Rosie, Carel H. D. R. van Gend, Ulrich Geen, Magaretha L. L. Pretorius, Stephen B. Potter, Egan Loubser, Willie Koorts, Hitesh Gajjar, Keegan Titus, Hannah L. Worters, Amanda A. Sickafoose, Sunil Chandra, James E. E. O'Connor, Kgothatso Matlala, Justine Crook-Mansour, Ali Ranjbar, Robert J. Smith, Helen E. Jermak, Shalom Abiodun, and Okwudili D. Egbo. Mookodi: multi-purpose low-resolution spectrograph and multi-filter photometric imager for rapid follow-up observations of astronomical transient events. *Journal of Astronomical Telescopes, Instruments, and Systems*, 10(2):025005, 2024. doi: 10.1117/1.JATIS.10.2.025005. URL `https://doi.org/10.1117/1.JATIS.10.2.025005`.

Hannah L. Worters, James E. O'Connor, David B. Carter, Egan Loubser, Pieter A. Fourie, Amanda Sickafoose, and Pieter Swanevelder. SAAO's new robotic telescope and WiNCam (Wide-field Nasmyth Camera). 9908:99083Y, August 2016. doi: 10.1117/12.2231636.

Marco C. Lam, Robert J. Smith, Iair Arcavi, Iain A. Steele, Josh Veitch-Michaelis, and Lukasz Wyrzykowski. Automated SpectroPhotometric Image REDuction (ASPIRED). AJ, 166(1):13, July 2023. doi: 10.3847/1538-3881/acd75c.

J. Xavier Prochaska, Joseph Hennawi, Ryan Cooke, Kyle Westfall, Feige Wang, EmAstro, Tiffanyhsyu, Asher Wasserman, Alexa Villaume, Marijana777, JT Schindler, David Young, Sunil Simha, Matt Wilde, Nicolas Tejos, Jacob Isbell, Andreas Flörs, Nathan Sandford, Zlatan Vasović, Edward Betts, and Brad Holden. pypeit/PypeIt: Release 1.0.0. art. 10.5281/zenodo.3743493, April 2020a. doi: 10.5281/zenodo.3743493.

J. Prochaska, Joseph Hennawi, Kyle Westfall, Ryan Cooke, Feige Wang, Tiffany Hsyu, Frederick Davies, Emanuele Farina, and Debora Pelliccia. PypeIt: The Python Spectroscopic Data Reduction Pipeline. *The Journal of Open Source Software*, 5(56):2308, December 2020b. doi: 10.21105/joss.02308.

M. Mommert. PHOTOMETRYPIPELINE: An automated pipeline for calibrated

photometry. *Astronomy and Computing*, 18:47–53, January 2017. doi: 10.1016/j.ascom.2016.11.002.

E. Bertin and S. Arnouts. SExtractor: Software for source extraction. A&AS, 117: 393–404, June 1996. doi: 10.1051/aas:1996164.

E. Bertin. Automatic Astrometric and Photometric Calibration with SCAMP. In C. Gabriel, C. Arviset, D. Ponz, and S. Enrique, editors, *Astronomical Data Analysis Software and Systems XV*, volume 351 of *Astronomical Society of the Pacific Conference Series*, page 112, July 2006.

F. Ochsenbein, P. Bauer, and J. Marcout. The VizieR database of astronomical catalogues. A&AS, 143:23–32, April 2000. doi: 10.1051/aas:2000169.

Catherine B. Olkin, John R. Spencer, William M. Grundy, Alex H. Parker, Ross A. Beyer, Paul M. Schenk, Carly J. A. Howett, S. Alan Stern, Dennis C. Reuter, Harold A. Weaver, Leslie A. Young, Kimberly Ennico, Richard P. Binzel, Marc W. Buie, Jason C. Cook, Dale P. Cruikshank, Cristina M. Dalle Ore, Alissa M. Earle, Donald E. Jennings, Kelsi N. Singer, Ivan E. Linscott, Allen W. Lunsford, Silvia Protopapa, Bernard Schmitt, Eddie Weigle, and the New Horizons Science Team. The Global Color of Pluto from New Horizons. AJ, 154(6):258, December 2017. doi: 10.3847/1538-3881/aa965b.

T. Bertrand, F. Forget, O. White, B. Schmitt, S. A. Stern, H. A. Weaver, L. A. Young, K. Ennico, and C. B. Olkin. Pluto's Beating Heart Regulates the Atmospheric Circulation: Results From High-Resolution and Multiyear Numerical Climate Simulations. *Journal of Geophysical Research (Planets)*, 125(2):e06120, February 2020. doi: 10.1029/2019JE006120.

J. L. Tonry, L. Denneau, A. N. Heinze, B. Stalder, K. W. Smith, S. J. Smartt, C. W. Stubbs, H. J. Weiland, and A. Rest. Atlas: A high-cadence all-sky survey system. *Publications of the Astronomical Society of the Pacific*, 130(988):064505, May 2018. ISSN 1538-3873. doi: 10.1088/1538-3873/aabadf. URL `http://dx.doi.org/10.1088/1538-3873/aabadf`.

David J. Tholen and Edward F. Tedesco. Pluto's Lightcurve: Results from Four Oppositions. icarus, 108(2):200–208, April 1994. doi: 10.1006/icar.1994.1054.

L. Shingles, K. W. Smith, D. R. Young, S. J. Smartt, J. Tonry, L. Denneau, A. Heinze, H. Weiland, H. Flewelling, B. Stalder, A. Clocchiatti, F. Förster, G. Pignata, A. Rest, J. Anderson, C. Stubbs, and N. Erasmus. Release of the ATLAS Forced Photometry server for public use. *Transient Name Server AstroNote*, 7:1–7, January 2021.

Chris Benn, Kevin Dee, and Tibor Agócs. ACAM: a new imager/spectrograph for the William Herschel Telescope. 7014:70146X, 2008. doi: 10.1117/12.788694. URL https://doi.org/10.1117/12.788694.

A. Boksenberg. The William Herschel telescope. *Vistas in Astronomy*, 28(2):531–553, January 1985. doi: 10.1016/0083-6656(85)90074-1.

W. M. Grundy, C. B. Olkin, L. A. Young, M. W. Buie, and E. F. Young. Near-infrared spectral monitoring of Pluto's ices: Spatial distribution and secular evolution. icarus, 223(2):710–721, April 2013. doi: 10.1016/j.icarus.2013.01.019.

TM Brown, N Baliber, FB Bianco, M Bowman, B Burleson, P Conway, M Crellin, É Depagne, J De Vera, B Dilday, et al. Las cumbres observatory global telescope network. *Publications of the Astronomical Society of the Pacific*, 125(931):1031, 2013.

Richard J. Mathar. Astronomical air mass. *arXiv preprint arXiv:1206.1692*, 2015. URL https://www2.mpia-hd.mpg.de/~mathar/public/mathar20151213.pdf. Dated: December 17, 2015.

Francesca E. DeMeo, Richard P. Binzel, Stephen M. Slivan, and Schelte J. Bus. An extension of the Bus asteroid taxonomy into the near-infrared. icarus, 202(1): 160–180, July 2009. doi: 10.1016/j.icarus.2009.02.005.

Thomas H Burbine, Iman Khanani, Deepika Kumawat, Ahlay Hussain, Sydney M Wallace, and M Darby Dyar. Testing the bus–demeo asteroid taxonomy using meteorite spectra. *The Planetary Science Journal*, 5(9):194, 2024.

Roger Dymock. The h and g magnitude system for asteroids. *Journal of the British Astronomical Association, vol. 117, no. 6, p. 342-343*, 117:342–343, 2007.

N. R. Lomb. Least-Squares Frequency Analysis of Unequally Spaced Data. Ap&SS, 39(2):447–462, February 1976. doi: 10.1007/BF00648343.

J. D. Scargle. Studies in astronomical time series analysis. II. Statistical aspects of spectral analysis of unevenly spaced data. ApJ, 263:835–853, December 1982. doi: 10.1086/160554.

R. P. Binzel, F. E. DeMeo, E. V. Turtelboom, S. J. Bus, A. Tokunaga, T. H. Burbine, C. Lantz, D. Polishook, B. Carry, A. Morbidelli, M. Birlan, P. Vernazza, B. J. Burt, N. Moskovitz, S. M. Slivan, C. A. Thomas, A. S. Rivkin, M. D. Hicks, T. Dunn, V. Reddy, J. A. Sanchez, M. Granvik, and T. Kohout. Compositional distributions and evolutionary processes for the near-Earth object population: Results from the MIT-Hawaii Near-Earth Object Spectroscopic Survey (MITHNEOS). icarus, 324: 41–76, May 2019. doi: 10.1016/j.icarus.2018.12.035.

Roger Dymock. *Asteroids and dwarf planets and how to observe them*. Springer, 2010.

Alan W. Harris and Alan W. Harris. On the Revision of Radiometric Albedos and Diameters of Asteroids. icarus, 126(2):450–454, April 1997. doi: 10.1006/icar.1996.5664.

Brian D. Warner, Alan W. Harris, and Petr Pravec. The asteroid lightcurve database. icarus, 202(1):134–146, July 2009. doi: 10.1016/j.icarus.2009.02.003.

Qiang Zhao, Le Yu, Zhenrong Du, Dailiang Peng, Pengyu Hao, Yongguang Zhang, and Peng Gong. An Overview of the Applications of Earth Observation Satellite Data: Impacts and Future Trends. *Remote Sensing*, 14(8):1863, April 2022. doi: 10.3390/rs14081863.

Shunlin Liang and Jindi Wang. *Advanced remote sensing: terrestrial information extraction and applications*. Academic Press, 2019.

D. Osgood. Farmers, scientists, and spacecraft: Climate change and the impact on smallholder farmers. `https://dc.alumni.columbia.edu/osgood`, 2017. Accessed: 2024-09-28.

Gaia Collaboration. VizieR Online Data Catalog: Gaia EDR3 (Gaia Collaboration, 2020). VizieR On-line Data Catalog: I/350. Originally published in: 2021A&A...649A...1G; doi:10.5270/esa-1ug, November 2020.

Appendix

In this appendix, you will find a table that consolidates the observations. The first column of the table contains filenames, each of which comprises the date and sequence number of a specific observation (e.g., MKD_20230715.0076.tab denotes an observation made on 15th July 2023 with a sequence number of 76). The second column specifies the type of object associated with each filename, e.g.,'134340' represents Pluto. Subsequent columns provide data on Airmass and Parallactic angle.

A Pluto

Filename	Object	Airmass	Parallactic angle
MKD_20230715.0076.tab	134340	1.42	-113.51
MKD_20230715.0077.tab	134340	1.36	-113.49
MKD_20230715.0142.tab	134340	1.16	-115.40
MKD_20230715.0143.tab	134340	1.14	-116.27
MKD_20230715.0186.tab	134340	1.05	-126.49
MKD_20230715.0280.tab	134340	1.02	139.22
MKD_20230715.0281.tab	134340	1.03	133.08
MKD_20230715.0323.tab	134340	1.08	119.79
MKD_20230715.0324.tab	134340	1.1	118.12
MKD_20230715.0366.tab	134340	1.2	114.32
MKD_20230715.0367.tab	134340	1.23	113.92
MKD_20230715.0423.tab	134340	1.49	113.6
MKD_20230715.0424.tab	134340	1.55	113.79
MKD_20230715.0039.tab	HD 190617	1.6	-114.84
MKD_20230715.0040.tab	HD 190617	1.59	-114.82
MKD_20230715.0041.tab	HD 190617	1.58	-114.81
MKD_20230715.0042.tab	HD 190617	1.58	-114.80
MKD_20230715.0043.tab	HD 190617	1.57	-114.79
MKD_20230715.0091.tab	HD 190617	1.28	-115.29
MKD_20230715.0092.tab	HD 190617	1.28	-115.32
MKD_20230715.0093.tab	HD 190617	1.27	-115.35
MKD_20230715.0094.tab	HD 190617	1.27	-115.38
MKD_20230715.0095.tab	HD 190617	1.27	-115.41
MKD_20230715.0128.tab	HD 190617	1.19	-116.62
MKD_20230715.0129.tab	HD 190617	1.19	-116.69
MKD_20230715.0130.tab	HD 190617	1.19	-116.75
MKD_20230715.0131.tab	HD 190617	1.18	-116.82
MKD_20230715.0132.tab	HD 190617	1.18	-116.88
MKD_20230715.0157.tab	HD 190617	1.1	-121.81
MKD_20230715.0158.tab	HD 190617	1.09	-121.98
MKD_20230715.0159.tab	HD 190617	1.09	-122.15
MKD_20230715.0160.tab	HD 190617	1.09	-122.33
MKD_20230715.0161.tab	HD 190617	1.09	-122.49
MKD_20230715.0171.tab	HD 190617	1.08	-123.81
MKD_20230715.0172.tab	HD 190617	1.08	-124.02
MKD_20230715.0173.tab	HD 190617	1.08	-124.22
MKD_20230715.0174.tab	HD 190617	1.08	-124.44
MKD_20230715.0175.tab	HD 190617	1.08	-124.65
MKD_20230715.0200.tab	HD 190617	1.03	-140.70
MKD_20230715.0201.tab	HD 190617	1.03	-141.27
MKD_20230715.0202.tab	HD 190617	1.03	-141.82

Filename	Object	Airmass	Parallactic angle
MKD_20230715.0203.tab	HD 190617	1.03	-142.38
MKD_20230715.0204.tab	HD 190617	1.03	-142.96
MKD_20230715.0214.tab	HD 190617	1.03	-147.56
MKD_20230715.0215.tab	HD 190617	1.03	-148.26
MKD_20230715.0216.tab	HD 190617	1.03	-148.95
MKD_20230715.0217.tab	HD 190617	1.03	-149.64
MKD_20230715.0218.tab	HD 190617	1.02	-150.35
MKD_20230715.0266.tab	HD 190617	1.02	150.44
MKD_20230715.0267.tab	HD 190617	1.02	149.7
MKD_20230715.0268.tab	HD 190617	1.02	148.99
MKD_20230715.0269.tab	HD 190617	1.02	148.3
MKD_20230715.0270.tab	HD 190617	1.02	147.62
MKD_20230715.0295.tab	HD 190617	1.06	127.47
MKD_20230715.0296.tab	HD 190617	1.06	127.18
MKD_20230715.0297.tab	HD 190617	1.06	126.92
MKD_20230715.0298.tab	HD 190617	1.06	126.66
MKD_20230715.0299.tab	HD 190617	1.06	126.4
MKD_20230715.0309.tab	HD 190617	1.07	124.7
MKD_20230715.0310.tab	HD 190617	1.07	124.48
MKD_20230715.0311.tab	HD 190617	1.07	124.26
MKD_20230715.0312.tab	HD 190617	1.07	124.05
MKD_20230715.0313.tab	HD 190617	1.08	123.85
MKD_20230715.0338.tab	HD 190617	1.15	117.75
MKD_20230715.0339.tab	HD 190617	1.15	117.66
MKD_20230715.0340.tab	HD 190617	1.15	117.57
MKD_20230715.0341.tab	HD 190617	1.15	117.49
MKD_20230715.0342.tab	HD 190617	1.16	117.41
MKD_20230715.0352.tab	HD 190617	1.17	116.84
MKD_20230715.0353.tab	HD 190617	1.18	116.77
MKD_20230715.0354.tab	HD 190617	1.18	116.71
MKD_20230715.0355.tab	HD 190617	1.18	116.64
MKD_20230715.0356.tab	HD 190617	1.18	116.58
MKD_20230715.0381.tab	HD 190617	1.32	114.86
MKD_20230715.0382.tab	HD 190617	1.32	114.84
MKD_20230715.0383.tab	HD 190617	1.32	114.82
MKD_20230715.0384.tab	HD 190617	1.33	114.81
MKD_20230715.0385.tab	HD 190617	1.33	114.79
MKD_20230715.0395.tab	HD 190617	1.39	114.65
MKD_20230715.0396.tab	HD 190617	1.39	114.64
MKD_20230715.0397.tab	HD 190617	1.4	114.64
MKD_20230715.0398.tab	HD 190617	1.4	114.63
MKD_20230715.0399.tab	HD 190617	1.41	114.63
MKD_20230715.0409.tab	HD 190617	1.44	114.62

Filename	Object	Airmass	Parallactic angle
MKD_20230715.0410.tab	HD 190617	1.45	114.62
MKD_20230715.0411.tab	HD 190617	1.45	114.62
MKD_20230715.0412.tab	HD 190617	1.46	114.62
MKD_20230715.0413.tab	HD 190617	1.46	114.62
MKD_20230715.0438.tab	HD 190617	1.75	115.2
MKD_20230715.0439.tab	HD 190617	1.76	115.22
MKD_20230715.0440.tab	HD 190617	1.77	115.25
MKD_20230715.0441.tab	HD 190617	1.78	115.27
MKD_20230715.0442.tab	HD 190617	1.79	115.29
MKD_20230712.1270.tab	134340	1.56	-113.83
MKD_20230712.1271.tab	134340	1.49	-113.66
MKD_20230712.1313.tab	134340	1.27	-113.79
MKD_20230712.1314.tab	134340	1.23	-114.08
MKD_20230712.1342.tab	134340	1.11	-117.78
MKD_20230712.1343.tab	134340	1.09	-119.32
MKD_20230712.1371.tab	134340	1.03	-135.04
MKD_20230712.1372.tab	134340	1.02	-141.69
MKD_20230712.1432.tab	134340	1.02	155.61
MKD_20230712.1433.tab	134340	1.02	145.8
MKD_20230712.1461.tab	134340	1.06	121.99
MKD_20230712.1462.tab	134340	1.08	119.84
MKD_20230712.1490.tab	134340	1.17	114.93
MKD_20230712.1491.tab	134340	1.19	114.37
MKD_20230712.1529.tab	134340	1.43	113.5
MKD_20230712.1530.tab	134340	1.49	113.63
MKD_20230712.1285.tab	HD 190617	1.38	-114.76
MKD_20230712.1286.tab	HD 190617	1.38	-114.77
MKD_20230712.1287.tab	HD 190617	1.37	-114.79
MKD_20230712.1288.tab	HD 190617	1.37	-114.80
MKD_20230712.1289.tab	HD 190617	1.37	-114.81
MKD_20230712.1299.tab	HD 190617	1.34	-114.91
MKD_20230712.1300.tab	HD 190617	1.33	-114.93
MKD_20230712.1301.tab	HD 190617	1.33	-114.95
MKD_20230712.1302.tab	HD 190617	1.33	-114.96
MKD_20230712.1303.tab	HD 190617	1.32	-114.98
MKD_20230712.1328.tab	HD 190617	1.15	-118.19
MKD_20230712.1329.tab	HD 190617	1.14	-118.29
MKD_20230712.1330.tab	HD 190617	1.14	-118.39
MKD_20230712.1331.tab	HD 190617	1.14	-118.48
MKD_20230712.1332.tab	HD 190617	1.14	-118.58
MKD_20230712.1357.tab	HD 190617	1.05	-131.66
MKD_20230712.1358.tab	HD 190617	1.05	-132.03
MKD_20230712.1359.tab	HD 190617	1.05	-132.40

Filename	Object	Airmass	Parallactic angle
MKD_20230712.1360.tab	HD 190617	1.05	-132.78
MKD_20230712.1361.tab	HD 190617	1.04	-133.16
MKD_20230712.1447.tab	HD 190617	1.06	127.72
MKD_20230712.1448.tab	HD 190617	1.06	127.43
MKD_20230712.1449.tab	HD 190617	1.06	127.16
MKD_20230712.1450.tab	HD 190617	1.06	126.89
MKD_20230712.1451.tab	HD 190617	1.06	126.63
MKD_20230712.1476.tab	HD 190617	1.13	118.34
MKD_20230712.1477.tab	HD 190617	1.14	118.24
MKD_20230712.1478.tab	HD 190617	1.14	118.15
MKD_20230712.1479.tab	HD 190617	1.14	118.05
MKD_20230712.1480.tab	HD 190617	1.14	117.96
MKD_20230712.1515.tab	HD 190617	1.39	114.64
MKD_20230712.1516.tab	HD 190617	1.4	114.64
MKD_20230712.1517.tab	HD 190617	1.4	114.63
MKD_20230712.1518.tab	HD 190617	1.41	114.63
MKD_20230712.1519.tab	HD 190617	1.41	114.63
MKD_20230724.0101.tab	134340	1.12	-117.03
MKD_20230724.0102.tab	134340	1.1	-118.38
MKD_20230724.0126.tab	134340	1.05	-125.34
MKD_20230724.0127.tab	134340	1.04	-129.09
MKD_20230724.0175.tab	134340	1.02	148.73
MKD_20230724.0176.tab	134340	1.02	140.33
MKD_20230724.0200.tab	134340	1.06	123.33
MKD_20230724.0201.tab	134340	1.07	120.86
MKD_20230724.0225.tab	134340	1.14	115.67
MKD_20230724.0226.tab	134340	1.16	114.91
MKD_20230724.0250.tab	134340	1.28	113.5
MKD_20230724.0251.tab	134340	1.32	113.38
MKD_20230724.0275.tab	134340	1.51	113.6
MKD_20230724.0276.tab	134340	1.58	113.81
MKD_20230724.0112.tab	HD 190617	1.07	-125.06
MKD_20230724.0113.tab	HD 190617	1.07	-125.30
MKD_20230724.0114.tab	HD 190617	1.07	-125.53
MKD_20230724.0115.tab	HD 190617	1.07	-125.77
MKD_20230724.0116.tab	HD 190617	1.07	-126.01
MKD_20230724.0138.tab	HD 190617	1.03	-147.72
MKD_20230724.0186.tab	HD 190617	1.05	130.85
MKD_20230724.0187.tab	HD 190617	1.05	130.5
MKD_20230724.0188.tab	HD 190617	1.05	130.16
MKD_20230724.0189.tab	HD 190617	1.05	129.84
MKD_20230724.0190.tab	HD 190617	1.05	129.52
MKD_20230724.0211.tab	HD 190617	1.12	119.3

Filename	Object	Airmass	Parallactic angle
MKD_20230724.0212.tab	HD 190617	1.12	119.18
MKD_20230724.0213.tab	HD 190617	1.12	119.06
MKD_20230724.0214.tab	HD 190617	1.12	118.95
MKD_20230724.0215.tab	HD 190617	1.12	118.84
MKD_20230724.0236.tab	HD 190617	1.24	115.47
MKD_20230724.0237.tab	HD 190617	1.25	115.43
MKD_20230724.0238.tab	HD 190617	1.25	115.4
MKD_20230724.0239.tab	HD 190617	1.25	115.37
MKD_20230724.0240.tab	HD 190617	1.25	115.33
MKD_20230724.0261.tab	HD 190617	1.45	114.62
MKD_20230724.0262.tab	HD 190617	1.46	114.62
MKD_20230724.0263.tab	HD 190617	1.46	114.62
MKD_20230724.0264.tab	HD 190617	1.47	114.63
MKD_20230724.0265.tab	HD 190617	1.47	114.63
MKD_20230722.0312.tab	134340	1.01	177.06
MKD_20230722.0313.tab	134340	1.01	163.91
MKD_20230722.0337.tab	134340	1.03	132.01
MKD_20230722.0338.tab	134340	1.04	127.54
MKD_20230722.0362.tab	134340	1.09	118.78
MKD_20230722.0363.tab	134340	1.1	117.32
MKD_20230722.0387.tab	134340	1.18	114.62
MKD_20230722.0388.tab	134340	1.2	114.13
MKD_20230722.0412.tab	134340	1.31	113.41
MKD_20230722.0413.tab	134340	1.35	113.36
MKD_20230722.0433.tab	134340	1.51	113.63
MKD_20230722.0434.tab	134340	1.58	113.85
MKD_20230722.0153.tab	HD 190617	1.61	-114.87
MKD_20230722.0154.tab	HD 190617	1.61	-114.85
MKD_20230722.0155.tab	HD 190617	1.6	-114.84
MKD_20230722.0156.tab	HD 190617	1.59	-114.83
MKD_20230722.0163.tab	HD 190617	1.45	-114.69
MKD_20230722.0164.tab	HD 190617	1.45	-114.69
MKD_20230722.0165.tab	HD 190617	1.44	-114.69
MKD_20230722.0166.tab	HD 190617	1.44	-114.69
MKD_20230722.0167.tab	HD 190617	1.43	-114.70
MKD_20230722.0188.tab	HD 190617	1.24	-115.71
MKD_20230722.0189.tab	HD 190617	1.24	-115.75
MKD_20230722.0190.tab	HD 190617	1.24	-115.79
MKD_20230722.0191.tab	HD 190617	1.23	-115.83
MKD_20230722.0192.tab	HD 190617	1.23	-115.88
MKD_20230722.0220.tab	HD 190617	1.16	-117.55
MKD_20230722.0221.tab	HD 190617	1.16	-117.63
MKD_20230722.0222.tab	HD 190617	1.16	-117.72

Filename	Object	Airmass	Parallactic angle
MKD_20230722.0223.tab	HD 190617	1.16	-117.80
MKD_20230722.0224.tab	HD 190617	1.15	-117.89
MKD_20230722.0253.tab	HD 190617	1.07	-126.29
MKD_20230722.0254.tab	HD 190617	1.07	-126.55
MKD_20230722.0255.tab	HD 190617	1.06	-126.81
MKD_20230722.0256.tab	HD 190617	1.06	-127.07
MKD_20230722.0257.tab	HD 190617	1.06	-127.34
MKD_20230722.0265.tab	HD 190617	1.03	-145.20
MKD_20230722.0266.tab	HD 190617	1.03	-145.85
MKD_20230722.0267.tab	HD 190617	1.03	-146.50
MKD_20230722.0268.tab	HD 190617	1.03	-147.15
MKD_20230722.0269.tab	HD 190617	1.03	-147.81
MKD_20230722.0298.tab	HD 190617	1.02	-169.75
MKD_20230722.0299.tab	HD 190617	1.02	-170.75
MKD_20230722.0300.tab	HD 190617	1.02	-171.73
MKD_20230722.0301.tab	HD 190617	1.02	-172.71
MKD_20230722.0302.tab	HD 190617	1.02	-173.70
MKD_20230722.0323.tab	HD 190617	1.02	147.28
MKD_20230722.0324.tab	HD 190617	1.03	146.59
MKD_20230722.0325.tab	HD 190617	1.03	145.94
MKD_20230722.0326.tab	HD 190617	1.03	145.3
MKD_20230722.0327.tab	HD 190617	1.03	144.68
MKD_20230722.0348.tab	HD 190617	1.07	124.06
MKD_20230722.0349.tab	HD 190617	1.08	123.84
MKD_20230722.0350.tab	HD 190617	1.08	123.64
MKD_20230722.0351.tab	HD 190617	1.08	123.44
MKD_20230722.0352.tab	HD 190617	1.08	123.25
MKD_20230722.0373.tab	HD 190617	1.15	117.47
MKD_20230722.0374.tab	HD 190617	1.16	117.38
MKD_20230722.0375.tab	HD 190617	1.16	117.31
MKD_20230722.0376.tab	HD 190617	1.16	117.23
MKD_20230722.0377.tab	HD 190617	1.16	117.15
MKD_20230722.0398.tab	HD 190617	1.28	115.12
MKD_20230722.0399.tab	HD 190617	1.28	115.09
MKD_20230722.0400.tab	HD 190617	1.28	115.06
MKD_20230722.0401.tab	HD 190617	1.29	115.04
MKD_20230722.0402.tab	HD 190617	1.29	115.02
MKD_20230722.0444.tab	HD 190617	1.77	115.24
MKD_20230722.0445.tab	HD 190617	1.78	115.26
MKD_20230722.0446.tab	HD 190617	1.78	115.28
MKD_20230722.0447.tab	HD 190617	1.79	115.31
MKD_20230722.0448.tab	HD 190617	1.8	115.33
MKD_20230713.0094.tab	134340	1.55	-113.79

Filename	Object	Airmass	Parallactic angle
MKD_20230713.0095.tab	134340	1.48	-113.63
MKD_20230713.0137.tab	134340	1.25	-113.88
MKD_20230713.0138.tab	134340	1.22	-114.23
MKD_20230713.0189.tab	134340	1.08	-119.81
MKD_20230713.0190.tab	134340	1.07	-121.92
MKD_20230713.0234.tab	134340	1.02	157.8
MKD_20230713.0235.tab	134340	1.02	147.56
MKD_20230713.0263.tab	134340	1.08	120.28
MKD_20230713.0264.tab	134340	1.09	118.5
MKD_20230713.0278.tab	134340	1.17	114.73
MKD_20230713.0279.tab	134340	1.2	114.22
MKD_20230713.0321.tab	134340	1.39	113.44
MKD_20230713.0322.tab	134340	1.45	113.52
MKD_20230713.0066.tab	HD 190617	1.78	-115.26
MKD_20230713.0067.tab	HD 190617	1.78	-115.24
MKD_20230713.0068.tab	HD 190617	1.77	-115.22
MKD_20230713.0069.tab	HD 190617	1.76	-115.20
MKD_20230713.0070.tab	HD 190617	1.75	-115.18
MKD_20230713.0080.tab	HD 190617	1.7	-115.04
MKD_20230713.0081.tab	HD 190617	1.69	-115.02
MKD_20230713.0082.tab	HD 190617	1.68	-115.01
MKD_20230713.0083.tab	HD 190617	1.67	-114.99
MKD_20230713.0084.tab	HD 190617	1.67	-114.97
MKD_20230713.0109.tab	HD 190617	1.38	-114.78
MKD_20230713.0110.tab	HD 190617	1.37	-114.79
MKD_20230713.0111.tab	HD 190617	1.37	-114.80
MKD_20230713.0112.tab	HD 190617	1.36	-114.81
MKD_20230713.0113.tab	HD 190617	1.36	-114.82
MKD_20230713.0123.tab	HD 190617	1.33	-114.94
MKD_20230713.0124.tab	HD 190617	1.33	-114.96
MKD_20230713.0125.tab	HD 190617	1.32	-114.98
MKD_20230713.0126.tab	HD 190617	1.32	-115.00
MKD_20230713.0127.tab	HD 190617	1.32	-115.02
MKD_20230713.0175.tab	HD 190617	1.11	-120.75
MKD_20230713.0176.tab	HD 190617	1.1	-120.90
MKD_20230713.0177.tab	HD 190617	1.1	-121.04
MKD_20230713.0178.tab	HD 190617	1.1	-121.19
MKD_20230713.0179.tab	HD 190617	1.1	-121.35
MKD_20230713.0220.tab	HD 190617	1.02	-169.48
MKD_20230713.0221.tab	HD 190617	1.02	-170.48
MKD_20230713.0222.tab	HD 190617	1.02	-171.46
MKD_20230713.0223.tab	HD 190617	1.02	-172.44
MKD_20230713.0224.tab	HD 190617	1.02	-173.43

Filename	Object	Airmass	Parallactic angle
MKD_20230713.0249.tab	HD 190617	1.07	125.36
MKD_20230713.0250.tab	HD 190617	1.07	125.12
MKD_20230713.0251.tab	HD 190617	1.07	124.89
MKD_20230713.0252.tab	HD 190617	1.07	124.67
MKD_20230713.0253.tab	HD 190617	1.07	124.45
MKD_20230713.0293.tab	HD 190617	1.29	115.02
MKD_20230713.0294.tab	HD 190617	1.29	115
MKD_20230713.0295.tab	HD 190617	1.3	114.98
MKD_20230713.0296.tab	HD 190617	1.3	114.96
MKD_20230713.0297.tab	HD 190617	1.3	114.94
MKD_20230713.0307.tab	HD 190617	1.33	114.81
MKD_20230713.0308.tab	HD 190617	1.33	114.79
MKD_20230713.0309.tab	HD 190617	1.34	114.78
MKD_20230713.0310.tab	HD 190617	1.34	114.76
MKD_20230713.0311.tab	HD 190617	1.34	114.75
MKD_20230714.0107.tab	134340	1.11	117.03
MKD_20230714.0108.tab	134340	1.13	115.97
MKD_20230714.0122.tab	134340	1.19	114.42
MKD_20230714.0123.tab	134340	1.22	113.99
MKD_20230714.0156.tab	134340	1.37	113.41
MKD_20230714.0157.tab	134340	1.42	113.46
MKD_20230714.0009.tab	HD 190617	1.03	143.78
MKD_20230714.0010.tab	HD 190617	1.03	143.16
MKD_20230714.0011.tab	HD 190617	1.03	142.58
MKD_20230714.0012.tab	HD 190617	1.03	142
MKD_20230714.0013.tab	HD 190617	1.03	141.44
MKD_20230714.0014.tab	HD 190617	1.03	140.89
MKD_20230714.0015.tab	HD 190617	1.03	140.35
MKD_20230714.0016.tab	HD 190617	1.03	139.82
MKD_20230714.0017.tab	HD 190617	1.03	139.3
MKD_20230714.0018.tab	HD 190617	1.03	138.8
MKD_20230714.0019.tab	HD 190617	1.03	138.3
MKD_20230714.0020.tab	HD 190617	1.03	137.81
MKD_20230714.0021.tab	HD 190617	1.03	137.33
MKD_20230714.0022.tab	HD 190617	1.04	136.86
MKD_20230714.0023.tab	HD 190617	1.04	136.4
MKD_20230714.0024.tab	HD 190617	1.04	135.95
MKD_20230714.0025.tab	HD 190617	1.04	135.51
MKD_20230714.0026.tab	HD 190617	1.04	135.08
MKD_20230714.0027.tab	HD 190617	1.04	134.65
MKD_20230714.0028.tab	HD 190617	1.04	134.23
MKD_20230714.0137.tab	HD 190617	1.31	114.88
MKD_20230714.0138.tab	HD 190617	1.32	114.86

Filename	Object	Airmass	Parallactic angle
MKD_20230714.0139.tab	HD 190617	1.32	114.84
MKD_20230714.0140.tab	HD 190617	1.32	114.83
MKD_20230714.0141.tab	HD 190617	1.33	114.81
MKD_20230714.0142.tab	HD 190617	1.33	114.8
MKD_20230714.0143.tab	HD 190617	1.34	114.78
MKD_20230714.0144.tab	HD 190617	1.34	114.77
MKD_20230714.0145.tab	HD 190617	1.34	114.75
MKD_20230714.0146.tab	HD 190617	1.35	114.74
MKD_20230623.0223.tab	134340	1.34	-113.67
MKD_20230623.0233.tab	134340	1.27	-113.96
MKD_20230623.0310.tab	134340	1.06	-124.82
MKD_20230623.0324.tab	134340	1.03	-133.64
MKD_20230623.0352.tab	134340	1.02	-161.81
MKD_20230623.0353.tab	134340	1.01	-174.46
MKD_20230623.0354.tab	134340	1.01	172.28
MKD_20230623.0411.tab	134340	1.06	123.77
MKD_20230623.0412.tab	134340	1.07	121.27
MKD_20230623.0413.tab	134340	1.09	119.32
MKD_20230623.0147.tab	HD 190617	1.77	-115.23
MKD_20230623.0247.tab	HD 190617	1.17	-117.20
MKD_20230623.0257.tab	HD 190617	1.15	-118.01
MKD_20230711.0082.tab	134340	1.49	-113.66
MKD_20230711.0083.tab	134340	1.43	-113.55
MKD_20230711.0125.tab	134340	1.25	-113.97
MKD_20230711.0126.tab	134340	1.21	-114.34
MKD_20230711.0168.tab	134340	1.11	-117.92
MKD_20230711.0169.tab	134340	1.09	-119.50
MKD_20230711.0211.tab	134340	1.03	-135.45
MKD_20230711.0212.tab	134340	1.02	-142.22
MKD_20230711.0265.tab	134340	1.02	147.89
MKD_20230711.0266.tab	134340	1.02	139.75
MKD_20230711.0326.tab	134340	1.09	118.88
MKD_20230711.0327.tab	134340	1.11	117.42
MKD_20230711.0341.tab	134340	1.15	115.27
MKD_20230711.0342.tab	134340	1.18	114.62
MKD_20230711.0367.tab	134340	1.5	113.64
MKD_20230711.0368.tab	134340	1.56	113.83
MKD_20230711.0068.tab	HD 190617	1.59	-114.82
MKD_20230711.0069.tab	HD 190617	1.58	-114.81
MKD_20230711.0070.tab	HD 190617	1.57	-114.79
MKD_20230711.0071.tab	HD 190617	1.56	-114.77
MKD_20230711.0072.tab	HD 190617	1.55	-114.76
MKD_20230711.0097.tab	HD 190617	1.33	-114.94

Filename	Object	Airmass	Parallactic angle
MKD_20230711.0098.tab	HD 190617	1.33	-114.96
MKD_20230711.0099.tab	HD 190617	1.32	-114.98
MKD_20230711.0100.tab	HD 190617	1.32	-115.00
MKD_20230711.0101.tab	HD 190617	1.32	-115.02
MKD_20230711.0111.tab	HD 190617	1.29	-115.19
MKD_20230711.0112.tab	HD 190617	1.29	-115.22
MKD_20230711.0113.tab	HD 190617	1.28	-115.25
MKD_20230711.0115.tab	HD 190617	1.28	-115.30
MKD_20230711.0140.tab	HD 190617	1.15	-117.88
MKD_20230711.0141.tab	HD 190617	1.15	-117.97
MKD_20230711.0142.tab	HD 190617	1.15	-118.06
MKD_20230711.0143.tab	HD 190617	1.15	-118.15
MKD_20230711.0144.tab	HD 190617	1.15	-118.25
MKD_20230711.0154.tab	HD 190617	1.13	-118.96
MKD_20230711.0155.tab	HD 190617	1.13	-119.07
MKD_20230711.0156.tab	HD 190617	1.13	-119.18
MKD_20230711.0157.tab	HD 190617	1.13	-119.29
MKD_20230711.0158.tab	HD 190617	1.12	-119.41
MKD_20230711.0183.tab	HD 190617	1.05	-130.03
MKD_20230711.0184.tab	HD 190617	1.05	-130.37
MKD_20230711.0185.tab	HD 190617	1.05	-130.71
MKD_20230711.0198.tab	HD 190617	1.04	-134.51
MKD_20230711.0199.tab	HD 190617	1.04	-134.93
MKD_20230716.0090.tab	134340	1.47	-113.59
MKD_20230716.0091.tab	134340	1.42	-113.50
MKD_20230716.0138.tab	134340	1.22	-114.27
MKD_20230716.0139.tab	134340	1.18	-114.77
MKD_20230716.0192.tab	134340	1.01	-164.65
MKD_20230716.0193.tab	134340	1.01	-177.80
MKD_20230716.0218.tab	134340	1.02	143.35
MKD_20230716.0219.tab	134340	1.03	136.23
MKD_20230716.0267.tab	134340	1.08	119.76
MKD_20230716.0268.tab	134340	1.1	118.09
MKD_20230716.0352.tab	134340	1.46	113.53
MKD_20230716.0353.tab	134340	1.52	113.69
MKD_20230716.0079.tab	HD 190617	1.77	-115.22
MKD_20230716.0080.tab	HD 190617	1.76	-115.20
MKD_20230716.0105.tab	HD 190617	1.32	-114.98
MKD_20230716.0106.tab	HD 190617	1.32	-115.00
MKD_20230716.0116.tab	HD 190617	1.29	-115.18
MKD_20230716.0117.tab	HD 190617	1.29	-115.21
MKD_20230716.0127.tab	HD 190617	1.25	-115.62
MKD_20230716.0128.tab	HD 190617	1.25	-115.66

Filename	Object	Airmass	Parallactic angle
MKD_20230716.0153.tab	HD 190617	1.13	-119.18
MKD_20230716.0154.tab	HD 190617	1.13	-119.30
MKD_20230716.0181.tab	HD 190617	1.02	-158.66
MKD_20230716.0182.tab	HD 190617	1.02	-159.55
MKD_20230716.0207.tab	HD 190617	1.02	155.89
MKD_20230716.0208.tab	HD 190617	1.02	155.05
MKD_20230716.0256.tab	HD 190617	1.07	124.15
MKD_20230716.0257.tab	HD 190617	1.07	123.94
MKD_20230716.0282.tab	HD 190617	1.15	117.76
MKD_20230716.0283.tab	HD 190617	1.15	117.67
MKD_20230716.0293.tab	HD 190617	1.17	117
MKD_20230716.0294.tab	HD 190617	1.17	116.92
MKD_20230716.0319.tab	HD 190617	1.34	114.77
MKD_20230716.0320.tab	HD 190617	1.34	114.75
MKD_20230716.0330.tab	HD 190617	1.37	114.67
MKD_20230716.0331.tab	HD 190617	1.38	114.66
MKD_20230716.0341.tab	HD 190617	1.43	114.62
MKD_20230716.0342.tab	HD 190617	1.44	114.62
MKD_20230716.0367.tab	HD 190617	1.75	115.2
MKD_20230716.0368.tab	HD 190617	1.76	115.22
MKD_20230720.0106.tab	134340	1.63	-114.00
MKD_20230720.0107.tab	134340	1.56	-113.78
MKD_20230720.0155.tab	134340	1.26	-113.78
MKD_20230720.0156.tab	134340	1.23	-114.09
MKD_20230720.0166.tab	HD 190617	1.18	-117.06
MKD_20230721.0033.tab	134340	1.3	-113.57
MKD_20230721.0034.tab	134340	1.26	-113.76
MKD_20230721.0068.tab	134340	1.15	-115.78
MKD_20230721.0120.tab	134340	1.01	-167.18
MKD_20230721.0121.tab	134340	1.01	179.45
MKD_20230721.0178.tab	134340	1.04	129.52
MKD_20230721.0203.tab	134340	1.11	116.96
MKD_20230721.0204.tab	134340	1.13	115.9
MKD_20230721.0044.tab	HD 190617	1.21	-116.29
MKD_20230721.0045.tab	HD 190617	1.2	-116.35
MKD_20230721.0046.tab	HD 190617	1.2	-116.40
MKD_20230721.0047.tab	HD 190617	1.2	-116.46
MKD_20230721.0048.tab	HD 190617	1.2	-116.52
MKD_20230721.0054.tab	HD 190617	1.18	-116.92
MKD_20230721.0055.tab	HD 190617	1.18	-116.99
MKD_20230721.0056.tab	HD 190617	1.18	-117.06
MKD_20230721.0057.tab	HD 190617	1.18	-117.13
MKD_20230721.0058.tab	HD 190617	1.17	-117.20

Filename	Object	Airmass	Parallactic angle
MKD_20230721.0079.tab	HD 190617	1.09	-122.16
MKD_20230721.0080.tab	HD 190617	1.09	-122.33
MKD_20230721.0081.tab	HD 190617	1.09	-122.51
MKD_20230721.0082.tab	HD 190617	1.09	-122.68
MKD_20230721.0083.tab	HD 190617	1.09	-122.86
MKD_20230721.0096.tab	HD 190617	1.03	-141.40
MKD_20230721.0097.tab	HD 190617	1.03	-141.98
MKD_20230721.0098.tab	HD 190617	1.03	-142.55
MKD_20230721.0099.tab	HD 190617	1.03	-143.12
MKD_20230721.0100.tab	HD 190617	1.03	-143.71
MKD_20230721.0106.tab	HD 190617	1.02	-151.62
MKD_20230721.0107.tab	HD 190617	1.02	-152.39
MKD_20230721.0108.tab	HD 190617	1.02	-153.15
MKD_20230721.0109.tab	HD 190617	1.02	-153.92
MKD_20230721.0131.tab	HD 190617	1.02	157.6
MKD_20230721.0132.tab	HD 190617	1.02	156.74
MKD_20230721.0133.tab	HD 190617	1.02	155.92
MKD_20230721.0134.tab	HD 190617	1.02	155.11
MKD_20230721.0135.tab	HD 190617	1.02	154.32
MKD_20230721.0164.tab	HD 190617	1.03	138.53
MKD_20230721.0165.tab	HD 190617	1.03	138.02
MKD_20230721.0166.tab	HD 190617	1.03	137.54
MKD_20230721.0167.tab	HD 190617	1.03	137.06
MKD_20230721.0168.tab	HD 190617	1.04	136.6
MKD_20230721.0189.tab	HD 190617	1.08	123.45
MKD_20230721.0190.tab	HD 190617	1.08	123.25
MKD_20230721.0191.tab	HD 190617	1.08	123.06
MKD_20230721.0192.tab	HD 190617	1.08	122.87
MKD_20230721.0193.tab	HD 190617	1.08	122.69
MKD_20230721.0214.tab	HD 190617	1.19	116.39
MKD_20230721.0215.tab	HD 190617	1.19	116.33
MKD_20230721.0216.tab	HD 190617	1.19	116.28
MKD_20230721.0217.tab	HD 190617	1.2	116.22
MKD_20230721.0218.tab	HD 190617	1.2	116.17
MKD_20230721.0224.tab	HD 190617	1.22	115.75
MKD_20230721.0225.tab	HD 190617	1.23	115.7
MKD_20230721.0226.tab	HD 190617	1.23	115.66
MKD_20230721.0227.tab	HD 190617	1.23	115.62
MKD_20230721.0228.tab	HD 190617	1.23	115.58
MKD_20230721.0241.tab	HD 190617	1.41	114.63
MKD_20230721.0242.tab	HD 190617	1.41	114.62
MKD_20230721.0243.tab	HD 190617	1.42	114.62
MKD_20230721.0244.tab	HD 190617	1.42	114.62

Filename	Object	Airmass	Parallactic angle
MKD_20230721.0245.tab	HD 190617	1.43	114.62
MKD_20230717.0137.tab	134340	1.68	-114.15
MKD_20230717.0138.tab	134340	1.6	-113.90
MKD_20230717.0159.tab	134340	1.42	-113.51
MKD_20230717.0160.tab	134340	1.37	-113.48
MKD_20230717.0216.tab	134340	1.15	-115.66
MKD_20230717.0217.tab	134340	1.13	-116.61
MKD_20230717.0238.tab	134340	1.08	-120.93
MKD_20230717.0239.tab	134340	1.06	-123.36
MKD_20230717.0304.tab	134340	1.03	136.64
MKD_20230717.0305.tab	134340	1.03	131.09
MKD_20230717.0326.tab	134340	1.08	119.22
MKD_20230717.0327.tab	134340	1.1	117.67
MKD_20230717.0355.tab	134340	1.22	113.99
MKD_20230717.0356.tab	134340	1.25	113.69
MKD_20230717.0148.tab	HD 190617	1.48	-114.69
MKD_20230717.0149.tab	HD 190617	1.47	-114.69
MKD_20230717.0170.tab	HD 190617	1.29	-115.17
MKD_20230717.0171.tab	HD 190617	1.29	-115.19
MKD_20230717.0205.tab	HD 190617	1.18	-117.09
MKD_20230717.0206.tab	HD 190617	1.17	-117.16
MKD_20230717.0228.tab	HD 190617	1.09	-122.26
MKD_20230717.0249.tab	HD 190617	1.04	-133.64
MKD_20230717.0250.tab	HD 190617	1.04	-134.06
MKD_20230717.0263.tab	HD 190617	1.02	170.13
MKD_20230717.0264.tab	HD 190617	1.02	169.12
MKD_20230717.0293.tab	HD 190617	1.03	146.65
MKD_20230717.0294.tab	HD 190617	1.03	145.98
MKD_20230717.0315.tab	HD 190617	1.06	127.01
MKD_20230717.0316.tab	HD 190617	1.06	126.74
MKD_20230717.0337.tab	HD 190617	1.15	117.56
MKD_20230717.0338.tab	HD 190617	1.15	117.47
MKD_20230717.0344.tab	HD 190617	1.16	117.08
MKD_20230717.0345.tab	HD 190617	1.17	117.01
MKD_20230717.0366.tab	HD 190617	1.34	114.76
MKD_20230717.0367.tab	HD 190617	1.34	114.74
MKD_20230710.0031.tab	134340	1.27	-113.82
MKD_20230710.0032.tab	134340	1.23	-114.12
MKD_20230710.0080.tab	134340	1.1	-118.28
MKD_20230710.0123.tab	134340	1.03	-135.93
MKD_20230710.0124.tab	134340	1.02	-142.84
MKD_20230710.0149.tab	134340	1.01	171.72
MKD_20230710.0150.tab	134340	1.02	159.23

Filename	Object	Airmass	Parallactic angle
MKD_20230710.0209.tab	134340	1.06	123.74
MKD_20230710.0210.tab	134340	1.07	121.2
MKD_20230710.0235.tab	134340	1.14	115.56
MKD_20230710.0236.tab	134340	1.17	114.84
MKD_20230710.0261.tab	134340	1.34	113.45
MKD_20230710.0262.tab	134340	1.39	113.45
MKD_20230710.0138.tab	HD 190617	1.02	-169.63
MKD_20230710.0139.tab	HD 190617	1.02	-171.18
MKD_20230710.0187.tab	HD 190617	1.04	132.45
MKD_20230710.0188.tab	HD 190617	1.04	131.86
MKD_20230710.0198.tab	HD 190617	1.05	129.09
MKD_20230710.0199.tab	HD 190617	1.05	128.6
MKD_20230710.0224.tab	HD 190617	1.12	119.23
MKD_20230710.0225.tab	HD 190617	1.12	119.05
MKD_20230710.0250.tab	HD 190617	1.29	115.01
MKD_20230710.0251.tab	HD 190617	1.3	114.97
MKD_20230710.0276.tab	HD 190617	1.62	114.87
MKD_20230710.0277.tab	HD 190617	1.63	114.89

B 2005 EK70

Filename	Object	Observation time	Airmass	Parallactic angle
MKD_20240224.0247.tab	2005 EK70	2024-02-24T19:09:14.856	1.27	-140.3408094
MKD_20240224.0248.tab	2005 EK70	2024-02-24T19:10:46.441	1.27	-140.6880864
MKD_20240224.0249.tab	2005 EK70	2024-02-24T19:12:14.844	1.26	-141.0282153
MKD_20240224.0250.tab	2005 EK70	2024-02-24T19:13:47.453	1.26	-141.3897189
MKD_20240224.0251.tab	2005 EK70	2024-02-24T19:15:34.280	1.25	-141.8139427
MKD_20240224.0272.tab	2005 EK70	2024-02-24T19:31:10.574	1.22	-145.8580517
MKD_20240224.0273.tab	2005 EK70	2024-02-24T19:32:41.730	1.22	-146.2846411
MKD_20240224.0274.tab	2005 EK70	2024-02-24T19:34:08.771	1.21	-146.697552
MKD_20240224.0275.tab	2005 EK70	2024-02-24T19:35:42.212	1.21	-147.1470551
MKD_20240224.0276.tab	2005 EK70	2024-02-24T19:37:12.331	1.21	-147.5865609
MKD_20240224.0304.tab	2005 EK70	2024-02-24T19:54:08.084	1.18	-152.9649151
MKD_20240224.0305.tab	2005 EK70	2024-02-24T19:55:39.422	1.17	-153.486735
MKD_20240224.0306.tab	2005 EK70	2024-02-24T19:57:08.685	1.17	-154.0026941
MKD_20240224.0307.tab	2005 EK70	2024-02-24T19:58:36.830	1.17	-154.5182409
MKD_20240224.0308.tab	2005 EK70	2024-02-24T20:00:05.030	1.17	-155.0399492
MKD_20240224.0327.tab	2005 EK70	2024-02-24T20:20:47.709	1.14	-162.9858145
MKD_20240224.0328.tab	2005 EK70	2024-02-24T20:22:16.732	1.14	-163.5962005
MKD_20240224.0329.tab	2005 EK70	2024-02-24T20:23:48.443	1.14	-164.2302107
MKD_20240224.0330.tab	2005 EK70	2024-02-24T20:25:20.233	1.14	-164.8698728
MKD_20240224.0331.tab	2005 EK70	2024-02-24T20:27:20.168	1.14	-165.7130713
MKD_20240224.0224.tab	HD76151	2024-02-24T18:53:34.332	1.36	-133.8865054
MKD_20240224.0225.tab	HD76151	2024-02-24T18:54:28.039	1.35	-134.035236
MKD_20240224.0226.tab	HD76151	2024-02-24T18:55:03.929	1.35	-134.1353683
MKD_20240224.0259.tab	HD76151	2024-02-24T19:22:32.296	1.26	-139.4857494
MKD_20240224.0260.tab	HD76151	2024-02-24T19:23:09.513	1.26	-139.6246972
MKD_20240224.0287.tab	HD76151	2024-02-24T19:45:02.421	1.21	-145.1278123
MKD_20240224.0289.tab	HD76151	2024-02-24T19:46:24.430	1.2	-145.5116986
MKD_20240224.0315.tab	HD76151	2024-02-24T20:05:53.744	1.17	-151.5426403
MKD_20240224.0316.tab	HD76151	2024-02-24T20:06:56.202	1.17	-151.8947264

C Meteosat-11

Filename	Object	Observation time	Airmass	Parallactic angle
MKD_20240225.0186.tab	Meteosat11	2024-02-25T18:26:18.005	1.3	197
MKD_20240225.0188.tab	Meteosat11	2024-02-25T18:29:18.937	1.3	197
MKD_20240225.0189.tab	Meteosat11	2024-02-25T18:30:48.680	1.3	197
MKD_20240225.0190.tab	Meteosat11	2024-02-25T18:32:14.965	1.3	197
MKD_20240225.0191.tab	Meteosat11	2024-02-25T18:33:45.890	1.3	197
MKD_20240225.0192.tab	Meteosat11	2024-02-25T18:35:15.362	1.3	197
MKD_20240225.0200.tab	Meteosat11	2024-02-25T18:38:38.432	1.3	197
MKD_20240225.0214.tab	Meteosat11	2024-02-25T18:45:16.043	1.3	197
MKD_20240225.0215.tab	Meteosat11	2024-02-25T18:46:53.446	1.3	197
MKD_20240225.0216.tab	Meteosat11	2024-02-25T18:48:19.611	1.3	197
MKD_20240225.0217.tab	Meteosat11	2024-02-25T18:50:24.587	1.3	197
MKD_20240225.0218.tab	Meteosat11	2024-02-25T18:51:53.089	1.3	197
MKD_20240225.0219.tab	Meteosat11	2024-02-25T18:53:26.535	1.3	197
MKD_20240225.0220.tab	Meteosat11	2024-02-25T18:54:52.639	1.3	197
MKD_20240225.0221.tab	Meteosat11	2024-02-25T18:56:29.461	1.3	197
MKD_20240225.0222.tab	Meteosat11	2024-02-25T18:58:52.206	1.3	197
MKD_20240225.0230.tab	Meteosat11	2024-02-25T19:03:29.705	1.3	197
MKD_20240225.0231.tab	Meteosat11	2024-02-25T19:05:17.240	1.3	197
MKD_20240225.0232.tab	Meteosat11	2024-02-25T19:06:45.584	1.3	197
MKD_20240225.0233.tab	Meteosat11	2024-02-25T19:08:15.448	1.3	197
MKD_20240225.0235.tab	Meteosat11	2024-02-25T19:11:25.308	1.3	197
MKD_20240225.0236.tab	Meteosat11	2024-02-25T19:12:53.519	1.3	197
MKD_20240225.0237.tab	Meteosat11	2024-02-25T19:14:23.527	1.3	197
MKD_20240225.0238.tab	Meteosat11	2024-02-25T19:15:55.430	1.3	197
MKD_20240225.0248.tab	Meteosat11	2024-02-25T19:19:47.057	1.3	197
MKD_20240225.0256.tab	Meteosat11	2024-02-25T19:25:16.362	1.3	197
MKD_20240225.0257.tab	Meteosat11	2024-02-25T19:27:43.337	1.3	197
MKD_20240225.0258.tab	Meteosat11	2024-02-25T19:29:11.784	1.3	197
MKD_20240225.0259.tab	Meteosat11	2024-02-25T19:30:39.162	1.3	197
MKD_20240225.0260.tab	Meteosat11	2024-02-25T19:32:07.405	1.3	197
MKD_20240225.0261.tab	Meteosat11	2024-02-25T19:33:35.321	1.3	197
MKD_20240225.0262.tab	Meteosat11	2024-02-25T19:35:23.492	1.3	197
MKD_20240225.0263.tab	Meteosat11	2024-02-25T19:36:52.637	1.3	197
MKD_20240225.0270.tab	Meteosat11	2024-02-25T19:40:41.795	1.3	197
MKD_20240225.0271.tab	Meteosat11	2024-02-25T19:42:15.753	1.3	197
MKD_20240225.0272.tab	Meteosat11	2024-02-25T19:43:38.361	1.3	197
MKD_20240225.0285.tab	Meteosat11	2024-02-25T19:50:34.670	1.3	197
MKD_20240225.0286.tab	Meteosat11	2024-02-25T19:51:59.683	1.3	197
MKD_20240225.0287.tab	Meteosat11	2024-02-25T19:53:23.305	1.3	197
MKD_20240225.0288.tab	Meteosat11	2024-02-25T19:54:46.777	1.3	197
MKD_20240225.0289.tab	Meteosat11	2024-02-25T19:56:09.385	1.3	197